Microwave-assisted Synthesis and Biomedical Applications of Inorganic Nanostructured Materials

JIA, Juncai

A Thesis Submitted in Partial Fulfillment

of the Requirement for the Degree of

Doctor of Philosophy

in

Environmental Science

The Chinese University of Hong Kong

June 2011

Thesis/Assessment Committee

Professor Hung Kay LEE (Chair)

Professor Jimmy C. YU (Thesis Supervisor)

Professor King Ming CHAN (Committee Member)

Professor Bernd ONDRUSCHKA (External Examiner)

Professor Wei CHU (External Examiner)

Abstract

Inorganic nanostrucured materials have attracted much attention owing to their unique features and important applications in biomedicine. This thesis describes the development of rapid and efficient approaches to synthesize inorganic nanostructures, and introduces some potential applications.

Magnetic nanostructures, such as necklace-like $FeNi_3$ magnetic nanochains and magnetite nanoclusters, were synthesized by an efficient microwave-hydrothermal process. They were used as magnetic resonance imaging (MRI) contrast agents. Magnetic $FeNi_3$ nanochains were synthesized by reducing iron(III) acetylacetonate and nickel(II) acetylacetonate with hydrazine in ethylene glycol solution without any template under microwave irradiation. This was a rapid and economical route based on an efficient microwave-hydrothermal process which significantly shortened the synthesis time to mins. The morphologies and size of the materials could be effectively controlled by adjusting the reaction conditions, such as, the reaction time, temperature and concentrations of reactants. The morphology and composition of the as-prepared products were characterized by field emission scanning electron microscopy (FESEM), transmission electron microscopy (TEM), X-ray diffraction (XRD) and X-ray photoelectron spectroscopy (XPS). The size of the aligned nanospheres in the magnetic $FeNi_3$ chains could be adjusted from 150nm to 550nm by increasing the amounts of the precursors. Magnetic measurements revealed that the $FeNi_3$ nanochains showed enhanced coercivity and saturation magnetization. Toxicity tests by exposure of $FeNi_3$ nanochains to the zebrafish larvae showed that the

as-prepared nanochains were biocompatible. *In vitro* magnetic resonance imaging (MRI) confirms the effectiveness of the $FeNi_3$ nanochains as sensitive MRI probes. Magnetite nanoclusters were synthesized by reducing iron(III) acetylacetonate with hydrazine in ethylene glycol under microwave irradiation. The nanoclusters showed enhanced T_2 relaxivity. *In vitro* and *in vivo* MRI confirmed the effectiveness of the magnetite nanoclusters as sensitive MRI probes. We also investigated the biodistribution of the nanoclusters in rat liver and spleen.

Bifunctional mesoporous core/shell $Ag@FeNi_3$ nanospheres were synthesized by reducing iron(III) chloride, nickel(II) chloride and silver nitrate with hydrazine in ethylene glycol under microwave irradiation. The efficient microwave-hydrothermal process significantly shortened the synthesis time to one minute. The toxicity of $Ag@FeNi_3$ nanospheres were tested by exposing to zebrafish, they were less toxic than silver nanoparticles. *In vitro* MRI confirmed the effectiveness of the $Ag@FeNi_3$ nanospheres as sensitive MRI probes. The interaction of Rhodamine B and nanospheres showed greatly enhanced fluorescence over the $FeNi_3$ nanoparticles.

A series of interesting core/shell silver/phenol formaldehyde resin (PFR) nano/microstructures were also synthesized through an efficient microwave process by self-assembly growth. Various morphologies, including monodispersed nanospheres, nanocables, and microcages were obtained by changing the fundamental experimental parameters, such as the reaction time and the surfactants (Pluronic P123 or CTAB). The results indicated that the presence of triblock copolymer Pluronic P123 would result in hollow silver/PFR microcages, while CTAB would prefer the

formation of ultralong silver/PFR coaxial nanocables. In the absence of surfactants, monodispersed core/shell silver/PFR nanospheres could be obtained. The size of the nanospheres can be controlled in the range of 110 to 450 nm by changing the molar ratio of reagents (phenol:hexamine). The morphology and composition of the as-prepared products were characterized. The formation mechanism of the products was discussed based on the obtained results.

Finally, a series of ZnO microarchitectures including monodispersed spindles, branches, flowers, paddies, and sphere-like clusters were prepared by an efficient microwave-hydrothermal process. The ZnO mophologies could be effectively controlled by changing the reaction conditions such as the reaction temperature, the reactant concentrations and the solvent system. Simple microspindles, interesting flowers and paddies could be obtained in the presence of hexamine, and the more attractive sphere-like clusters could be synthesized by introducing phenol. The formation mechanisms of different morphologies are discussed in detail. These interesting ZnO structures may have potential applications in electronic and optoelectronic devices.

摘 要

近年來無機納米材料備受關注，由於其獨特的功能和重要的應用在許多領域，特別是在生物醫學領域有廣泛的應用前景。本論文在無機納米材料的快速高效可控合成、及其形成機制、所獲新型納米解構的性質以及潛在的生物醫學應用進行了有益的探索。

論文第一部分報導了高效微波水熱方法製備磁性納米結構，如項鍊狀的 $FeNi_3$ 納米鏈和磁鐵礦團簇，以及它們作爲核磁共振成像（MRI）造影劑的潛在應用。首先，我們在乙二醇溶液中，沒有添加任何範本的情況下，用水合肼還原乙醯丙酮鐵和乙醯丙酮鎳合成了磁性 $FeNi_3$ 納米鏈，並且採用了微波輔助的程式可控水熱技術。這是一個非常快速、經濟的方法，可以把反應時間縮短爲幾分鐘。並且可以通過調控反應條件，比如反應時間、溫度、反應物的濃度等等來控制納米材料的形貌和尺寸。我們用場發射掃描電鏡（FESEM），透射電子顯微鏡（TEM），X 射線衍射（XRD）和 X 射線光電子能譜（XPS）對所製備的樣品形貌和結構組成進行了表徵。我們發現，隨著前驅體濃度的增加，每個 $FeNi_3$ 鏈上單個納米球的尺寸可以從 150nm 調整至 550nm。磁性測量結果表明，$FeNi_3$ 納米鏈增強了磁矯頑力和飽和磁化強度。$FeNi_3$ 納米鏈暴露在斑馬魚幼體的毒性測試表明了所製備的納米鏈的生物相容性。體外磁共振成像（MRI）證實了 $FeNi_3$ 納米鏈可以用作磁共振成像的有效探針。此外，我們也用微波輻射的方法製備了磁鐵礦納米簇。此部分依然用乙醯丙酮鐵爲原料，用肼作爲還原劑在乙二醇溶液中反應。該納米簇顯示增強了 T_2 弛豫度。體外和體內 MRI 證實了該磁鐵礦納米簇可以作爲磁共振成像造影劑的有效性。我們還研究了該磁鐵礦納米簇在大鼠肝和脾的納米簇生物分佈。

此外，我們通過在乙二醇溶液中用肼作還原劑還原氯化鐵、氯化鎳和硝酸銀的方法一步合成了具有核殼結構的雙功能 Ag@$FeNi_3$ 納米球。此部分我們仍然採用快速、高效的微波水熱方法，製備時間僅一分鐘。斑馬魚毒性實驗表明，和銀納米顆粒相比，Ag@$FeNi_3$納米球的毒性已經大大減少。體外 MRI 證實了 Ag@$FeNi_3$ 納米球可以作爲有效的磁共振成像探針。羅丹明 B 和納米球的相互作用的實驗結果表明，和普通 $FeNi_3$納米顆粒相比，Ag@$FeNi_3$納米球大大加強了羅丹明 B 的螢光。

與此同時，本論文報導了用微波合成方法製備一系列有趣的核殼結構的銀/苯醛樹脂（PFR）納米/微米結構。通過調整各項實驗參數，如反應時間，表面活性劑的種類（聚醚P123或CTAB）實現調控樣品的形貌，包括單分散納米微球、納米電纜、微米籠。結果表明，三嵌段共聚物P123的存在會產生銀/苯醛樹脂（PFR）空心微米籠，而CTAB會生成超長的銀/苯醛樹脂（PFR）同軸納米電纜。在沒有任何表面活性劑存在的情況下，則生成單分散的核殼小球。並且通過調節苯酚、四氮六甲圜的比例和濃度，可以有效的控制核殼納米球的尺寸（110nm－450nm）。此外我們根據實驗結果分析討論了各種形貌的形成機理。

最後，我們用微波水熱的方法製備了一系列單分散氧化鋅微米結構，包括微米紡錘、樹枝、花朵、稻穀和球狀團簇。通過改變反應條件，如反應時間、反應物濃度和溶劑類型可以有效的控制氧化鋅的形貌。在四氮六甲圜存在時，可以生成紡錘、樹枝、花朵和稻穀狀的氧化鋅。加入苯酚則可以形成球狀氧化鋅團簇。並討論了這些不同形貌的形成機理。這些有趣的氧化鋅的結構可能在電子和光電子器件的應用潛力。

Acknowledgements

It is my great pleasure to take this opportunity to thank all of the people who have contributed to my thesis directly or indirectly.

First of all, I would like to express my sincere gratitude and appreciation to my supervisor, Prof. Jimmy C. Yu, for his expert guidance and generous support throughout my Ph.D. study at The Chinese University of Hong Kong. I have not only learnt a lot from him but have also been inspired by his dedicated attitude to science. I am also deeply impressed by his profound knowledge in research. He took me into the interesting world of nanoscience and nanotechnology technology with his broad knowledge and precious insights. I was very impressed by his enthusiasm and strict attitude both as a scientist and as an academic professional. He helped me to be independent and creative in almost all aspects of research. Throughout my life I will benefit from the experience, knowledge, and confidence that I gained while working with Professor Jimmy C. Yu.

Special thanks are given to the thesis committee members, Prof. Hung Kay LEE, Prof. King Ming CHAN, Prof. Bernd ONDRUSCHKA and Prof. Wei CHU for their time and energy spent on reading this thesis.

I would like to thank Prof. King Ming Chan for toxicity studies using zebrafish embryos and larvae in biochemistry department. I also would like to thank Professor, Yixiang WANG, for his generous supporting my work in magnetic resonance imaging (MRI) experiments in Prince of Wales hospital, and introducing me into the new field

of important applications of magnetic nanomaterials. I am also grateful to Mr Andrew LEE and Mr Man Hau YUENG for the help of using SEM and TEM in central lab of physics department.

Much thanks to all of my lab-mates for their highly knowledgeable discussion. Their constructive comments were essential to the completion of this dissertation. I would like to acknowledge all the staff members in the Department of Chemistry for the contribution to an active academic atmosphere. In addition, this research work was made possible by the generous financial support of the Research Grants Council of Hong Kong.

Finally, I am deeply grateful to my family members without whom this thesis would not be possible. I thank my parents for their unlimited support and confidence in me. I also want to thank my husband, Jiangtao Zhu, for his unconditional love, concern, support and encouragement for the pursuit of my Ph.D. I am indebted to him for everything he did for me, which cannot be listed here in a few words.

Feb 2011

Jia, Juncai

Environmental Science Programme

The Chinese University of Hong Kong

List of Figures

List of Tables

List of Schemes

Table of Contents

Chapter One

Introduction

1.1 Nanostructured materials

Nanostructured materials are simply defined by their size, according to the ASTM standard definition, they are particles with lengths that range from 1 to 100 nanometers in one, two or three dimensions.[1] Nanomaterials include one-dimensional rods, wires or tubes, two-dimensional sheets, or three dimensional spheres.[2-7] In the past decades, nanostructured materials were widely utilized in various areas, such as electronic, magnetic, catalytic, optical, environmental remediation, and biomedical applications.[8-12] The interest and effort to develop existing materials in the nanometer scale come from the extraordinary physical properties of these materials compared to their bulk counterparts. These extraordinary properties arise due to the enormous increase in the surface-to-volume (S/V) ratio and the predominance of quantum mechanical phenomena exhibited by materials in this particular length scale.[13]

1.2 Synthesis of inorganic nanostructured materials

1.2.1 Method of synthesis

There are basically two approaches for the synthesis of nanostructured matrials, irrespective of the field or discipline: 'Top-Down' and 'Bottom-Up'. In the 'Top-Down' approach, bulk materials are reduced by certain processes to form nanostructures. 'Top-Down' is obtained by cutting, breaking or etching techniques,[14] by bulk or film machining, mold machining employing and lithography surface machining.[15] Bulk machining employs photolithography which applies the etching process while mold machining employs soft lithography. Other techniques are x-ray lithography, electron beam lithography and micro-electro-mechanical systems lithography.[16, 17] However, photolithography and related techniques have limitations of fabricating nanostructures of sub-100nm and so are not suitable for nanostructures below 100 nm.[18]

In the 'Bottom-Up' approach, the building of nanostructured materials is obtained by growing or assembling of atoms or molecules which are the building blocks. The building blocks can be used by controlling chemical reactions to self-assemble and synthesize nanostructures such as nanotubes and quantum dots.[15] Atoms or molecules may also be physically used to form nanostructures by minute probes.[19] Self-assembling of atoms or molecules can be obtained by templating or non-templating.[14] Templating involves the interaction of macromolecules under the influence of a specific sequence, structure, pattern, spatial constraint or external force.

For instance, block co-polymers and non-ionic surfactants are used as templates in the formation of nanostructures. Two dimensional hexagonal nanostructures formed by cylindrical amphiphilic polymeric micelles were used as templates to fabricate nanotubes of cadmium sulphide.[20] Non-templating is the formation of nanostructures from atoms or molecules without template but under external influence.[14] Self-assembly lithography is a cost-effective and efficient technique that can be used to produce nanostructures below 100nm.[15]

'Bottom-Up' is considered to be an ideal approach for nanotechnology.[21] Bottom-Up shows almost unlimited possibilities in the design and construction of artificial molecular devices capable of performing specific functions upon stimulation with external energy.[22] However, one of the challenges of the bottom-up approach is the random movement exhibited by atoms which has to be overcome. [23]

In the past decades, the synthesis of inorganic nanocrystals with controlled size and shape has attracted rapidly growing interest both for fundamental scientific interest and many practical and technological applications.[23-25] The shape control and assembly of nanostructures into organized patterns provide valuable routes to the design of functional materials and to a variety of applications. [23-25] Many chemical methods were developed for the synthesis of controlled size and shape of nanostructures. Examples of these approaches include template-assisted, solvothermal methods, sonochemical reactions, kinetic growth control, and thermolysis of single-source precursor in ligating solvents.[23-29]

1.2.2 Microwave Irradiation (MWI) method

Upon realization that the properties of the materials are influenced by the size and shape, it becomes an issue to control the synthetic methodologies. It is well known that the growth of the materials at the nanoscale is largely dependent on the thermodynamic and kinetic barriers in the reaction, as defined by the reaction trajectory; and growth is influenced by vacancies, defects, and surface reconstruction events.[30] Most synthetic methods for producing inorganic nanomaterials use conventional thermal heating that relies on conduction of blackbody radiation to drive the reaction. The reaction vessel acts as an intermediary for energy transfer from the heating mantle to the solvent and finally to the reactant molecules. It can cause sharp thermal gradients throughout the bulk solution and inefficient, non-uniform reaction conditions. This is a common problem encountered in chemical scale-up and is more problematic for nanomaterials, where uniform nucleation and growth rates are critical to material quality.[30]

Microwave Irradiation (MWI) methods can solve the problem of heating inhomogeneity. Microwaves are electromagnetic radiation, with wavelengths in the range of 1 mm to 1 m (frequency range 0.3 to 300 GHz). A large part of the microwave spectrum is used for communication purposes and only narrow frequency windows centered at 900 MHz and 2.45 GHz are allowed for microwave heating purposes. Heating by microwave has been known since the early 1940s and has been used successfully in the food industry. MWI as a heating method has been used in a number of applications in chemistry since 1986.[31] The main advantage of using

microwaves is that it accelerates organic reactions.[32,33] MWI methods provide simple and fast routes to the synthesis of nanomaterials. MWI is potentially useful in large-scale synthesis due to the small thermal gradient effects in MWI processes.[34-38]

In addition, due to the difference in the solvent and reactant dielectric constants, selective dielectric heating can provide significant enhancement in reaction rates. The rapid transfer of energy direct to the reactants (faster than they are able to relax), causes an almost instantaneous internal temperature rise. By chosing metal precursors with larger microwave absorption cross-sections than that of the solvent, high effective reaction temperatures can be achieved. This allows the rapid decomposition of the precursors, which creates high supersaturated solutions. These conditions lead to the formation of very small nanocrystals since the higher the supersaturation the smaller the critical size required for nucleation. On the other hand, the growth of the newly formed nanocrystals can be effectively inhibited by the adsorption of ligating organic surfactants which could bind strongly to the surfaces of the nanocrystals, thus stabilizing and passivating the surfaces. Furthermore, selective adsorption of the ligating organics can significantly slow down the growth of the nanocrystal in all but the favorable crystallographic plane thus resulting in a one dimensional (ID) structure or special designed structure. Compared with the conventional heating methods, this provides energy efficiency by reducing the reaction times from hours to minutes, and it also culminates in clean reaction products and higher yields. As a result, the microwave irradiation is an efficient, environmentally friendly, and economically viable heating method for the production of nanomaterials.

Since in MWI it is possible to quench the reaction in 10 seconds, this provides the opportunity of controlling the nanostructures from small spherical nuclei to short rods to extended assemblies of nanowires by varying the MWI reaction time and the relative concentrations of different organic surfactants with variable binding strengths to the initial precursors and to the nanocrystals.

This dissertation discusses the synthesis of various inorganic nanomaterials under microwave irradiation conditions.

1.3 Biomedical applications of inorganic nanostructured materials

Inorganic nanomaterials provide a particularly useful platform, demonstrating unique properties with potentially wide-ranging therapeutic applications.[39] In this part, we will discuss three major areas of nanoparticle application: (i) magnetic resonance imaging (MRI) (ii) metal-enhanced fluorescence (MEF), and (iii) drug delivery.

1.3.1 Magnetic resonance imaging (MRI)

MRI is one of the most powerful diagnosis tools in biomedical science.[40] It has been the preferred tool for assessing cardiac function, for imaging the brain and the central nervous system and for detecting tumors. Since it can give anatomic images of tissue with high resolution, it is expected to become a very important tool for molecular and cellular imaging. MRI contrast agents are used to clarify images and

can give better interpretation. Currently, most available MRI contrast agents are paramagnetic complexes, usually gadolinium (Gd^{3+}) chelates.[41] Superparamagnetic iron oxide (SPIO) is a different class of contrast agents, and it has received great attention since it was developed as a liver contrasting agent.[42,43] Alloy materials can also be candidates for more-efficient T_2 contrast agents. Various bimetallic ferrite nanoparticles, including $CoFe_2O_4$, $MnFe_2O_4$, and $NiFe_2O_4$, have been tested for T_2 contrast agents.[44] Table 1.1 summarizes different kinds of T_2 contrast agents and their physical and chemical properties. [44-53]

Table 1.1 Kinds of T_2 contrast agents. Reproduced from Reference 45.

Name	Core Material	Surface	Diameter of Core [nm]	Hydrodynamic Diameter [nm]	Magnetization [emu g^{-1}][a]	r_2 [mM^{-1} s^{-1}]	B_0 [T]
Ferumoxides (Feridex)	Fe_3O_4, γ-Fe_2O_3	Dextran	4 96	160	45	120	1.5
Ferucarbotran (Resovist)	Fe_3O_4	Carboxydextran	4	60		186	1.5
Ferumoxtran (Combidex)	Fe_3O_4	Dextran	5.85	35	61	65	1.5
CLIO-Tat	Fe_3O_4	Dextran	5	30	60	62	1.5
WSIO (MEIO)	Fe_3O_4	DMSA[b]	4		25	78	1.5
			6		43	106	
			9		80	130	
			12		101	218	
FeNP	α-Fe	PEG	10		70	129	1.5
MnMEIO	$MnFe_2O_4$	DMSA[b]	6		68	208	1.5
			9		98	265	
			12		110	358	
CoMEIO	$CoFe_2O_4$	DMSA[b]	12		99	172	1.5
NiMEIO	$NiFe_2O_4$	DMSA[b]	12		85	152	1.5
Au-Fe_3O_4	Fe_3O_4	PEG	20			114	3.0
Au-FePt	FePt (fcc)	PEG	6			59	3.0

[a] Magnetic properties were measured at 1.5 T external field.

[b] 2,3-Dimercaptosuccinic acid.

The basic principle of MRI is based on nuclear magnetic resonance (NMR) together with the relaxation of proton spins in a magnetic field.[40] When the nuclei of protons are exposed to a strong magnetic field, their spins align parallel (low energy state) or anti-parallel (high energy state) to the external magnetic field. During their alignment, the spins precess under a specified frequency, the Larmor frequency. When a 'resonance' frequency in the radio-frequency (RF) range is introduced to the nuclei, the protons absorb energy and are excited to the antiparallel state. With time following the excitation, the system will return to its thermal equilibrium after losing energy due to the relaxation process. There are two distinct types of relaxation pathways. The first type, called spin-lattice relaxation or T_1, involves the decreased net magnetization (Mz) recovering to the initial state. The second type, called spin-spin relaxation or T_2, involves the induced magnetization on the perpendicular plane (Mxy) disappearing by the dephasing of the spins. Based on the two relaxation types, the contrast agents are classified as T_1 and T_2 contrast agents. Commercially available T_1 contrast agents are usually paramagnetic complexes, while T_2 contrast agents are based on iron oxide nanoparticles, which are the most representative nanoparticulate agents. Iron oxide nanoparticles are superparamagnetic and losing their magnetization in the absence of an external magnetic field. However, when an external magnetic field is applied, they exhibit strong magnetization, which can cause microscopic field inhomogeneity and activate the dephasing of protons. Therefore, iron oxide nanoparticles can shorten T_2 relaxation times of the neighboring regions, and produce a decreased signal intensity in T_2-weighted MR images.

The contrast agents can be extravazated from the blood vessels into interstitial spaces, and they are transported to lymph nodes through lymphatic vessels. Nanoparticles are uptaken only by the normal nodes, as nodes with malignant cells cannot undergo phagocytosis by nodal macrophages. Their accumulation within normal nodes produces significant susceptibility effects, and the specific uptake allows a more sensitive detection between normal and malignant cells. Therefore, the contrast agents are expected to improve the diagnosis of metastatic tumors, and they are currently under investigation for human applications. For instance, Weissleder and coworkers reported the detection of lymph-node metastases in patients with prostate cancer using SPIO.[54]

1.3.2 Metal-enhanced fluorescence (MEF)

When molecules are adsorbed onto Ag and Au surfaces, or nanostructured Ag and Au colloids, they can produce a million fold increase in the intensity of Raman scattering, known as surface-enhanced Raman scattering (SERS).[55,56] In the past few years, it is reported that even single molecule spectroscopy is possible using SERS, and the enhancement factor can reach 10^{14}-10^{15}.[57,58] The effective Raman cross sections are then comparable to the usual fluorescence cross sections. Second-harmonic generation at a metal-air interface can also be enhanced by surface roughness, and it is accompanied by a broad luminescence background extending far beyond the anti-Stokes side of the second harmonic. On the other hand, nonlinear Raman scattering is facilitated by the surface-enhanced effect. All these phenomena

are accompanied by a strongly enhanced electric field in the vicinity of the metal structure via the excitation of resonant surface plasmon modes.[55,59] A dramatic increase in the fluorescence emission can also occur on nanostructured Ag and Au surfaces. The phenomenon, called surface-enhanced fluorescence (SEF) or metal-enhanced fluorescence (MEF),[60-68] is derived from the interaction of the dipole moment of the fluorophore and the surface plasmon field of the metal, resulting in fluorescence enhancement, increased photostability, reduced blinking in single molecule fluorescence spectroscopy,[69] decreased lifetime owing to increased rates of system radiative decay, and increased transfer distances for fluorescence resonance energy transfer.[70] In effect, it demonstrates that weakly emitting materials (dyes, proteins, or DNA) with low quantum yields can be transformed into more efficient fluorophores with a shortening of fluorescence lifetimes. The reduction in fluorescence lifetimes due to MEF means that molecules spend less time in the excited state, thus reducing photobleaching effects.[63] These characteristics of the MEF effect therefore can be utilized in the development of efficient fluorescence-based sensors and microarrays.[63,71]

The use of fluorescent nanoparticles as indicators in biological applications such as imaging and sensing has dramatically increased since the 1990s.[72,73] These applications require that the fluorescent nanoparticles are monodisperse, photostable, bright, and amenable to further surface modification for the conjugation of biomolecules or fluorophores. Among many types of fluorescent nanoparticles available, nanoparticles with core/shell architecture can fulfill all these requirements,

combining multifunctionalities into a single hybrid nanocomposite.[74-76]

In the past years, many factors were studied that could influence the magnitude of the MEF phenomenon, such as, the use of different metals including silver,[77] gold,[78,79] copper,[80] chromium,[81] and zinc;[82] different nanostructure architectures such as silver islands films (SIFs), silver colloids, silver nanorods, silver nanotriangles, and fractal-like silvered surfaces;[83] and the size of these nanoparticles, as well as the nature of the surrounding media, dielectric, temperature, etc.[84]

Up to now, MEF is thought to be comprised of two cooperative mechanisms[85] and near-field interactions: an electric field effect and an induced plasmon effect. In the so-called electric field effect, fluorophores in close proximity (<10 nm) to plasmonic nanoparticles are exposed to the increased electric fields between and around the nanoparticles, which can effectively result in significant increases in their absorption cross section.[86] This leads itself to a subsequent increase in the excitation and eventually in the fluorescence emission of the fluorophores, and the fluorescence lifetime remains unchanged. In the second mechanism, the excited state energies of fluorophores are partially transferred to surface plasmons, and two distinct observations can be made for fluorescent species in close proximity to plasmonic nanoparticles: (1) an increase in the fluorescence emission from the metal-fluorophore unified system with the spectral properties of the fluorophores maintained and (2) a decrease in the excited-state decay time (fluorescence lifetime), which invariably gives rise to improvements in the photostability of the fluorophores, due to their spending less time in a reactive excited state.

1.3.3 Drug delivery

Some of the challenges of most drug delivery systems (DDSs) include poor bioavailability, in vivo stability, intestinal absorption, solubility, sustained and targeted delivery to site of action, side effects, therapeutic effectiveness, and plasma fluctuations of drugs, and they will either fall below the minimum effective concentrations or exceed the safe therapeutic concentrations. Nanostuctrued materials in drug delivery are designed to overcome these challenges due to the development and fabrication of nanostructures at submicron scale and nanoscale which have multiple advantages.

DDSs by nanostructured mateials can improve several crucial properties of ''free'' drugs, such as solubility, in vivo stability, pharmacokinetics, and biodistribution, enhancing their efficacy.[87] Generally, nanostructured mateials have the ability to protect drugs encapsulated within them from hydrolytic and enzymatic degradation in the gastrointestinal tract; and then they can target the delivery of a wide range of drugs to various areas of the body for sustained release and thus are able to deliver drugs, proteins and genes through the peroral route of administration.[88-90] They can deliver drugs that are highly water insoluble, which can bypass the liver, therefore preventing the first pass metabolism of the incorporated drug.[91,92] They can also increase oral bioavailability of drugs, due to their specialized uptake mechanisms such as absorptive endocytosis. The drugs are able to remain in

the blood circulation for a much longer time, and release in a sustained and continuous manner, which lead to less plasma fluctuations thereby minimizing side-effects caused by drugs.[91] The nanostructures are able to penetrate into tissues and are uptaken by cells, allowing efficient delivery of drugs to sites of action. The uptake of nanostructures was found to be 15-250 times greater than that of microparticles in 1-10μm range.[93] Lin et al. reported that thiols, such as dihydrolipoic acid and dithiothreitol, could act as stimuli to remove caps of the pores in mesoporous silica nanoparticles and hence released trapped molecules inside the pores.[94,95] The pores could be capped with removable Fe_3O_4 or CdS nanoparticles through disulphide linkers that cleave in a reducing environment. Release of encapsulated fluorescein isothiocyanate (FITC) from magnetic nanoparticle-capped MCM-41 was obtained in cancer cells. pH-responsive nanomateials provided an alternate mechanism for release, relying on the acidic condition inside tumor and inflamed tissues (pH～6.8) and cellular compartments including lysosomes (pH～4.5–5.0) and endosomes (pH～5.5–6).[96] Magnetic nanoparticles (Fe_3O_4) were covalently functionalized with doxorubicin (DOX), an anticancer drug, through an acid-labile hydrazone linker.[97] The carrier was then encapsulated with thermosensitive polymer for temperature-controlled release of the drug. The hybrid system released DOX efficiently in mild acidic buffer solution of pH 5.3.

1.4 Toxcity test of inorganic nanostructured materials

1.4.1 Potential toxicity of inorganic nanostructured materials

The presence of inorganic nanostructured materials in commercially available products is becoming more common. With this increase in manufacturing of nanomaterials-containing merchandise along with the constant discovery of new applications of nanoparticles, human exposure to nanoparticles is inevitable. As a result, nanotoxicology research is now gaining attention. However, while the number of nanoparticle types and applications continues to increase, studies to characterize their effects after exposure and to address their potential toxicity are few in comparison. In the medical field in particular, nanostructured materials are being utilized in diagnostic and therapeutic tools to better understand, detect, and treat human diseases. Exposure to nanomaterials for medical purposes involves intentional contact or administration. Therefore, understanding the properties of nanomaterials and their effect on the body is crucial before clinical use can occur. For nanomaterials to move into the clinical arena, it is important that nanotoxicology research uncovers and understands how these multiple factors influence the toxicity of nanomaterials so that their undesirable properties can be avoided. Meanwhile, the application of these materials will be limited by their inherent toxicity.[98,99] Thus, the need for evaluating nanotoxicity is becoming increasingly paramount.

1.4.2 Zebrafish as a model for biotoxicity studies

Reliable in vivo models are required to assess the biodistribution and toxicity of nanomaterials and thereby bridge in vitro cell models and small mammalian models. Small mammalian models remain the putative method to assessthe possible toxicities and biodistribution of nanomaterials in humans. Most commonly, both human diseases and possible drug candidates have been modeled in mammals because of close homology between the mammalian genomes.[100] Typically, rats are used in toxicology experiments, whereas mice are used in efficacy models. However, establishing mammalian models is often expensive and time consuming, and there remains a clear disconnect between in vitro and in vivo data preventing reliable predictive effects on toxicity, biodistribution, and efficacy. Instead, one of the most promising in vivo model systems for toxicity studies is Danio rerio, commonly known as zebrafish. The National Institute of Environmental Health Sciences (NIEHS) in the United States and the Institute for Environment and Sustainability (IES) in Europe support the zebrafish as one model organism to study environmental toxicity.[101] Furthermore, the National Institutes of Health (NIH) recognizes the zebrafish as an alternative model for exploring human disease, development, and physiology. With its extensive background in various biological fields,[101-104] numerous benefits accompany the zebrafish for studying nanotoxicology: (i) a high degree of homology to the human genome and comparable human tissue types;[101,105,106] (ii) a nearly identical physiologic response to xeno-substances as mammals (e.g., oxidative stress and induction of foreign body metabolizing enzymes);[101,107-109] (iii) Post-fertilization,

zebrafish embryos rapidly develop ex-utero—less than 1 week is required for the development of the digestive, nervous, and cardiovascular organ systems,[102 105] as shown in Fig. 1.1. (iv) a medium-throughput screening ability at significantly lower costs due to being extremely small in size (3–4 cm as adults, 4mm as early larvae), implying low sample volumes[102] and decreased housing/husbandry costs;[103-106] (vi) the high fecundity of zebrafish presents a significant reduction in time aswell; zebrafish are capable of fertilizing 200–300 eggs per day every 57 days and have an equivalent longevity and generation time to mice (3–5 months).[105 106] (vii) the biology and optical clarity of zebrafish embryos allows testing at all stages of embryonic development.[104-106] These characteristics translate into the ability to examine the in vivo course of pathological processes in real time, such as organogenesis, vasculogenesis, and deleterious effects during anatomical development.[104 109]

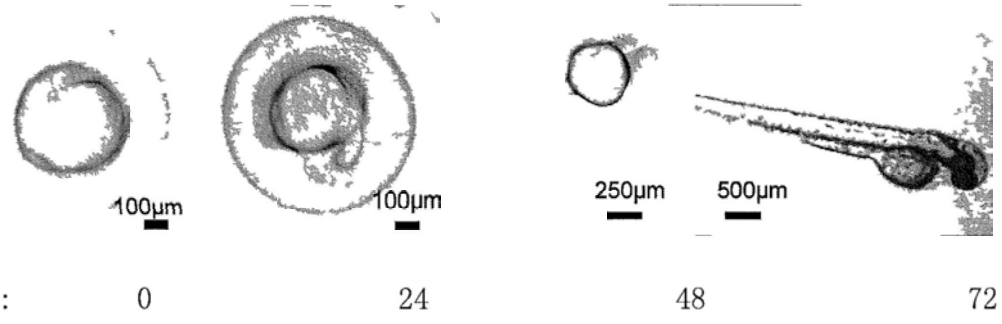

Figure 1.1 The development of zebrafish embryos at different time intervals (hours post-fertilization)

Assessment of nanotoxicity can be semi-quantified as sublethal toxicities (viz. survival of the embryo and the severity of phenotypic and gross morphological

differences). This nano-toolkit allows several parameters to be varied including concentration, nanomaterial size, chemical composition, density, route of exposure, time of exposure, and the point of embryonic development at which the nanomaterial is administered.[104] Since whole animals are used in zebrafish-based drug screen studies, both bioavailability and toxicity can be assayed and examined. Unlike traditional biochemical assays that explore specific molecular targets, the zebrafish model relies on the analysis of phenotypic changes. This method allows researchers to bypass several roadblocks commonly associated with current drug discovery efforts, which are based on in vitro biochemical screens followed by in vivo mammalian studies. The zebrafish model is a rapid and cost-effective method to conservatively assess the toxicity of novel nanopharmaceuticals, flagging those samples displaying nanotoxicity for closer scrutiny and possible removal from continued drug development.

Many studies were performed to evaluate the toxicity of metal and metal oxide nanoparticles. Zhu et al. studied the toxic effects of metal oxide nanoparticles in aqueous suspension by the zebrafish model.[111] In their study, a 96-hour zebrafish embryo-larval assay was used to study the relative toxicities of nZnO, $nTiO_2$ and nAl_2O_3, as well as the bulk form of each metal oxide. They determined that both nZnO and bulk ZnO delayed the hatching rate and development of embryos and larvae, caused tissue damage and decreased survival. Malformation of the embryos was characterized by several conditions including tissue ulceration, body arcuation and pericardial edema. Under the same experimental conditions, neither $nTiO_2$ and

nAl_2O_3 nor their bulk counterparts caused any visible toxicity in the zebrafish embryos and larvae. Griffitt et al. studied the Cu nanoparticles toxicity with zebrafish.[112] The results of the study showed that Cu nanoparticles were acutely toxic to zebrafish, with a 48 h LC_{50} concentration of 1.5mg/L, that would be classified asmoderately toxic by the U.S. Environmental Protection Agency. Further biochemical and histological analyses showed that the primary organ for Cu nanoparticles toxicity was the gill. Exposure of Cu nanoparticles caused the proliferation of interlamellar cells and inhibited Na^+/K^+ ATPase activity. There was no evidence, neither histological nor biological, of damage to other organs. Bar-Ilan et al[110] used a series of sizes (3, 10, 50, and 100 nm) colloidal silver (cAg) and gold nanoparticles (cAu) and a semiquantitative scoring system, they found that cAg produces almost 100% mortality at 120 h postfertilization, while cAu produces less than 3% mortality at the same time point. Furthermore, while cAu induces minimal sublethal toxic effects, cAg treatments generate a variety of embryonic morphological malformations. Both cAg and cAu were taken up by the embryos and control experiments, suggesting that cAg toxicity was caused by the nanoparticles themselves or Ag^+ that was formed during in vivo nanoparticle destabilization. Although cAg toxicity was slightly size dependent at certain concentrations and time points, the most striking result was that parallel sizes of cAg and cAu induced significantly different toxic profiles, with the former being toxic and the latter being inert in all exposed sizes. Therefore, it could be proposed that nanoparticle chemistry is as important as specific nanosizes at inducing toxicity *in vivo*. Furthermore, the zebrafish

embryo is a resourceful model for assessing nanotoxicology. The results from this study may portend the zebrafish as the new ''go-to'' organism to gauge systemic toxicity accurately for nanomaterials, and it can be used to identify physicochemical properties affording lower incidences of toxic effects.

1.5 Summary

This chapter gave an introduction on the classification and preparation methods of inorganic nanostructured materials, especially the microwave-assisted method was discussed. Furthermore, the biomedical applications of inorganic nanostructured materials were introduced. Finally, this chapter introduced the toxicity test of inorganic nanomaterials using zebrafish.

1.6 Aim of this research and its significance

The objective of this thesis is to fabricate nanostructured materials with tunable sizes and controllable morphologies by microwave process. These materials are expected to have promising applications in the biomedical field.

The first goal of this dissertation is to synthesize a series of magnetic nanostructures (necklace-like $FeNi_3$ magnetic nanochains and magnetite nanoclusters) with various morphologies by an efficient microwave process, and then use them as

magnetic resonance imaging (MRI) contrast agents. Magnetic $FeNi_3$ nanochains were synthesized by reducing iron(III) acetylacetonate and nickel(II) acetylacetonate with hydrazine in ethylene glycol solution without any template under microwave irradiation. The size of the aligned nanospheres in the magnetic $FeNi_3$ chains will be adjusted by changing the amounts of the precursors. Magnetic measurement will be applied on the $FeNi_3$ nanochains to know their coercivity and saturation magnetization. Toxicity tests by exposure of $FeNi_3$ nanochains to the zebrafish larvae will be done to test whether the as-prepared nanochains are biocompatible. *In vitro* magnetic resonance imaging (MRI) will be used to confirm the effectiveness of the $FeNi_3$ nanochains as sensitive MRI probes. On the other hand, magnetite nanoclusters will be synthesized by reducing iron(III) acetylacetonate with hydrazine in ethylene glycol under microwave irradiation. *In vitro* and *in vivo* MRI will be used to confirm the effectiveness of the magnetite nanoclusters as sensitive MRI probes. We also investigate the biodistribution of the nanoclusters in rat liver and spleen.

The second goal of this work is to synthesize bifunctional mesoporous core/shell $Ag@FeNi_3$ nanospheres by reducing iron(III) chloride, nickel(II) chloride and silver nitrate with hydrazine in ethylene glycol under microwave irradiation. The efficient microwave-hydrothermal process is intended to shorten the synthesis time to one minute. Toxicity of $Ag@FeNi_3$ nanospheres will be tested to be compared to silver nanoparticles by exposuring to zebra fish. *In vitro* MRI will be used to confirm the effectiveness of the $Ag@FeNi_3$ nanospheres as sensitive MRI probes. The Rhodamine B will be adsorbed on the nanospheres to show the greatly enhanced fluorescence

over the $FeNi_3$ nanoparticles.

The third goal of this research is to use a fast microwave-assisted approach to fabricate hollow silver/PFR microcages and ultralong and flexible silver/PFR coaxial nanocables separately for the first time via one step. The effect of the surfactant, triblock copolymer Pluronic P123 and CTAB on the final structures will be discussed. The results indicate that the presence of triblock copolymer Pluronic P123 would result in hollow silver/PFR microcages, while CTAB would prefer the formation of ultralong silver/PFR coaxial nanocables. In the absence of surfactants monodispersed core/shell silver/PFR nanospheres could be obtained. This kind of novel superstructure is also expected to have potential applications in catalyst support, drug delivery, separation technology, biomedical engineering, and nanotechnology owing to its unique structures.

Finally, a series of ZnO microarchitectures including monodispersed spindles, branches, flowers, paddies, and sphere-like clusters were prepared by a microwave-hydrothermal process. These interesting ZnO structures may have potential applications in electronic and optoelectronic devices. This efficient method significantly reduces the synthesis time to minutes.

1.7 References

(1) ASTM E 2456-06 "Terminology for Nanotechnology." ASTM International, 2006.

(2) Meuer, S.; Oberle, P.; Theato, P.; Tremel, W.; Zentel, R. *Adv. Mater.* **2007**, *19*, 2073.

(3) Ou, Y. N.; Li, G. R.; Wang, Z. L.; Yu, X. L.; Tong, Y. X. *J. Electrochem. Soc.* **2010**, *157*, D264.

(4) Pan, M. H.; Liu, H.; Wang, J. Z.; Jia, J. F.; Xue, Q. K.; Li, J. L.; Qin, S.; Mirsaidov, U. M.; Wang, X. R.; Markert, J. T.; Zhang, Z. Y.; Shih, C. K. *Nano Lett.* **2005**, *5*, 87.

(5) Elias, J.; Tena-Zaera, R.; Wang, G. Y.; Levy-Clement, C. *Chem. Mater.* **2008**, *20*, 6633.

(6) Lin, H. H.; Wang, C. Y.; Shih, H. C.; Chen, J. M.; Hsieh, C. T. *J. Appl. Phys.* **2004**, *95*, 5889.

(7) Tao, C. G.; Cullen, W. G.; Williams, E. D.; Hunyadi, S. E.; Murphy, C. J. *Surf. Sci.* **2007**, *601*, 4939.

(8) Kamtekar, K. T.; Monkman, A. P.; Bryce, M. R. *Adv. Mater.* **2010**, *22*, 572.

(9) Sculimbrene, B. R.; Imperiali, B. *J. Am. Chem. Soc.* **2006**, *128*, 7346.

(10) Gaya, U. I.; Abdullah, A. H. *J. Photoch. Photobio. C-Photochem. Rev.***2008**, *9*, 1.

(11) Alivisatos, A. P.; Gu, W. W.; Larabell, C. *Annu. Rev. Biomed. Eng.* **2005**, *7*, 55.

(12) Cheon, J.; Lee, J. H. *Acc. Chem. Res.* **2008**, *41*, 1630.

(13) Williams, D. *Biomaterials.* **2008**, *29*, 1737.

(14) Guo, P. *J. Nanosci. Nanotechnol.* **2005**, *5.*

(15) Majumder, D. D; Banerjee, R; Ulrichs, C. H.; Mewis, I. *IETE Tech. Rev.* **2007**, *24*, 9.

(16) Teo, B. K.; Sun, X. H. *J. Cluster. Sci.* **2006**, *17*, 529.

(17) Romig, A. D.; Baker, A. B.; Johannes, J.; Zipperian, T.; Eijkel, K.; Kirchoff, B.; Mani, H. S.; Rao, C. N. R.; Walsh, S. *Technol. Forecasting Social Change* **2007**, *74*, 1634.

(18) Balzani, V. *Small* **2005**, *1*, 278.

(19) Horton, M. A.; Khan, A. *Nanomedicine: NBM* **2006**, *2*, 42.

(20) Liu, T.; Burger, C.; Chu, B. *Prog. Polym. Sci.* **2003**, *28*, 5.

(21) Mansoori, G. A. Advances in atomic and molecular nanotechnology. United Nations Tech Monitor; UN-APCTT Tech Monitor, 2002; Special Issue: 53-59.

(22) Wikipedia, History of Nanotechnology. Wikipedia: Free encyclopaedia. http://en.wikipedia.org/wiki/History_of_nanotechnology Accessed 03 August, 2008.

(23) Schmidt, G. *Nanoparticles from Theory to Application,* Wiley-VCH, Weinheim, **2004**.

(24) Alivisatos, A. P. *J. Phys. Chem.* **1996,** *100*, 13226.

(25) El-Sayed, M. A. *Acc. Chem. Res.* **2004,** *37,* 326.

(26) Peng, Z.; Manna, W.; Wickham, J.; Scher, E.; Kadavanich, A.; Alivisatos, A. P. *Nature* **2000,** *404,* 59.

(27) Park, J.; An, K.; Hwang, Y.; Park, J.-G.; Noh, H.-J.; Kim, J.-Y.; Park, J.-H.; Hwang, N.-M.; Hyeon, T. *Nat. Mater.* **2004,** *3,* 891.

(28) Li, Y.; Malik, M. A.; O'Brien, P. *J. Am. Chem. Soc.* **2005,** *127*, 16020.

(29) Wang, X.; Zhuang, J.; Peng, Q.; Li, Y. *Nature* **2005**, *437,* 121.

(30) Gerbec, J. A.; Magana, D.; Washington, A.; Strouse, G. F. *J. Am. Chem. Soc.* **2005,** *127*, 15791.

(31) Mingos, D. M. P.; Baghurst, D. R. *Chem. Soc. Rev.* **1991**, *20*, 1.

(32) Dagani, R. *Chem. Eng. News* **1997**, *75*, 26.

(33) Rao, K. J.; Vaidhyanathan, B.; Ganguli M.; Ramakrishnan, P. A. *Chem. Mater.* **1999**, *11*, 882.

(34) Gallis, K.; Landry, C. *Adv. Mater.* **2001,** *13,* 23.

(35) Boxall, D.; Lukehart, C. *Chem. Mater.* **2001,** *13,* 806, 891.

(36) Zhu, J.; Palchik, O.; Chen, S.; Gedankan, A. *J. Phys. Chem. B.* **2000, 1**04, 7344.

(37) Liang, J.; Deng, Z. X.; Jiang, X.; Li, F.; Li, Y. *Inorg. Chem.* **2002,** *41,* 3602.

(38) Panda, A. B.; Glaspell, G.; El-Shall, M. S. *J. Am. Chem. Soc.* **2006**, *128,* 2790.

(39) Gao, X.; Cui, Y.; Levenson, R. M.; Chung, L. W. K.; Nie, S. *Nat. Biotechnol.* **2004**, *22*, 969.

(40) Brown, M. A.; Semelka, R. C. *MRI: Basic Principles and Applications*, Wiley-Liss, New York **2003**.

(41) Caravan, P; Ellison, J. J.; McMurry, T. J.; Lauffer, R. B. *Chem. Rev.* **1999**, *99*, 2293.

(42) Mendonca Dias, M. H.; Lauterbur, P. C. *Magn. Reson. Med.* **1986**, *3*, 328.

(43) Semelka, R. C.; Helmberger, T. K. *Radiology* **2001**, *218*, 27.

(44) Lee, J. H.; Huh, Y. M.; Jun, Y. W.; Seo, J. W.; Jang, J. T.; Song, H. T.; Kim, S.; Cho, E. J.; Yoon, H. G.; Suh, J. S.; Cheon, J. *Nat. Med.* **2007**, *13*, 95.

(45) Na, H. B.; Song, I. C.; Hyeon T. *Adv. Mater.* **2009**, *21*, 1.

(46) Jung, C. W.; Jacobs, P.; *Magn. Reson. Imaging* **1995**, *13*, 661.

(47) Wang, Y. X.; Hussain, S. M.; Krestin, G. P. *Eur. J. Radiol.* **2001**, *11*, 2319.

(48) Josephson, L.; Tung, C.H.; Moore, A.; Weissleder, R. *Bioconjugate Chem.* **1999**, *10*, 186.

(49) Xu, C.; Xie, J.; Ho, D. ;Wang, C.; Kohler, N.; Walsh, E. G.; Morgan, J. R.; Chin, Y. E.; Sun, S. *Angew. Chem. Int. Ed.* **2008**, *47*, 173.

(50) Jun, Y. W.; Seo, J. W.; Cheon, J. *Acc. Chem. Res.* **2008**, *41*, 179.

(51) Hadjipanayis, C. G.; Bonder, M. J.; Balakrishnan, S.; Wang, X.; Mao, H.; Hadjipanayis, G. C. *Small* **2008**, *4*, 1925.

(52) Jun, Y. W.; Huh, Y. M.; Choi, J. S.; Lee, J.-H.; Song, H. T.; Kim, S.; Yoon, S.; Kim, K. S.; Shin, J. S.; Suh, J. S.; Cheon, J. *J. Am. Chem. Soc.* **2005**, *127*, 5732.

(53) Choi, J. S.; Jun, Y. W.; Yeon, S. I.; Kim, H. C.; Shin, J. S.; Cheon, J. *J. Am. Chem. Soc.* **2006**, *128*, 15982.

(54) Harisinghani, M. G.; Barentsz, J.; Hahn, P. F.; Deserno, W. M.; Tabatabaei, S.; van de Kaa, C. H.; de la Rosette, J.; Weissleder, R. *N. Engl. J. Med.* **2003**, *348*, 2491.

(55) Chang, R. K.; Furtak, T. E. *Surface Enhanced Raman Scattering*; Plenum Press: New York, 1982.

(56) Moskovits, M. *Re*V. *Mod. Phys.* **1985**, *57*, 783.

(57) Kneipp, K.; Wang, Y.; Kneipp, H.; Perelman, L. T.; Itzkan, I.; Dasari, R. R.; Feld, M. S. *Phys. Re*V. *Lett.* **1997**, *78*, 1667.

(58) Nie, S.; Emory, S. R. *Science* **1997**, *275*, 1102.

(59) Li, W.-H.; Li, X.-Y.; Yu, N.-T. *Chem. Phys. Lett.* **1999**, *312*, 28.

(60) Campion, A.; Gallo, A. R.; Harris, C. B.; Robota, H. J.; Whitmore, P. M. *Chem. Phys. Lett.* **1980**, *73*, 447.

(61) Ku¨mmerlen, J.; Leitner, A.; Brunner, H.; Aussenegg, F. R.; Wokaun, A. *Mol. Phys.* **1993**, *80*, 1031.

(62) Sokolov, K.; Chumanov, G.; Cotton, T. M. *Anal. Chem.* **1998**, *70*, 3898.

(63) Lakowicz, J. R. *Anal. Biochem.* **2001**, *298*, 1.

(64) Lakowicz, J. R.; Shen, Y.; D'Auria, S.; Malicka, J.; Fang, J.; Gryczynski, Z.; Gryczynski, I. *Anal. Biochem.* **2002**, *301*, 261.

(65) DeSaja-Gonzalez, J.; Aroca, R.; Nagao, Y.; DeSaja, J. A. *Spectrochim. Acta Part A* **1997**, *53*, 173.

(66) Geddes, C. D.; Lakowicz, J. R. *J. Fluoresc.* **2002**, *12*, 121.

(67) Aroca, R. F.; Constantino, C. J. L. *Langmuir* **2000**, *16*, 5425.

(68) Dos Santos, D. S., Jr.; Aroca, R. F. *Analyst* **2007**, *132*, 450.

(69) Ray, K.; Badugu, R.; Lakowicz, J. R. *J. Am. Chem. Soc.* **2006**, *128*, 8998.

(70) Malicka, J.; Gryczynski, I.; Kusba, J.; Lakowicz, J. R. *Biopolymers* **2003**, *70*, 595.

(71) Smith, D. S.; Kostov, Y.; Rao, G. *Sens. Actuators, B: Chem.* **2007**, *127*, 432.

(72) Bruchez, M., Jr.; Moronne, M.; Gin, P.; Weiss, S.; Alivisatos, A. P. *Science* **1998**, *281*, 2013.

(73) Chan, W. C. W.; Nie, S. *Science* **1998**, *281*, 2016.

(74) Ow, H.; Larson, D. R.; Srivastava, M.; Baird, B. A.; Webb, W. W.; Wiesner, U. *Nano Lett.* **2005**, *5*, 113.

(75) Gong, J-L.; Jiang, J-H.; Liang, Y.; Shen, G-L.; Yu, R-Q. *J. Coll. Inter. Sci.* **2006**, *298*, 752.

(76) Wang, L.; Yang, C.; Tan, W. *Nano Lett.* **2005**, *5*, 37.

(77) Aslan, K.; Leonenko, Z.; Lakowicz, J. R.; Geddes, C. D. *J. Fluoresc.* **2005**, *15*, 643.

(78) Aslan, K.; Malyn, S. N.; Geddes, C. D. *J. Fluoresc.* **2007**, *17*, 7.

(79) Aslan, K.; Lakowicz, J. R.; Geddes, C. D. *Anal. Chem.* **2005**, *77*, 2007.

(80) Zhang, Y.; Aslan, K.; Previte, M. J. R.; Geddes, C. D. *Appl. Phys. Lett.* **2007**, *90*, 173116.

(81) Pribik, R.; Aslan, K.; Zhang, Y.; Geddes, C. D. *J. Phys. Chem. C* **2008**, *112*, 17969.

(82) Kadir Aslan, M. J. R. P.; Yongxia, Z.; Geddes, C. D. *J. Phys. Chem. C* **2008**, *112*, 18368.

(83) Aslan, K.; Lakowicz, J. R.; Geddes, C. D. *Anal. Bioanal. Chem.* **2005**, *382*, 926.

(84) Zhang, Y.; Aslan, K.; Previte, M. J.; Geddes, C. D. *J. Fluoresc.* **2007**, *17*, 627.

(85) Zhang, Y.; Dragan, A.; Geddes C. D. *J. Phys. Chem. C* **2009,** *113,* 12095.

(86) Geddes, C. D.; Lakowicz, J. R. *J. Fluoresc.* **2002**, *12*, 121.

(87) Allen, T. M.; Cullis, P. R. *Science* **2004**, *303*, 1818.

(88) Nimesh, S.; Manchanda, R.; Kumar, R.; Saxena, A.; Chaudhary, P.; Yadav, V.; Mozumdar, S.; Chandra, R. *Int. J. Pharm.* **2006**, *323*, 146.

(89) Soppimath, K.; Aminabhavi, T. M.; Kulkarni, A. R.; Rudzinski, W. E.; *J. Controlled Release* **2001**, *70*, 1.

(90) Jung, T.; Kamm, W.; Breitenbach, A.; Kaiserling, E.; Xiao, J. X.; Kissel, T. *Eur. J. Pharm. Biopharm.* **2000**, *50*, 147.

(91) Italia, J. L.; Bhatt, D. K.; Bhardwaj, V.; Tikoo, K.; Ravi Kumar, M. N. V. *J. Controlled Release* 2007, 119, 197.

(92) Sahoo, S. K.; Labhasetwar, V. *Drug Discovery Today*, **2003**, *8*, 1112.

(93) Panyam, J.; Labhasetwar, V. *Adv Drug Delivery Rev*, **2003**, *55*, 329.

(94) Lai, C. Y.; Trewyn, B. G.; Jeftinija, D. M.; Jeftinija, K.; Xu, S.; Jeftinija, S.; Lin, V. S. Y. *J. Am. Chem. Soc.* **2003**, *125*, 4451.

(95) Giri, S.; Trewyn, B. G.; Stellmaker, M. P.; Lin, V. S. Y. *Angew. Chem. Int. Ed.* **2005**, *44*, 5038.

(96) Yang, Q.; Wang, S. H.; Fan, P. W.; Wang, L. F.; Di, Y.; Lin, K. F.; Xiao, F. S. *Chem. Mater.* **2005**, *17*, 5999.

(97) Zhang, J.; Misra, R. D. K. *Acta Biomat.* **2007**, *3*, 838.

(98) Oberdorster, G. Oberdorster, E. Oberdorster, J. *Environ. Health Perspect.* **2005**, *113*, 823.

(99) Grainger, D. W.; Castner, D. G. *Adv. Mater*. **2008**, *20*, 867.

(100) Russell, R. *Neurosci. Biobehav. Rev.* **1991**, *15,* 7.

(101) Parng, C. *Curr. Opin. Drug Discovery Dev.* **2005**, *8*, 100.

(102) Teraoka, H.; Dong, W.; Hiraga, T. *Congenital Anomalies* **2003**, *43*, 123.

(103) Rubinstein, A. L. *Expert Opin. Drug Metab. Toxicol.* **2006**, *2*, 231.

(104) Fako, V. E.; Furgeson D. Y. *Adv. Drug Delivery Rev.* **2009**, *61*, 478.

(105) Pyati, U. J.; Look, A. T.; Hammerschmidt, M. *Semin. Cancer Biol.* **2007**, *17*, 154.

(106) Spitsbergen, J. M.; Kent, M. L. *Toxicol. Pathol.* **2003**, *31 Suppl*, 62.

(107) Langheinrich, U. *BioEssays* **2003**, *25*, 904.

(108) Rubinstein, A. L. *Curr. Opin. Drug Discovery Dev.* **2003**, *6*, 218.

(109) Zon, L. I.; Peterson, R. T. *Nat. Rev. Drug Discovery* **2005**, *4*, 35.

(110) Bar-Ilan, O.; Albrecht, R. M.; Fako, V. E.; Furgeson, D. Y. *Small* **2009**, *5*, 1897.

(111) Zhu, X.; Zhu, L.; Duan, Z.; Qi, R.; Li, Y.; Lang, Y. *J. Environ. Sci. Health A Toxicol. Hazard. Subst. Environ. Eng.* **2008**, *43*, 278.

(112) Griffitt, R.; Weil, R.; Hyndman, K.; Denslow, N.; Powers, K.; Taylor, D.; Barber, D. *Environ. Sci. Technol.* **2007**, *41,* 8178.

Chapter Two

Magnetic Nanochains of $FeNi_3$ Prepared by a Template-Free Microwave-Hydrothermal Method

2.1 Introduction

One-dimensional (1D) nanostructures have drawn great attention in recent years because of their distinctive geometries and special optical, photoelectric, and electrochemical properties.[1-5] In particular, 1D magnetic nanochains have stimulated interests in many research fields such as electrical transport, magnetic switching,[6] magnetotransport behavior,[7] micromechanical sensors,[8] DNA separation, and other biomedical applications.[9-11] In comparison to the zero-dimensional nanoparticles, 1D nanochains provide more parallel-aligned surface functionalities per molecular structure, which are suitable for multivalent molecular recognition on cell surfaces.[11] Macrophage cells may take up the 1D nanochains more rapidly than nanoparticles by

their differences in mass.[12] Transition metal alloys have been extensively studied in the past several decades for their increasing utility in electronic and energy conversion devices.[13] Alloys form when two or more metals coaggregate to produce compositionally ordered structures, with properties that differ from those of bulk alloys or nanoparticles of the individual components.[14-17] This makes magnetic alloy nanoparticles particularly interesting because of their high saturation magnetization[18] and resistance against oxidation.[19] As important transition alloys, iron-nickel alloys, such as $FeNi_3$, are of great interest due to their useful magnetic properties and wide applications.[20-24] Owing to the distinctive 1D intrinsic anisotropic shape, comparing to the zero-dimensional nanoparticles, these $FeNi_3$ nanochains are expected to exhibit enhanced magnetic coercivity and saturation magnetization and can be used as a new class of MRI probes with high sensitivity. However, up to now, there are only several methods to prepare the $FeNi_3$ nanoparticles, such as electrical explosion of wire,[21] chemical reduction using hydrazine in aqueous solutions.[22-24] The methods reported are either time-consuming, or they require additional surfactant or template. And the reported $FeNi_3$ does not have a regular shape or an ordered structure.

Herein, we report a rapid and economical microwave-assisted approach to fabricate awaruite $FeNi_3$ nanochains in ethylene glycol solution at one step, as shown in Scheme 2.1. Microwave irradiation is an efficient process that becomes an increasingly popular heating method for nanomaterials synthesis.[25-27] We have successfully synthesized colloidal Fe_2O_3 nanocrystals,[28] carbon-based interconnected cable-like Ag/C,[29] Ni nanowires[29] and superparamagnetic porous Fe_3O_4/C

nanocomposites[31] by taking advantage of microwave irradiation and hydrothermal effects. In this chapter, the $FeNi_3$ nanochains were synthesized within several minutes without using any hard templates or catalysts. The structure, morphology and composition of the nanochain products are investigated by changing the experiment conditions, such as the amounts of precursors, the relative ratio of Fe and Ni precursors and the solvent. The biocompatibility of the product is tested by exposing the zebrafish larvae to the product solution. And the potential application of the product as the MRI probes is also studied. It is expected that the unique shape of these nanostructures can find applications for cell labeling, as drug carrier, magnetic separation of labeled cells and other biological entities, and also in the application of magnetic targeting .[12]

Scheme 2.1. Illustration of a Proposed Mechanism for the Formation of $FeNi_3$ Nanochains

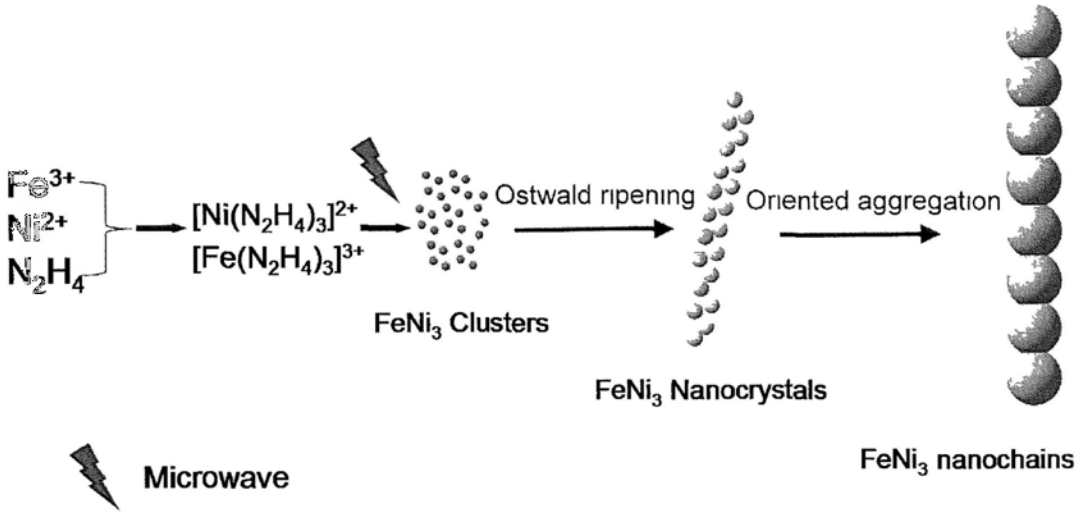

2.2 Experimental Section

2.2.1 Reagents.

Iron(III) acetylacetonate ($Fe(acac)_3$, 95%), nickel(II) acetylacetonate ($Ni(acac)_2$, 95%), ethylene glycol (EG, 99.8%), triethylene glycol (TEG, 99%), hydrazine monohydrate (98%) were supplied by Aldrich. Deionized water was used throughout. All chemicals were used as received without further purification.

2.2.2 Synthesis of necklace-like $FeNi_3$ nanochains.

All the samples were prepared in a microwave digestion system (Ethos TC Plus 1, Milestone). The detailed conditions are listed in Table 2.1. In a typical procedure, 0.07 mmol iron(III) acetylacetonate and 0.2 mmol nickel(II) acetylacetonate were dissolved into 45mL ethylene glycol, and then 1mL of hydrazine monohydrate was added dropwise by an auto-pipette over an one-minute period. After stirring mildly for about 5 min, the solution was sealed in a high-pressure digestion vessel which was Teflon-lined and double-walled. The reaction vessel was fitted with a temperature probe that was housed in a sturdy thermowell and protected from chemical attack by a triple layer of PTFE/ceramic/PTFE. The desired exposure time and temperature were programmed by using Milestone's EasyControl software. The Automatic Temperature Control system allowed continuous monitoring and controlling (±1℃) of the internal temperature. The preset profile (desired time and temperature) was followed automatically by continuously adjusting the applied power (0-1000 W) in order to keep the reaction temperature at 160℃. After treating the mixture at 160℃ for 5 min under microwave irradiation, the vessel was cooled to room temperature. The product was collected, washed with deionized water and absolute ethanol, and dried in a vacuum at 60℃ for 4 hours.

2.2.3 Characterization of necklace-like $FeNi_3$ nanochains.

The general morphology of the products was characterized by a field-emission scanning electron microscope (FESEM, FEI, Quanta 400 FEG). Transmission

electron microscopy (TEM, FEI/PHILIPS CM120), high-resolution TEM (HRTEM), and high angle annular dark field scanning TEM (HAADF-STEM) measurements were carried out on a Tecnai F20 microscope (FEI, 200 kV) coupled with an HAADF detector and an energy-dispersive X-ray (EDX) spectrometer. Two-dimensional STEM-EDX elemental mapping was performed for the $FeNi_3$ product. The electron probe size for the STEM-EDX analysis was about 1 nm. X-ray diffraction (XRD) patterns were collected using a Bruker D8 Advance diffractometer using Cu Kα irradiation (λ =1.5406 Å). Powdered products were weighed out for magnetic characterization by vibrating sample magnetometry (VSM-7300, Lakeshore, U.S.A.)

2.2.4 Toxicity test—Exposure of the zebrafish (*Danio rerio*) larvae to $FeNi_3$ nanochains.

For toxicity studies, 20 healthy zebrafish larvae (5 day post-fertilization and hatched) were transferred to a 100 ml polyethylene beaker containing 50 ml of a solution prepared by dissolving 60 mg of artificial sea salt in one liter of ultrapure (deionized and purified after reverse osmosis) water. All fish rearing conditions and larval production procedures were carried out according to Westerfield[32] and the bioassay was performed according to the OECD recommended method.[33] Graded concentrations of $FeNi_3$ nanochains (0, 1, 5, 10, 25, 35, 50 mg/L) were sonicated and incubated for 96 h at 28.5°C. Tests were performed six times (120 larvae per concentration). The survival rate is expressed as the total number of survival larvae after 24, 48 and 96 h.

2.2.5 *In vitro* MRI of $FeNi_3$ nanochains.

MR relaxometry of the $FeNi_3$ nanochains was performed using a clinical 1.5 T

whole-body MR system (Siemens Sonata, Erlangen, Germany) in combination with a knee radio frequency coil for excitation and signal reception. $FeNi_3$ nanochains were dispersed in distilled water at iron concentrations ranging from 0 to 0.2 mmol/L. For MR measurements, $FeNi_3$ nanochains dispersed solutions (1 mL) were filled in each 1.5 mL Eppendorf tubes. Sonication was applied for 10 min prior to MRI using at 40 kHz (Branson 3510E-MTH) in water at ambient temperature. T_2 relaxation times were measured using a standard Carr-Purcell-Meiboom -Gill pulse sequence (TR = 2000 msec, TE range = 30-960 msec, 32 echoes, FOV = 134 × 67 mm, matrix = 128 × 64, slice thickness = 5 mm, NEX = 3). T_2 relaxation times were calculated by a linear fit of the logarithmic ROI signal amplitudes versus TE. The T_2 relaxivity (r_2) was determined by a linear fit of the inverse relaxation times as a function of the iron concentrations used.

2.3 Results and discussion

Black powders were obtained from the microwave-assisted reaction of ethylene glycol iron (III) acetylacetonate and nickel (II) acetylacetonate. Figure 2.1 shows the X-ray diffraction (XRD) pattern of a typical product. All peaks can be indexed to the awaruite $FeNi_3$ alloy, which is in good agreement with the reported data (Joint Committee on Powder Diffraction Standards, JCPDS card no.: JCPDS 38-0419). No iron and nickel oxides or hydroxides or other impurity phases are detected. The sharp

peaks and the low background reveal that the as-synthesized iron-nickel alloy particles had a high degree of crystallinity. This indicates that well-crystallized $FeNi_3$ nanochains can be easily obtained under the proposed preparation conditions.

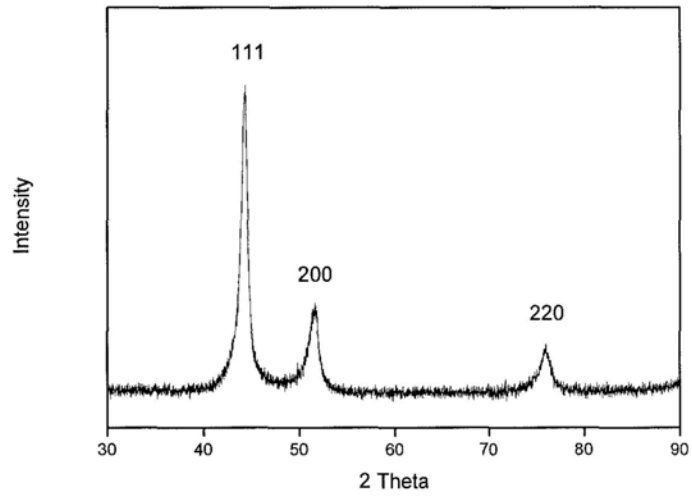

Figure 2.1 XRD patterns of the as-prepared $FeNi_3$ nanochains (S1).

The morphology of the as-obtained products was characterized by FESEM and TEM. A general overview FESEM image in Figure 2.2a shows that the product is composed of nanochains with a diameter of 150 nm and length about several tens of micrometers. Enlarged FESEM images (Figure 2.2b) show that the nanochains are comprised of many aligned nanospheres. Representative TEM images (Figure 2.3a) clearly show the shape of necklace-like nanochains, and a high-magnification TEM image (Figure 2.3b) shows that the chain is necklace-like and the diameter of each nanosphere is about 150 nm. An electron diffraction (ED) pattern (Figure 2.3c) was recorded by focusing the electron beam on an individual nanochain. The results

suggest that the products are polycrystalline. Figure 3d shows a HRTEM image at the edge of an individual $FeNi_3$ nanosphere. As shown in Figure 2.3d, a typical intensity profile covers the line scan (labeled by a line in Figure 2.3e) across the lattice fringes. The periodic fringe spacing of ~2.0 Å agrees well with interplanar spacing between the {111} planes of the awaruite $FeNi_3$. The local elemental composition of the as-formed nanochains was studied by EDX microanalysis at the single-nanochain level, shown in Figure 2.4. It confirms that the nanochains are composed of Fe and Ni elements. Figure 2.5a-d show the typical high angle annular dark field scanning TEM (HAADF-STEM) and EDX elemental mapping images of an individual nanochain. The results confirm the existence of Fe and Ni elements, which are distributed homogenously over the entire nanochains.

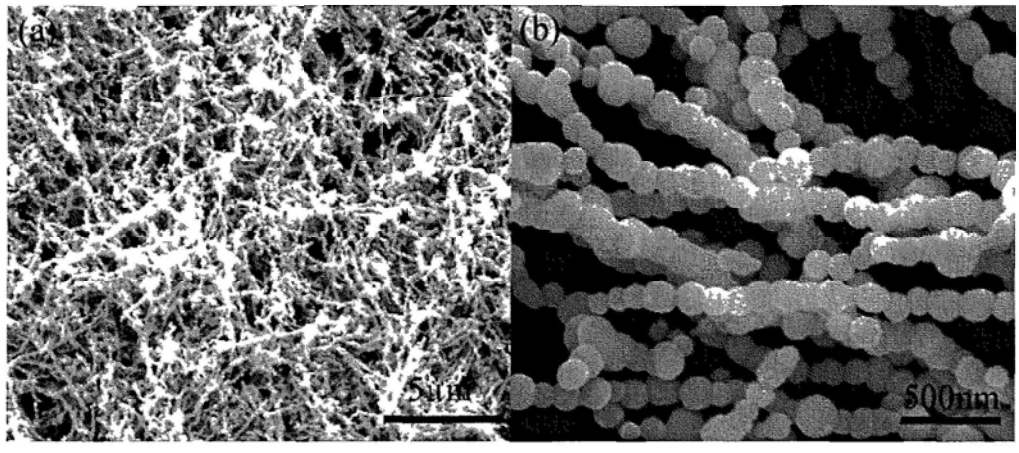

Figure 2.2 (a) Low- and (b) high-magnification FESEM images of S1

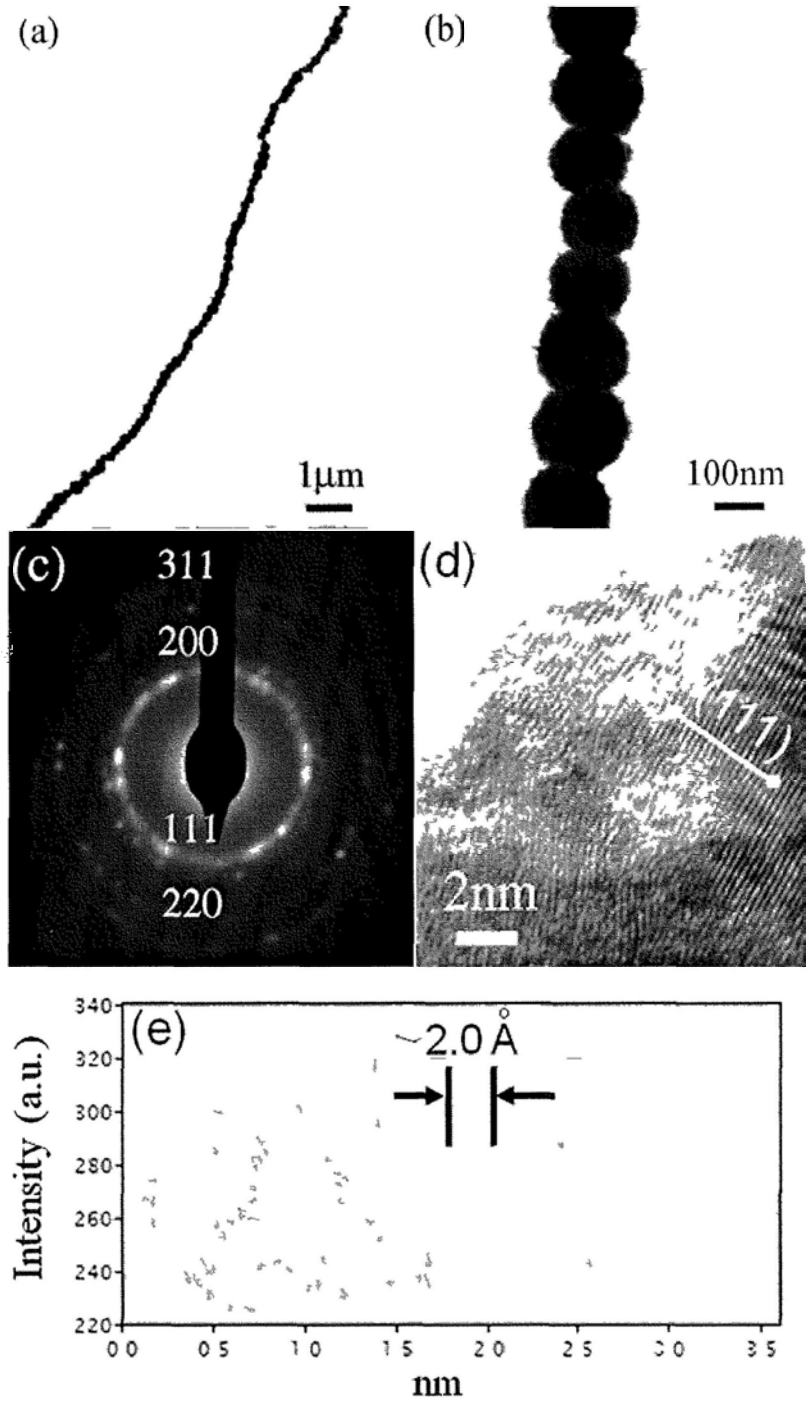

Figure 2.3 (a, b) Bright-field TEM and enlarged TEM image of S1. (c) ED pattern indicating the polycrystalline nature of the nanochains. (d) Typical HRTEM image. (e) Corresponding intensity profile for the line scan across the lattice fringes.

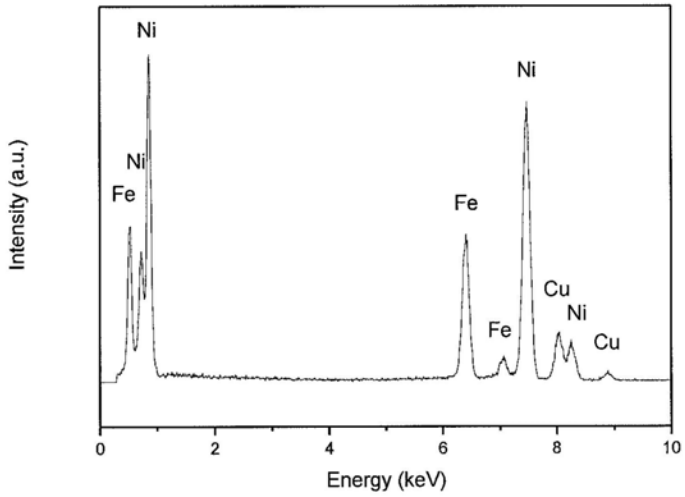

Figure 2.4 EDX spectrum of a single $FeNi_3$ nanochain from S1, where the signals of Cu are generated from the Cu grids.

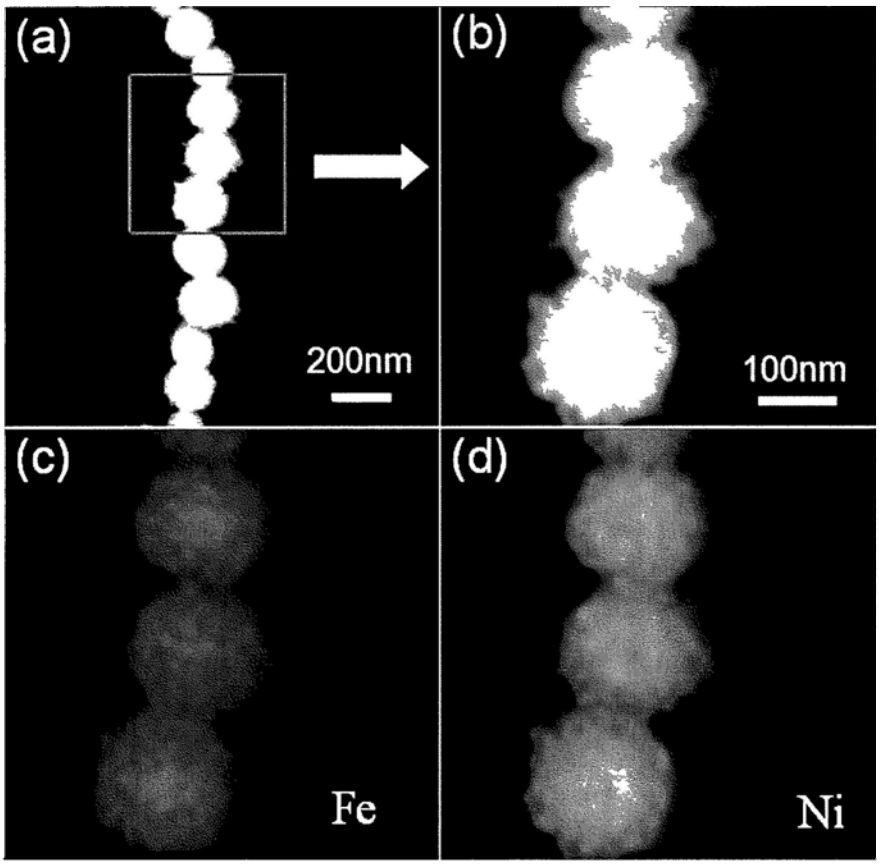

Figure 2.5 (a, b) HAADF-STEM and (c, d) elemental mapping images of a single $FeNi_3$ nanochain.

The magnetic properties of the products were characterized by VSM. Figure 6 shows the room-temperature magnetization hysteresis loop. Clearly, it reveals a typical ferromagnetic behavior with saturation magnetization (Ms) of 53.6 emu g^{-1} and coercivity field (Hc) of 53.0 Oe. The hysteresis curve is symmetric in shape with respect to zero magnetic field. It is worth noting that the $FeNi_3$ nanochains exhibit significantly enhanced magnetic coercivity (about 100 times higher) compared with that of bulk $FeNi_3$ (0.54 Oe), and the saturation magnetization is about 350 times higher than the monodispersed $FeNi_3$ nanospheres (0.15 emu g^{-1}).[22] This may be ascribed to the distinctive 1D anisotropic structure and hierarchical surfaces of the magnetic nanochains. Figure 2.7 also shows a fast response to a foreign magnet and can be rapidly separated from the solution.

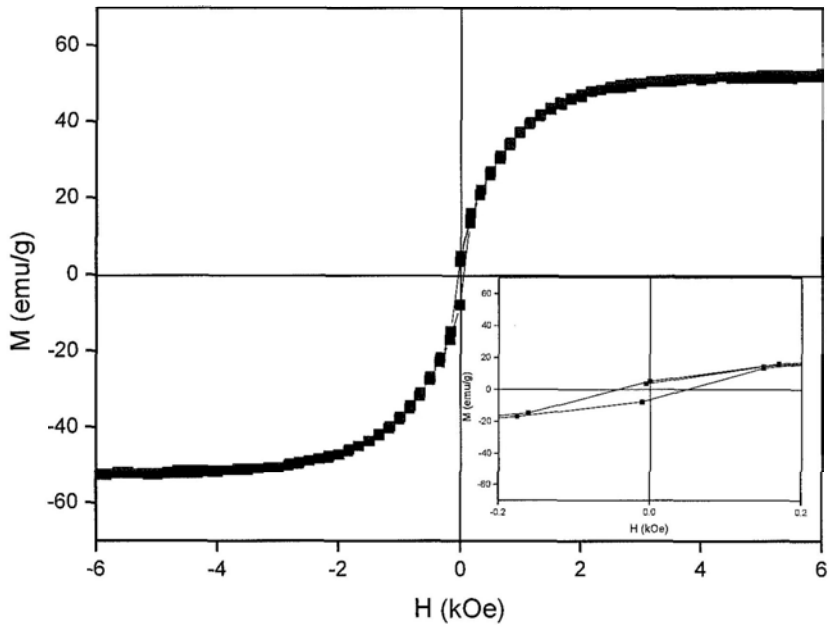

Figure 2.6 The hysteresis loops of the $FeNi_3$ nanochains (S1) at 300 K.

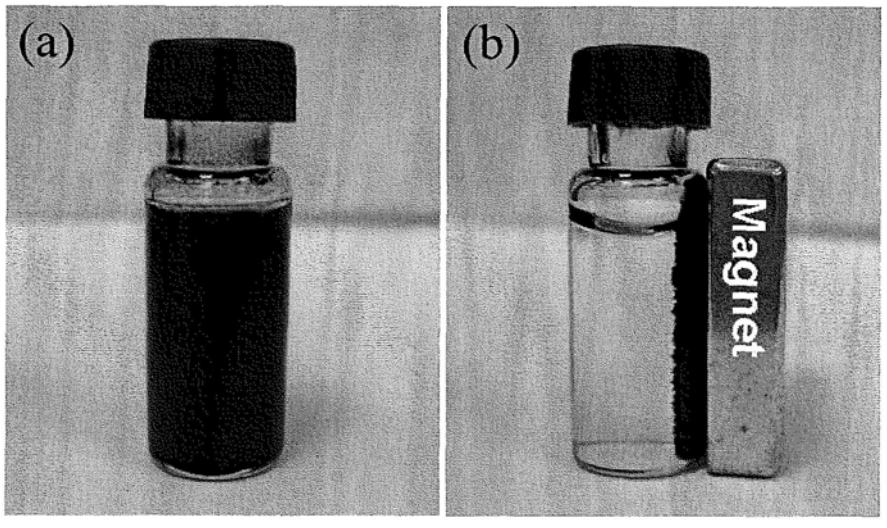

Figure 2.7 (a), (b) Photograph of the $FeNi_3$ nanochains dispersed in the water and response to external magnetic field.

We further investigated the effects of reactant concentration and solvents on the morphology of the $FeNi_3$ products. Results are summarized in Table 2.1. The amounts of ($Fe(acac)_3$:$Ni(acac)_2$) had a significant effect on the size of the as-prepared $FeNi_3$ nanochains. When the amounts of $Fe(acac)_3$:$Ni(acac)_2$ were increased from 0.07 mmol:0.2 mmol to 0.17 mmol:0.50 mmol (fixed the molar ratio of Fe:Ni = 1:3), the sizes of nanospheres in each nanochain increased from 150 nm to 550 nm in diameter (Figure 2.8a-c). This is responding to the more mass transfer for the growth of the crystal with a higher concentration of the precursor. The molar ratio of Fe:Ni ($Fe(acac)_3$:$Ni(acac)_2$) also play a key role in the morphology of the product. At a molar ratio of 1:0.33, most of the structures were nanospheres. However, when the molar ratio was changed from 1:0.33 to 1:3 (Figure. 2.9a-f), pure nanochain structures were obtained. In the absence of an iron precursor, pure Ni nanowires were formed (Figure 2.9g-h). The effect of solvent was also studied (Figure 2.10a, b). When EG was replaced by TEG, ultrafine nanopartiles were obtained.

Table 2.1 Experimental conditions for the preparation of $FeNi_3$ nanostructures

Sample No.	$Fe(acac)_3$	$Ni(acac)_2$	Molar ratio Fe:Ni	solvent	Morphology
	[mmol]	[mmol]	[mmol:mmol]		
S1	0.07	0.20	1:3	EG	chain
S2	0.10	0.30	1:3	EG	chain
S3	0.13	0.40	1:3	EG	chain
S4	0.17	0.50	1:3	EG	chain
S5	0.20	0.07	1:0.33	EG	chain + particle
S6	0.27	0.20	1:0.75	EG	chain + particle
S7	0.20	0.20	1:1	EG	chain + particle
S8	0.10	0.20	1:2	EG	chain
S9	0	0.20	0:1	EG	wire
S10	0.07	0.20	1:3	TEG+EG	chain + particle
S11	0.07	0.20	1:3	TEG	particle

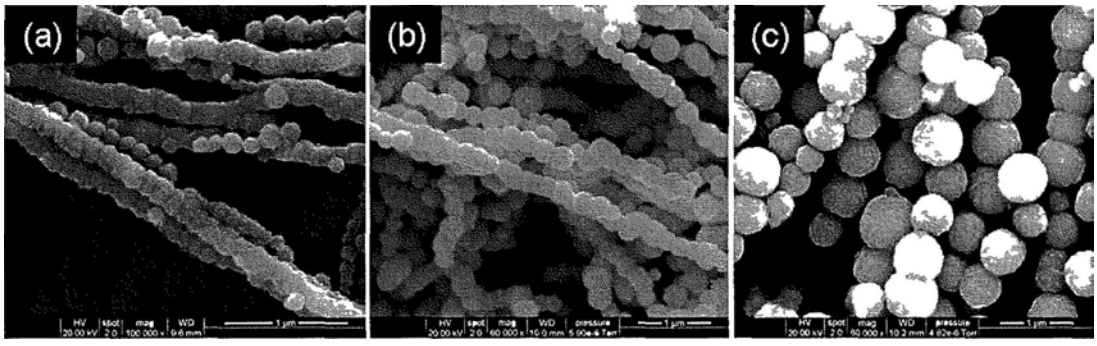

Figure 2.8 FESEM images of the products (S2-S4) prepared by the microwave irradiation 160℃ for 5min, with different amounts of $Fe(acac)_3$ /$Ni(acac)_2$ at the molar ratio of Fe:Ni = 1:3 (mmol/mmol). (a) 0.10:0.3, (b) 0.13:0.40, (c) 0.17:0.50.

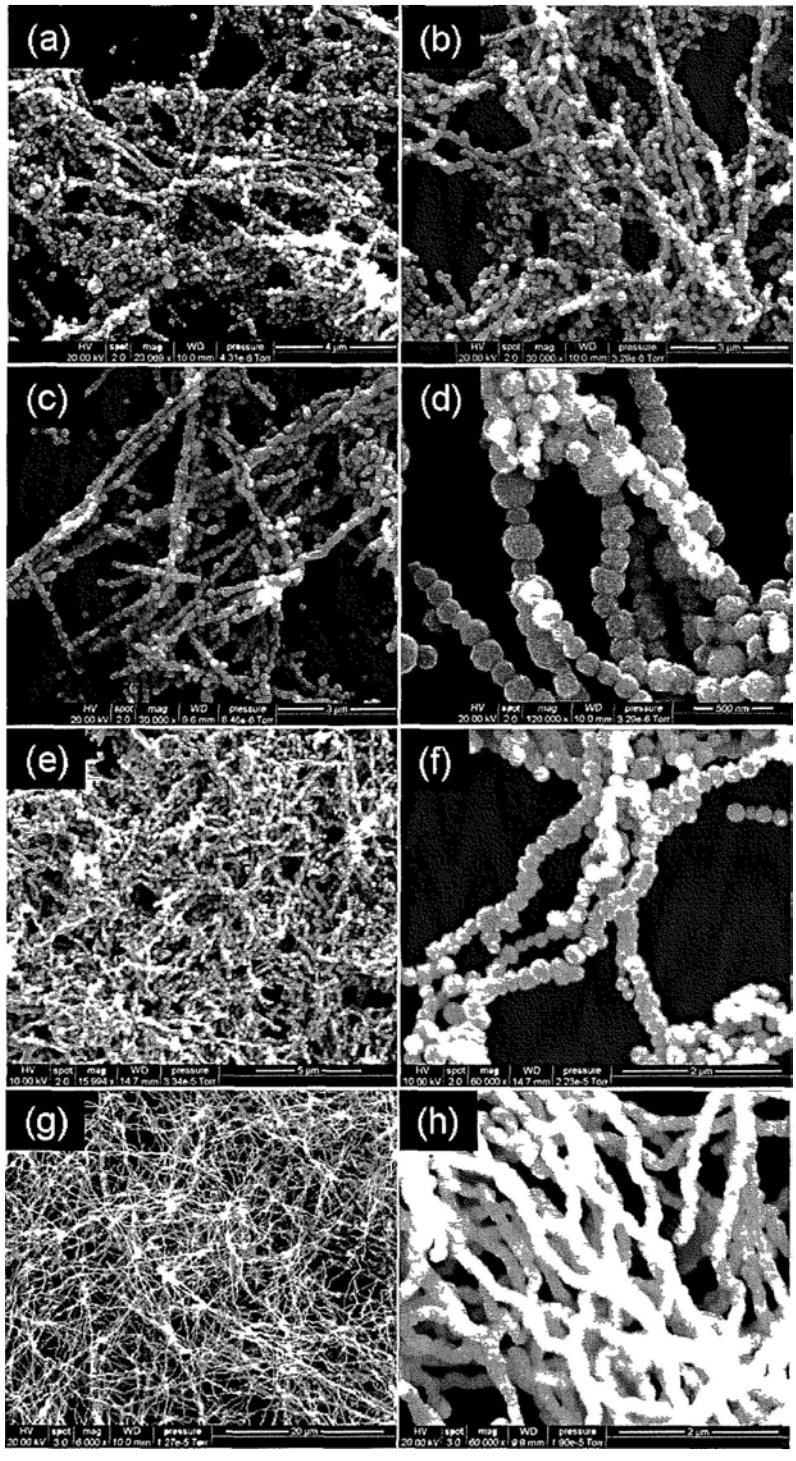

Figure 2.9 FESEM images of the products (S5-S9) with different molar ratios molar ratios of Fe:Ni ($Fe(acac)_3$: $Ni(acac)_2$) (mmol/mmol). (a) 1:0.33, (b) 1:0.75, (c, d) 1:1, (e, f) 1:2, (g, h) 0:1.

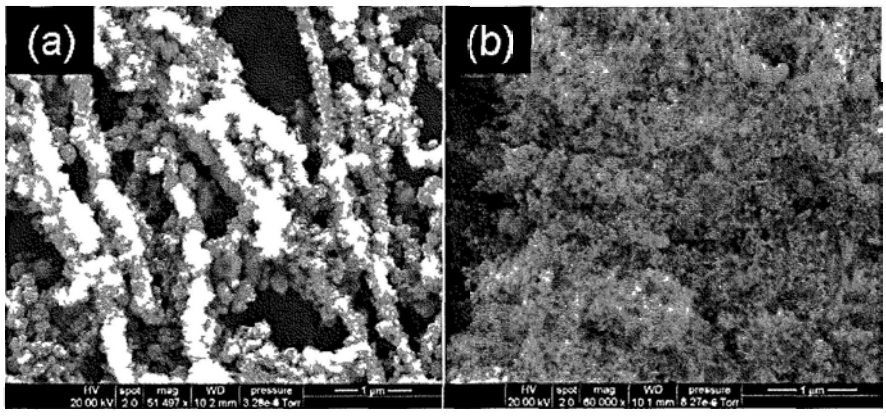

Figure 2.10 SEM images of the $FeNi_3$ products prepared in 20ml TEG + 25ml EG (a, S10) and 45ml TEG (b, S11).

Figures 2.2 and 2.3 reveal that the nanospheres in nanochains are made up of small crystallites and have a rough surface. It is known that a dark blue complex of $[Fe(N_2H_4)_3]^{3+}$ and $[Ni(N_2H_4)_3]^{2+}$ is formed by reacting Fe^{3+} and Ni^{2+} in a hydrazine solution,[29] the excess hydrazine reduces the $[Fe(N_2H_4)_3]^{3+}$ and $[Ni(N_2H_4)_3]^{2+}$ complex into Fe and Ni nuclei under microwave irradiation. Here it is because hydrazine is a moderate reducing agent with low-cost and has been proved to be good alternative to produce metallic particles.[23] Owing to the excellent microwave absorbing characteristics of the polar glycol and metallic $FeNi_3$, "hot spots" in the bulk solution and "hot surfaces" on metallic $FeNi_3$ can be created. They would speed up mass transfer and crystal growth. Microwave irradiation would also induce localized ionic currents on the "hot surface" of $FeNi_3$ in an alternating electromagnetic field, providing additional driving force for directional crystallographical fusion of nuclei into nanocystals. The crystallites attach to each other probably driven by the "oriented

attachment" mechanism associate with Ostwald ripening[34] and grow into a chain due to the attractive magnetic forces between the magnetic particles as well as van der Waals interactions.[35]

While rapid development of nanomaterials will certainly continue, the application of these materials will be limited by their inherent toxicity.[36,37] Thus, the need for evaluating nanotoxicity is becoming increasingly paramount. Transparent zebrafish, possessing a high degree of homology to the human genome, offers an economically feasible platform for noninvasive real-time assessments of nanotoxicity.[38] The biocompatibility of the as-prepared $FeNi_3$ alloyed nanochains were evaluated using zebrafish as a model. Figure 2.11 shows in detail the survival rate of zebrafish larvae at different concentrations of nanochains (0, 1, 5, 10, 25, 35, 50 mg/L) after 96h exposure. It shows that more than 90% zebrafish larvae survived even under the highest concentration 50 mg/L. These results confirm that the $FeNi_3$ nanochains are of good biocompatibility. Figure 2.12 shows *in vitro* MRI of $FeNi_3$ nanochains (S1) suspended in DI water at the different concentrations of nanochains (0, 0.001, 0.002, 0.005, 0.01, 0.02, 0.05, 0.1, 0.2mM). The $FeNi_3$ nanochains resulted in signal decrease in a concentration dependant manner, with higher concentration leading to darker signal. The r_2 relaxivity is 7.1 $s^{-1}mM^{-1}$ calculated from Figure 2.13. At TE=92 msec, the detection limit is 0.002 mM (Figure 2.12) which compared favorably the commercial iron oxide nanoparticles.[39,40] These results demonstrate that this kind of alloy nanochains has the potential to be used as a T_2 MRI contrast agent.

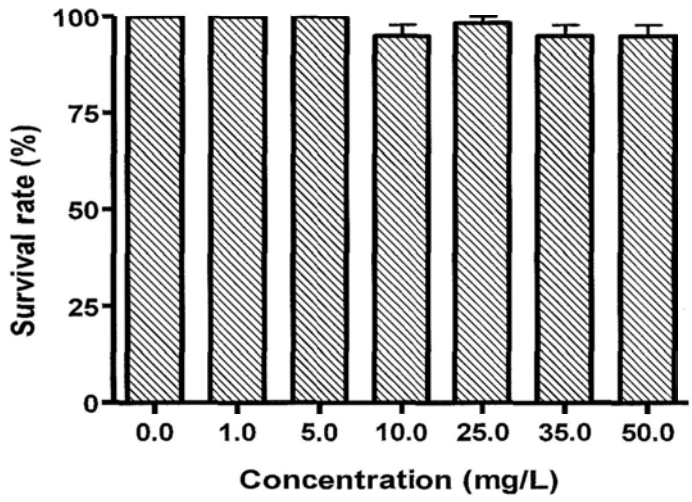

Figure 2.11 The survival rate of zebrafish larvae at different $FeNi_3$ nanochains (S1) concentrations after 96h exposure.

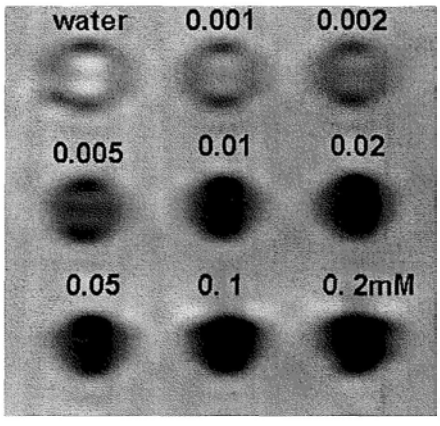

Figure 2.12 T_2-weighted magnetic resonance spin echo images of the prepared $FeNi_3$ nanochains (S1) in DI water (1.5Tesla, TR = 2000 msec, TE=92 msec).

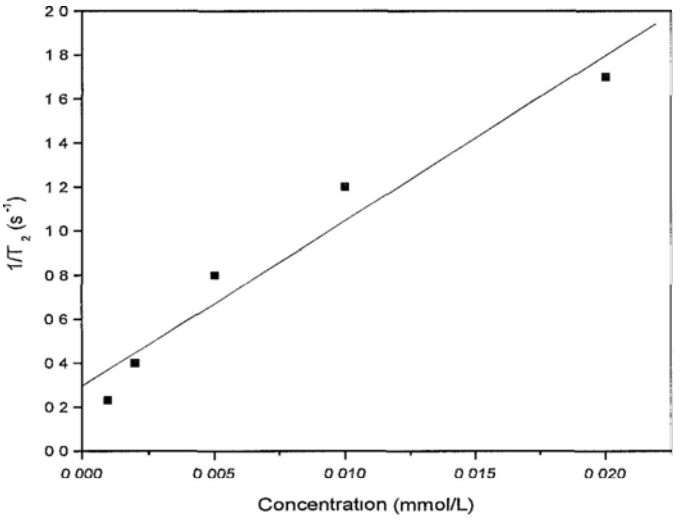

Figure 2.13 r_2 relaxivity of the prepared $FeNi_3$ nanochains (S1) in DI water (1.5Tesla, TR = 2000 msec, TE=92 msec).

2.4 Conclusions

In summary, we have reported a rapid and economical microwave-assisted route to synthesize $FeNi_3$ alloyed nanochains. The diameter of the chains can be tuned by changing the concentration of the precursors, iron(III) acetylacetonate and nickel(II) acetylacetonate. The prepared $FeNi_3$ alloyed nanochains show remarkably enhanced coercivity and saturation magnetization. This new materials can be used as efficient and sensitive MRI probes. In addition, the present synthetic method and growth

mechanism might be extended to other magnetic substances to direct large-scale synthesis of similar nanochains.

2.5 References

(1) Zhou, Y.; Kogiso, M.; Shimizu, T. *J. Am. Chem. Soc.* **2009**, *131,* 2456.

(2) Gu, Y. X.; Chen, D. R.; Jiao, X. L.; Liu, F. F. *J. Mater. Chem.* **2006,** *16,* 4361.

(3) Jin, Y.; Yang, D. Y.; Kang, D. Y.; Jiang, X. Y. *Langmuir* **2010**, *26,* 1186.

(4) Zeng, J.; Huang, J. L.; Lu, W.; Wang, X. P.; Wang, B.; Zhang, S. Y.; Hou, J. G. *Adv. Mater.* **2007**, *19,* 2172.

(5) Tao, X. Y.; Liu, J.; Koley, G.; Li, X. D. *Adv. Mater.* **2008**, *20,* 4091.

(6) Sudfeld, D.; Wojczykowski, K.; Hachmann, W.; Heitmann, S.; Rott, K.; Hempel, T.; Kammerer, S.; Jutzi, R.; Hutten, A.; Reiss, G. *IEEE Trans. Magn.* **2002**, *38*, 2601.

(7) Kinsella, J. M.; Ivanisevic, A. *J. Phys. Chem. C* **2008**, *112*, 3191.

(8) Goubault, C.; Jop, P.; Fermigier, M.; Baudry, J.; Bertrand, E.; Bibette, J. *Phys. Rev. Lett.* **2003**, *91*, 260802.

(9) Doyle, P. S.; Bibette, J.; Bancaud, A.; Viovy, J. L. *Science* **2002**, *295*, 2237.

(10) Koenig, A.; Hebraud, P.; Gosse, C.; Dreyfus, R.; Baudry, J.; Bertrand, E.; Bibette, J. *Phys. Rev. Lett.* **2005**, *95,* 128301.

(11) Park, J. H.; von Maltzahn, G.; Zhang, L. L.; Schwartz, M. P.; Ruoslahti, E.; Bhatia, S. N.; Sailor, M. J. *Adv. Mater.* **2008**, *20*, 1630.

(12) Leung, K. C. F.; Wang, Y. X.; Wang, H. H.; Chak, C. P.; Cheng, C. H. K. *IEEE Trans. on Nanobioscience* **2009**, *8*,192.

(13) Tremel, W.; Kleinke, H.; Derstroff, V.; Reisner, C. *J. Alloys Compd.* **1995**, *219*,

73.

(14) Sun, S. H.; Anders, S.; Hamann, H. F.; Thiele, J. U.; Baglin, J. E. E.; Thomson, T.; Fullerton, E. E.; Murray, C. B.; Terris, B. D. *J. Am. Chem. Soc.* **2002**, *124*, 2884.

(15) Sun, S. H.; Fullerton, E. E.; Weller, D.; Murray, C. B. *IEEE Trans. Magn.* **2001**, *37*, 1239.

(16) Park, J. I.; Cheon, J. *J. Am. Chem. Soc.* **2001**, *123*, 5743.

(17) Kiely, C. J.; Fink, J.; Zheng, J. G.; Brust, M.; Bethell, D.; Schiffrin, D. J. *Adv. Mater.* **2000**, *12*, 640.

(18) Chaubey, G. S.; Barcena, C.; Poudyal, N.; Rong, C. B.; Gao, J. M.; Sun, S. H.; Liu, J. P. *J. Am. Chem. Soc.* **2007**, *129*, 7214.

(19) Robinson, I.; Zacchini, S.; Tung, L. D.; Maenosono, S.; Thanh, N. T. K. *Chem. Mater.* **2009**, *21*, 3021.

(20) Datta, A.; Pal, M.; Chakravorty, D.; Das, D.; Chintalapudi, S. N. *J. Magn. Magn. Mater.* **1999**, *205*, 301.

(21) Bac, L.H.; Kwon, Y.S.; Kim, J.S.; Lee, Y.I.; Lee, D.W.; Kim, J.C. *Mater. Res. Bull.* **2010**, *45*, 352.

(22) Wang, H. Z.; Li, J.G.; Kou, X. L.; Zhang, L. *J. Cryst. Growth* **2008**, *310*, 3072.

(23) Lu, X. G.; Liang, G. Y.; Zhang Y. M. *Mater. Sci. Eng., B* **2007**, *139*, 124.

(24) Liao, Q. L.; Tannenbaum, R.; Wang Z. L. *J. Phys. Chem. B*, **2006**, 110, 14262.

(25) Tsuji, M.; Hashimoto, M.; Nishizawa, Y.; Kubokawa, M.; Tsuji, T. *Chem. Eur. J.* **2005**, *11*, 440.

(26) Makhluf, S.; Dror, R.; Nitzan, Y.; Abramovich, Y.; Jelinek, R.; Gedanken, A. *Adv. Funct. Mater.* **2005**, *15*, 1708.

(27) Panda, A. B.; Glaspell, G.; El-Shall, M. S. *J. Am. Soc. Chem.* **2006**, *128*, 2790.

(28) Hu, X. L.; Yu, J. C.; Gong, J. M.; Li, Q.; Li, G. S. *Adv. Mater.* **2007**, *19*, 2324.

(29) Yu, J. C.; Hu, X. L.; Li, Q.; Zhang, L. Z. *Chem. Commun.* **2005**, 2704.

(30) Hu, X. L.; Yu, J. C. *Chem. Mater.* **2008**, *20,* 6743.

(31) Hu, X. L.; Yu, J. C. *Chem.-Asian J.* **2006**, *1*, 605.

(32) Westerfield, M.; *The Zebrafish Book.* Edition 5, University of Oregon Press, Eugene. **2007**; pp 2.1.

(33) International Organization for Standardization; ISO 7346-2 Water quality-determination of the actual lethal toxicity of substances to a freshwater fish [*Brachydanio rerio* Hamilton-Buchanan (Teleostei, Cyprinidae)] Part 2: Semi-static method. 1996.

(34) Murphy, C. J.; Jana, N. R. *Adv. Mater.* **2002**, *14*, 80.

(35) Huelser, T. P.; Wiggers, H.; Ifeacho, P.; Dmitrieva, O.; Dumpich, G. Lorke, A. *Nanotechnology* **2006**, *17,* 3111.

(36) Oberdorster, G.; Oberdorster, E.; Oberdorster, J. *Environ. Health Perspect.* **2005**, *113,* 823.

(37) Grainger, D. W.; Castner, D. G. *Adv. Mater.* **2008**, *20*, 867.

(38) Bar-Ilan, O.; Albrecht, R. M.; Fako, V. E.; Furgeson, D. Y. *Small* **2009**, *5*, 1897.

(39) Wang, Y. X.; Hussain, S. M.; Krestin, G. P. *Eur. Radiol.* **2001**, *11*, 2319.

(40) Corot, C.; Robert, P.; Idée, J. M.; Port, M. *Adv. Drug Delivery Rev.* **2006,** *58*,

1471.

Chapter Three

Mesoporous Magnetite Nanoclusters as Magnetic Resonance Probes

3.1 Introduction

In the past few decades, magnetic nanomaterials have attracted much attention owing to their unique magnetic features and important biomedical applications, such as bioseparation, drug delivery, and detection of cancer.[1-4] In particular, the magnetite (Fe_3O_4) nanoparticles are commonly used in cellular and molecular imaging as magnetic resonance imaging (MRI) contrast agents because of their good biocompatibility, low cost and localized shortening of spin-spin (T_2) proton relaxation times.[5-8] The effectiveness of a contrast agent is determined by its relaxivity, or how much the relaxation rates of water protons are increased in the presence of the agent at a given concentration.[9-11] The traditional MRI probes of superparamagnetic iron oxide (SPIO) nanoparticles with dimensions on the order of less than 10 nm and a low magnetization per particle, are usually difficult to be manipulated or controlled in

blood by using moderate magnetic fields,[12] this limits their usage in targeted delivery. Efforts to increase the relaxivity of magnetic nanoparticle contrast agents have been focused on the development of new magnetic core materials,[13] increase of the nanoparticle size,[14] or aggregation of SPIO nanoparticles by encapsulation of polymer or organic acid.[15-18] Increasing nanoparticle size can increase the relaxivity, but also induces superparamagnetic-ferromagnetic transition (at a domain size of ca. 30 nm for Fe_3O_4),[19] making nanoparticles no longer dispersible in solution. There is still a demand for nanoparticles with high T_2 relaxivity and sensitivity, which can enhance the efficiency of targeted diagnostic imaging.

Magnetite nanoculsters, composed of many ultrafine magnetite nanocrystals, have the advantage of increasing the magnetization in a controllable manner while retaining the superparamagnetic characteristics.[12] Several methods are developed for direct synthesis of magnetic nanoparticle clusters. These include high-temperature reduction with poly(acrylic acid) (PAA) or trisodium acetate as stabilizers, modified coprecipitation methods, or decomposition of iron salts in polyol.[12,20,21] These methods are either time-consuming, or they require additional stabilizer or template.

Herein, we report the development of superparamagnetic mesoporous magnetite nanoculsters as MRI probes with very high T_2 relaxivity and sensitivity. Mesoporous materials provide an ideal platform for the development of MR-enhancing materials due to their high surface areas and tunable pore structures.[22] Up to now, there is no report of using mesoporous magnetite nanoculsters as *in vivo* MRI probes. The mesoporous magnetite nanoclusters are prepared by using a rapid and economical

route based on an efficient microwave-assisted process. Microwave irradiation is becoming an increasingly popular heating method for nanomaterials synthesis.[23-25] We have synthesized colloidal Fe_2O_3 nanocrystals,[26] ZnO nanoclusters,[27] Ni nanowires[28] and $FeNi_3$ nanochains[29] by taking advantage of microwave irradiation and hydrothermal effects. In this work, the magnetite nanoclusters were synthesized within 5 min without using any hard templates or catalysts. The structure, morphology and composition of the magnetite nanoclusters were investigated. The diameter could be controlled effectively by changing the amounts of precursors. *In vitro* and *in vivo* studies confirmed the effectiveness of these magnetite nanoclusters for MRI contrast enhancement. *In vivo* toxicity was studied by exposing zebrafish larvae to the nanoclusters. The newly designed nanoclusters have the potentials to enhance the efficiency of targeted imaging and a wide spectrum of biomedical applications.

3.2 Experimental Section

3.2.1 Preparation of mesoporous magnetite nanoclusters

All chemicals were of analytical grade and were used as received without further purification. All the samples were prepared in a microwave digestion system (Ethos TC Plus 1, Milestone). In a typical procedure, 1 mmol iron(III) acetylacetonate ($Fe(acac)_3$) was dissolved into 45mL ethylene glycol, and then 1mL of hydrazine

monohydrate was added dropwise by an auto-pipette over an one-minute period. After stirring mildly for several minutes, the solution was sealed in a high-pressure digestion vessel which was Teflon-lined and double-walled. The reaction vessel was fitted with a temperature probe that was housed in a sturdy thermowell and protected from chemical attack by a triple layer of PTFE/ceramic/PTFE. The desired exposure time and temperature were programmed by using Milestone's EasyControl software. The Automatic Temperature Control system allowed continuous monitoring and controlling (±1 ℃) of the internal temperature. The preset profile (desired time and temperature) was followed automatically by continuously adjusting the applied power (0-1000 W) in order to keep the reaction temperature at 220℃. After treating the mixture at 220 ℃ for 5 min under microwave irradiation, the vessel was cooled to room temperature. The product was collected, washed with deionized water and absolute ethanol, and dried in a vacuum at 60 ℃ for 4 hours. Finally, as-prepared powder was obtained for further characterization and application.

3.2.2 Characterization of mesoporous magnetite nanoclusters

The samples were examined by powder XRD with a Bruker D8 Advance diffractometer using Cu Kα irradiation (λ = 1.5406 Å). Diffraction patterns were collected from 20° to 80° with a step size of 0.02°. TEM images were recorded on a CM-120 microscope (Philips, 120 kV) coupled with an EDX spectrometer (Oxford

Instrument). High-resolution transmission electron microscopy (HRTEM, Tecnai 20, 200kV) was also used. Samples were deposited on thin amorphous carbon films supported by copper grids from ultrasonically processed ethanol solutions of the samples. The general morphology of the products was characterized by field emission scanning electron microscopy (FESEM, Quanta 400 FEG). The N_2-sorption isotherms were recorded at 77 K in a Micromeritics ASAP 2010 instrument. All samples were degassed at 150 ℃ and 10^{-6} Torr for 24 h prior to measurements. The Brunauer-Emmett-Teller (BET) approach was used to determine the surface area. X-ray photoelectron spectroscopy (XPS) measurement was performed with a PHI Quantum 2000 XPS system with a monochromatic Al K_α source and a charge neutralizer. All binding energies were referenced to the C_{1s} peak at 284.8 eV of the surface adventitious carbon. Powdered products were weighed out for magnetic characterization by vibrating sample magnetometry (VSM-7300, Lakeshore, U.S.A.).

3.2.3 Toxicity test-Exposure of the zebrafish larvae to magnetite nanoclusters

For toxicity studies, 20 healthy larvae (5 day post-fertilization and hatched) were transferred to a 100 ml polyethylene beaker containing 50 ml of a solution prepared by dissolving 60 mg of artificial sea salt in one liter of ultrapure (deionized and purified after reverse osmosis) water. All fish rearing conditions and larval production procedures were carried out according to Westerfield[30] and the bioassay was

performed according to the Organisation for Economic Co-operation and Development[31] recommended method. Different concentrations of 100 nm nanoclusters (0, 1, 5, 10, 25, 25, 50 mg/L) were sonicated and added to the beakers and incubated for 96 h at 28.5°C. Tests were performed six times (120 larvae per concentration). The survival rate is expressed as the total number of survival larvae after 24, 72 and 96 h.

3.2.4 *In vitro* MRI of magnetite nanoclusters

MR relaxometry of the magnetite nanoclusters was performed using a clinical 1.5 T whole-body MR system (Siemens Sonata, Erlangen, Germany) in combination with a human knee radio frequency coil for excitation and signal reception. Magnetite nanoclusters were dispersed in distilled water at iron concentrations ranging from 0.001 to 0.02 mmol/L. For MR measurements, magnetite nanoclusters dispersed solutions (1 mL) were filled in each 1.5 mL Eppendorf tubes. Sonication was applied for 10 min prior to MRI using at 40 kHz (Branson 3510E-MTH) in water at ambient temperature. T_2 relaxation times were measured using a standard Carr-Purcell-Meiboom-Gill pulse sequence (TR = 2000 msec, TE range = 30-960 msec, 32 echoes, FOV = 134 × 67 mm, matrix = 128 × 64, slice thickness = 5 mm, NEX = 3). T_2 relaxation times were calculated by a linear fit of the logarithmic ROI signal amplitudes versus TE. The T_2 relaxivity (r_2) was determined by a linear fit of the inverse relaxation times as a function of the iron concentrations used.

3.2.5 *In vivo* MRI of magnetite nanoclusters

The experimental protocol was approved by the local Animal Experiment Ethics Committee. Four Male Sprague Dawley (SD) rats (approx 350 g) from the same batch were used. Under brief anesthesia, an aqueous dispersion of the magnetite nanoclusters (Fe concentration of 0.6 mg mL^{-1}) was injected via the tail vein into three rats at a dose equivalent to 2 mg Fe kg^{-1} of body weight. One rat injected with the equivalent volume of saline was used as control. MRI of the abdomen four rats was performed 12 hours later. A 3.0 Tesla clinical whole-body imaging system was used (Achieva, Philips Healthcare, Best, The Netherlands), a custom made volume RF coil suitable for rat body was employed as the signal transmitter and receiver. The imaging parameters included gradient echo sequence, TR/TE=202/9 millisecond, Flip angle=45^0, in-plane resolution=0.27 mm ×0.27 mm, slice thickness=3mm, NEX=6.

3.2.6 Prussian blue staining

After the MR imaging and approximately 14 hours post injection of magnetite nanoclusters, the rats were euthanized with an over dose of pentobarbital. The liver, spleen, and kidneys were perfused via the heart with 4% paraformaldehyde for fixation, embedded in paraffin, and sectioned into 5-10-μm-thick slices for

hematoxylin-eosin staining to display tissue morphology and for Prussian blue staining to identify iron particles.[32] The principle of Prussian blue staining is that the ferric iron (Fe^{3+}) in the presence of ferrocyanide ion is precipitated as the highly colored and highly water-insoluble complex, potassium ferric ferrocyanide. The iron particles in the organ pieces were observed as blue dots using an optical microscope.

3.3 Results and discussion

3.3.1 Characterization of magnetite nanoclusters

The X-ray diffraction (XRD) pattern in Fig. 3.1 shows all reflections can be indexed to magnetite (JCPDS no. 19-0629), which is in good agreement with the literature values.[12] The broad diffraction peaks further suggest the ultrafine nanocrystalline nature of the magnetite particles.

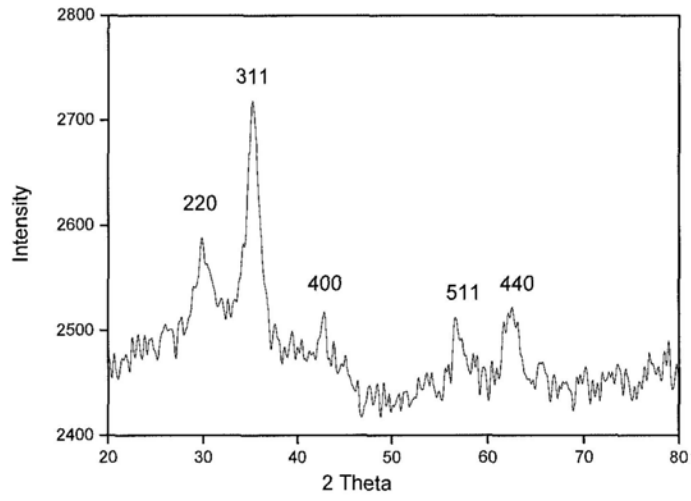

Figure 3.1 XRD patterns of the as-prepared magnetite nanoclusters.

A general overview FESEM image in Fig. 3.2a shows that the product is composed of uniform spherical magnetite nanoparticles. The diameter of the spheres is about 100 nm. A TEM image (Fig. 3.2b) of the magnetite particles shows a nearly uniform size of about 100 nm. A close inspection of Fig. 3.2c suggests that the obtained magnetite particles are loose clusters, and a high-resolution TEM (HRTEM) image (Fig. 3.2d) further reveals that the particles are composed of nanocrystals with an average size of 3-5 nm. The selected-area electron diffraction (SAED) pattern (the inset of Fig. 3.2b) reveals a polycrystalline-like diffraction, suggesting that the sample consists of many magnetite nanocrystals.

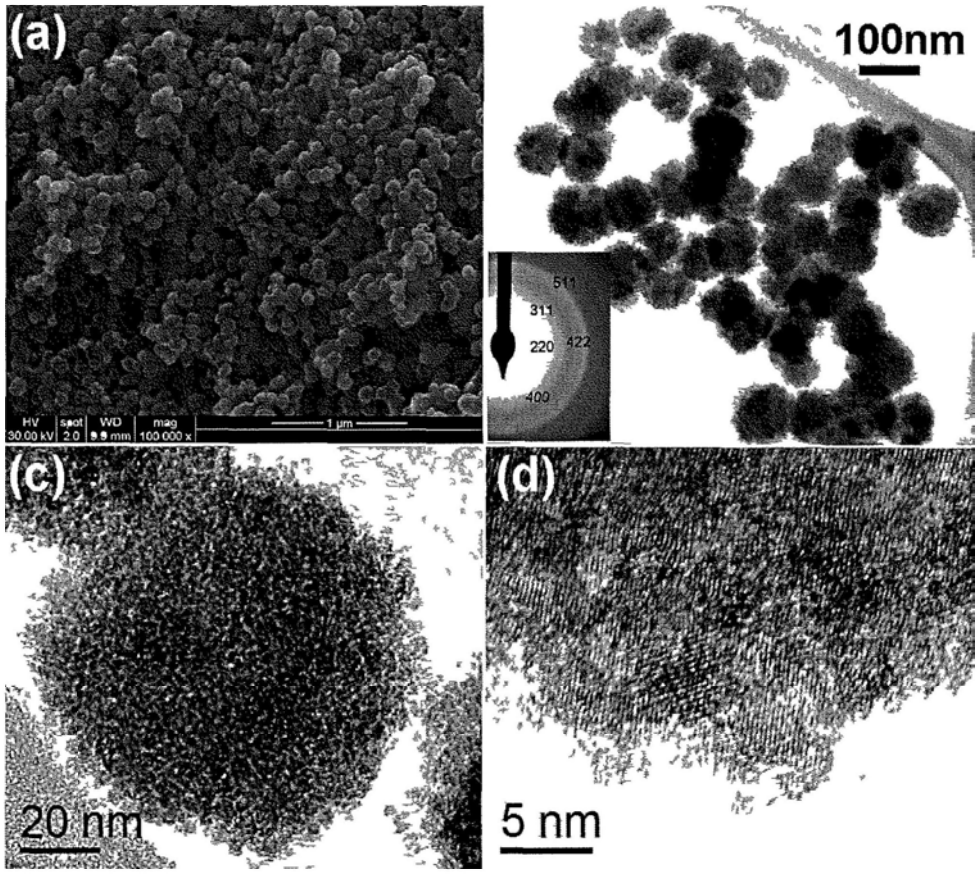

Figure 3.2 (a) FESEM image, (b) TEM image and (c, d) HRTEM image of the as-prepared magnetite nanoclusters. The inset in (b) is the SEAD pattern corresponding to the small frame area marked at one single nanocluster.

In a typical microwave-hydrothermal process, the diameters of the nanospheres were influenced by the concentration of starting material. TEM images in Fig. 3.3 show that when the $Fe(acac)_3$ amount is in the range of 0 2 to 2 mmol while keeping all other parameters constant, the diameter of the nanoclusters increases from 75 to 115 nm, indicating that higher $Fe(acac)_3$ concentrations can lead to a larger particle size.

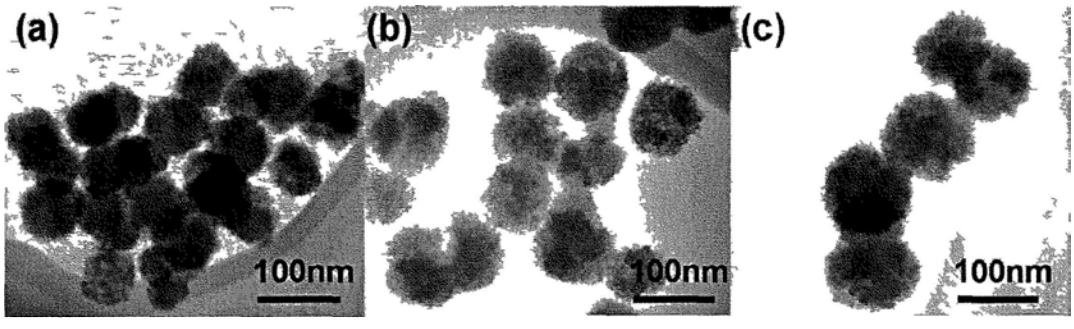

Figure 3.3 TEM images of the magnetite nanoclusters prepared with different initial $Fe(acac)_3$ concentrations: (a) 0.2, (b) 0.5, (c) 2 mmol.

X-ray photoelectron spectroscopy (XPS) was used to determine the surface composition of the nanoclusters. XPS results (Fig. 3.4) show peaks at 710.5 and 724.3 eV, which are in good agreement with the known values of the $Fe2p_{3/2}$ and $Fe2p_{1/2}$ oxidation states.[21] The results further confirm that the magnetite particles were synthesized by the effective microwave-assisted approach.

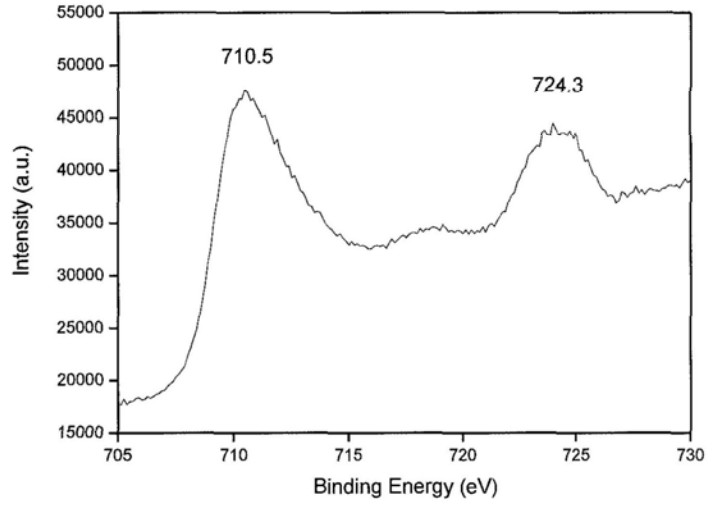

Figure 3.4. The XPS spectrum of the as-prepared 100 nm magnetite nanoclusters.

Figure 3.5 shows the nitrogen adsorption/desorption isotherms of magnetite nanoclusters. The isotherm was of type IV classification, showing typical hysteresis loops of mesoporous materials and further confirming the nanocluster structure. The magnetite nanoclusters had a surface area of 72.3 m^2 g^{-1}. It can be clearly seen that two peaks appear on the pore size distribution curve. One peak was located at around 2.7 nm, corresponding to filling of the pores formed in the nanoclusters. The other peak was centered at 16.7 nm, corresponding to filling of the pores formed among the nanoclusters. The single point adsorption total volume at $P/P_0 = 0.973$ of magnetite is 0.099 cm^3/g.

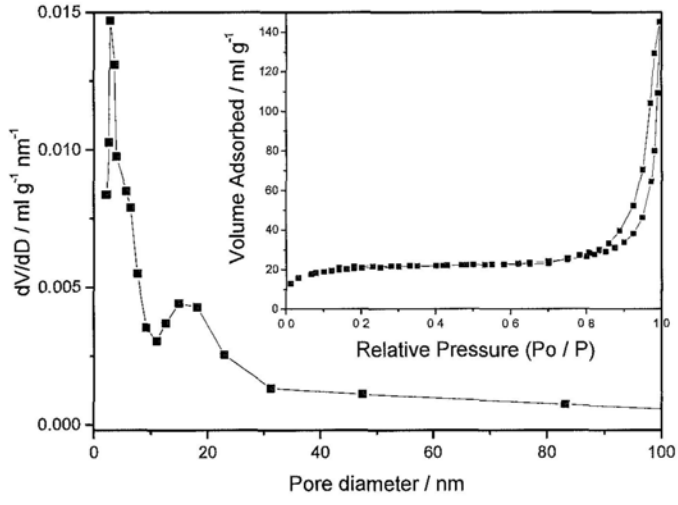

Figure 3.5 The pore size distribution curve and corresponding N_2-sorption isotherm (inset) for 100 nm magnetite nanoclusters.

The magnetic properties (Fig. 3.6a) of the magnetite particles synthesized indicate that the particles have no remanence or coercivity at 300 K, and their magnetization saturation value (Ms) increases to 38.3emu/g The inserted Fig. 3.6 (b, c) show a fast response to a foreign magnet and the magnetite nanoclusters can be separated from the solution.

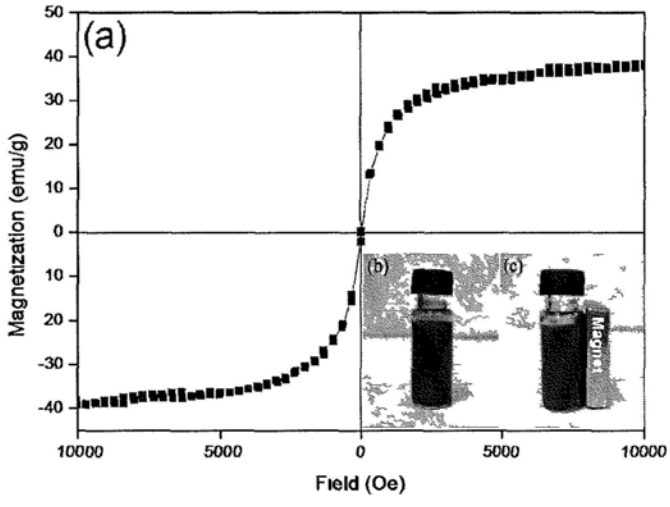

Figure 3.6 (a) The hysteresis loops of 100nm magnetite nanoclusters at 300 K. The inserts in (b-c) Photograph of the 100 nm magnetite nanoclusters dispersed in the water and response to external magnetic field.

3.3.2 Toxicity test of magnetite nanoclusters by using zebrafish larvae

While rapid development of nanomaterials will certainly continue, the application of these materials will be limited by their inherent toxicity.[33,34] Thus, the need for evaluating nanotoxicity is becoming increasingly paramount. Transparent zebrafish, possessing a high degree of homology to the human genome, offers an economically feasible platform for noninvasive real-time assessments of nanotoxicity.[35] The toxicity of the as-prepared magnetite nanoclusters were evaluated using zebrafish as a model. The survival rates were calculated after 24, 72 and 96 h. Figure 3.7 shows in detail the survival rates of zebrafish larvae at different concentrations of nanoclusters (0, 1, 5, 10, 25, 25, 50 mg/L) after 96h exposure. The results show that nearly 100% zebrafish larvae survived even under the highest concentration 50 mg/L.

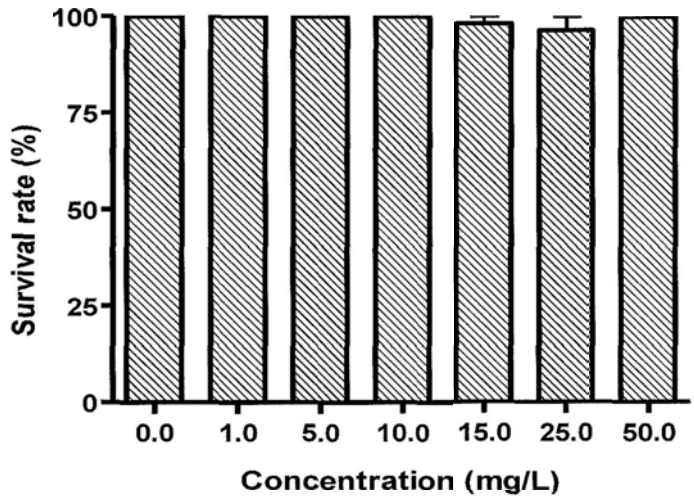

Figure 3.7 The survival rate of zebrafish larvae at different magnetite nanocluster (100 nm) concentrations after 96h exposure.

3.3.3 *In vitro and in vivo* MRI of magnetite nanoclusters

3.3.3.1 *In vitro* MRI

Fig. 3.8 shows *in vitro* MRI of magnetite nanoclusters suspended in DI water at the different concentrations of nanoclusters (0, 0.001, 0.002, 0.005, 0.01, 0.02 mM). The magnetite nanoclusters resulted in signal decrease in a concentration dependant manner, with higher concentration leading to darker signal, and the detection limit is around 0.001mM. The *in vitro* relaxivity plot of magnetite nanoclusters is presented in

Fig. 3.9 and the T_2 relaxivity was 406 s^{-1} mM^{-1}. T_2 relaxivity of magnetite nanoclusters from the study was approximately 10 times higher than single nanoparticle micellar SPIO (30-50 s^{-1} mM^{-1}),[36] and 3.4 times higher than the commercial Feridex. Na et al.[38] summarized the recent progress in inorganic nanoparticle-based MRI contrast agents, they concluded that the $MnFe_2O_4$ nanoparticles (MnMEIO) had much larger relaxivity (358 s^{-1} mM^{-1}) than other nanoparticles. The current results demonstrated that magnetite nanoclusters from this study achieved a higher MRI contrast effect as the commercial iron oxides[39] and other reported data.[36-38]

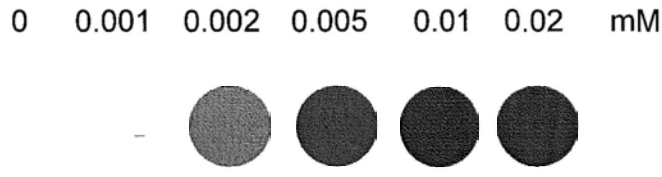

Figure 3.8 T_2- weighted MR image of 100 nm magnetite nanoclusters in DI water.

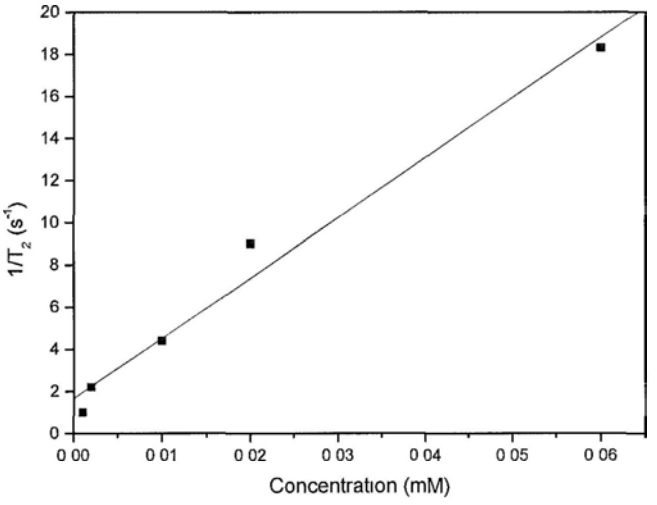

Figure 3.9 T_2 relaxivity measurement of 100 nm magnetite nanoclusters.

Magnetite nanoparticles, with a diameter of about 100-150nm were found to cause better cell labeling efficiencies and MR signal alterations as compared to smaller ultra small paramagnetic iron oxides (USPIOs), which have average hydrodynamic diameters of 20-40nm.[37,40] This is probably due to the fact that phagocytic and endocytic uptake increases with increasing particle diameter. Meanwhile, large magnetite nanoparticles have a large magnetization and a high r_2 relaxivity, which renders it possible to increase the sensitivity in T_2-weighted images and to ease the toxicity concern by decreasing the agent dosage.[41] In addition, mesoporous structure benefits the MRI sensitivity due to the high surface area and tunable pore structures.[22] High surface area may be beneficial when the SPIO is used

as targeted drug carrier. The enhanced T_2 relaxation of nanoclusters measured here is significant when combined with the highly controllable aggregation process. The result is in agreement with previous studies of aggregated SPIO.[42-45] Specifically, nanoclusters possess higher relaxivity than monodispersed SPIO nanopartilces due to the increased proton spin dephasing from the cooperating SPIO cores in the aggregates. This cooperative T_2 relaxation rate enhancement of aggregated SPIO cores is explained by a theoretical model by Roch et al which adapts the conventional SPIO model by accounting for the greater magnetic moment and longer correlation time caused by aggregation.[45]

3.3.3.2 *In vivo* MRI

MRI of rat abdomen post intravenous magnetite nanoclusters administration shows significant signal void of the liver and spleen, but not other solid organs such as bilateral kidneys. Fig. 3.10 shows *in vivo* MRI of Sprague Dawley (SD) rat liver. Lower image was acquired 12 hours after intravenous injection of the magnetite nanoclusters at 0.6 mg mL^{-1} Fe concentration, equivalent to a dose of 2 mg Fe kg^{-1} of the body weight. A rat injected with the equivalent volume of saline was used as control (control, upper image). It can be seen the control rat's liver showed normal intermediate gray signal, while magnetite nanoclusters administration lead to signal void of the liver parenchyma.

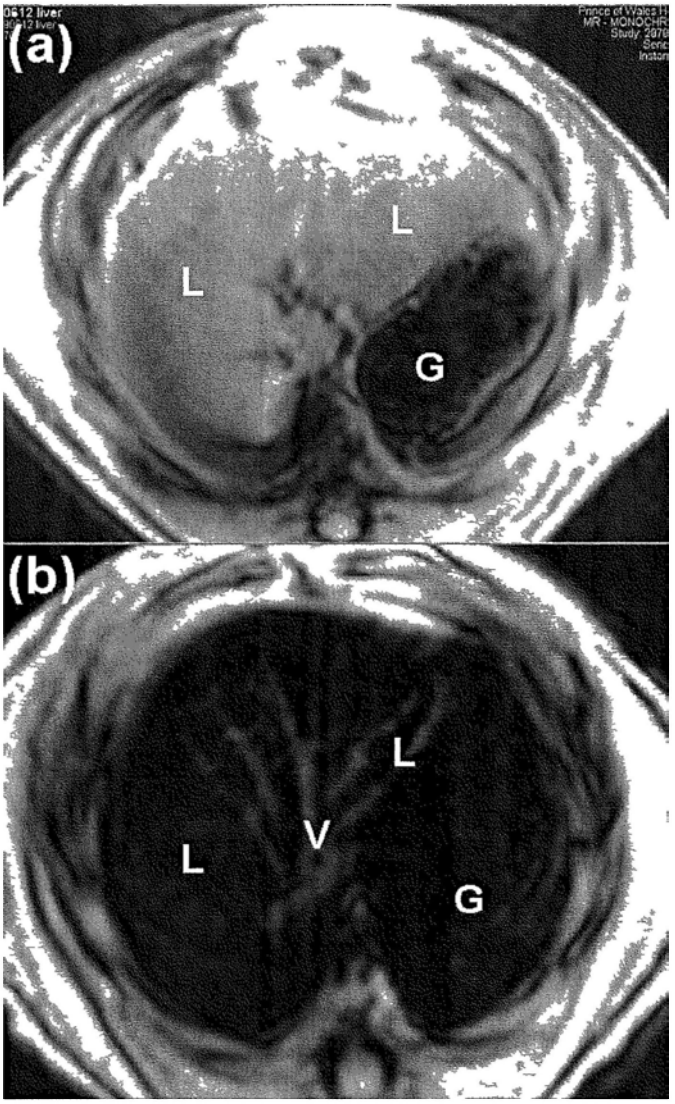

Figure 3.10 MRI of the control rat liver (a) and 100 nm magnetite nanoclusters enhanced rat liver (b). Control rat liver parenchyma (L) shows gray signal The gas in the stomach (G) is shown dark signal Magnetite nanoclusters enhanced rat liver (L) shows parenchyma signal void. The vessels (V) in liver b, which do not contain magnetite nanoclusters, shows tree branch like structure of higher signal.

Histological analysis of the liver and spleen is shown in Fig. 3.11. The uptake of magnetite nanoclusters was investigated using Prussian blue staining. As expected, there are large number of macrophages up-taken magnetite nanoclusters and then deposited in the spleen (Fig. 3.11c, d). Magnetite nanoclusters containing macrophages are also seen in the liver, which contains less macrophages than the spleen. It is interesting to note while there is only small amount of magnetite nanoclusters containing macrophage in the liver (Fig. 3.11a, b), these magnetite nanoclusters lead to signal void of the liver parenchyma so that it is close to background signal. There is no blue staining granules in the kidneys.

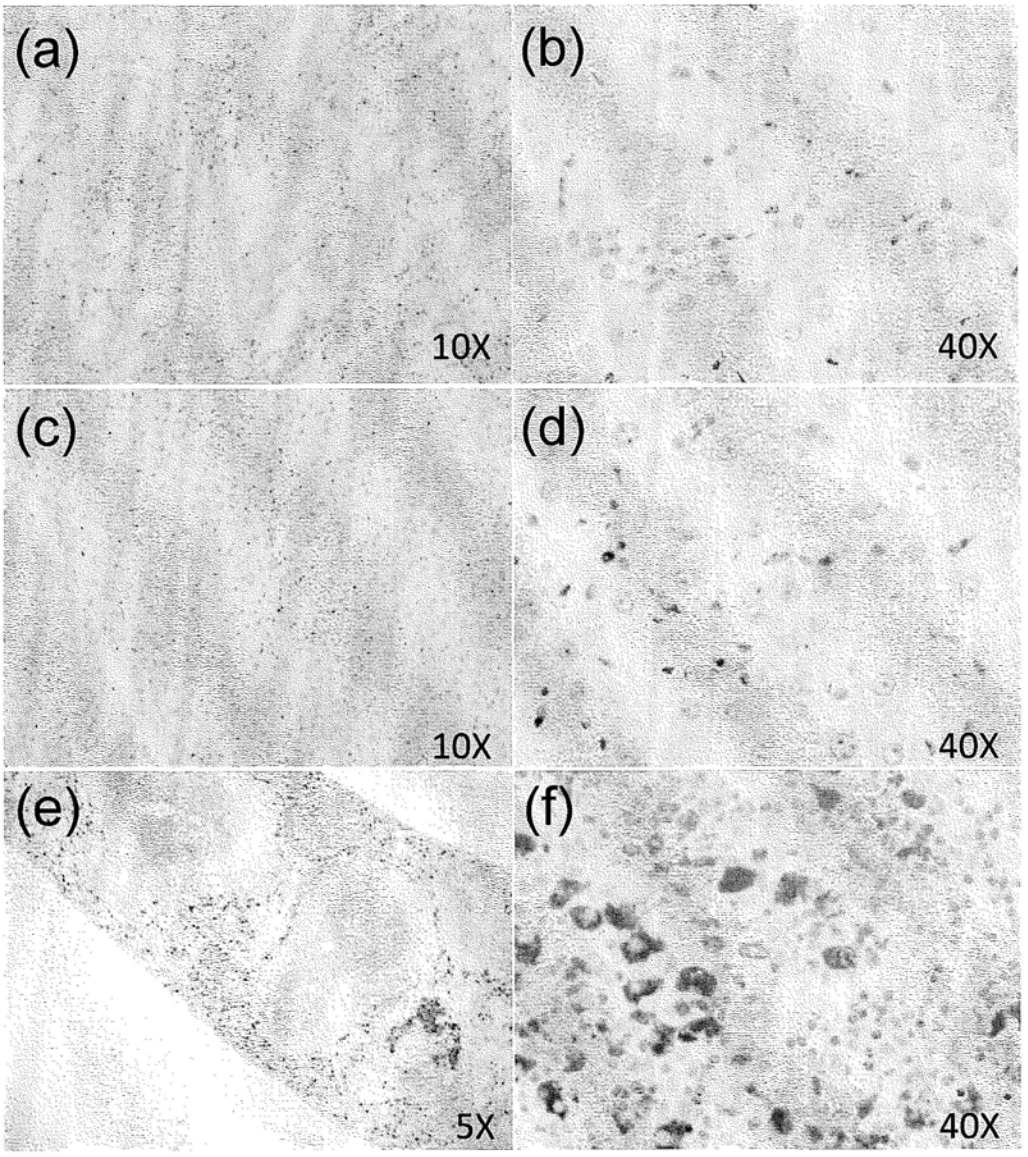

Figure 3.11 Histological analysis with Prussian blue staining of the rat kidney (a, b), liver (c, d) and spleen (e, f) 14 hours post intravenous injection of magnetite nanoclusters. Magnetite nanocluster is dyed blue in the pictures. There is no magnetite nanocluster in the kidney, while there is small amount of magnetite nanoclusters in the liver, and significant amount in macrophages of the spleen.

3.4 Conclusions

This chapter reports a rapid and economical microwave-assisted synthesis of superparamagnetic mesoporous magnetite nanoclusters with diameters between 75nm and 115nm. The prepared magnetite nanoclusters show good *in vitro* and *in vivo* MRI contrast properties due to their high saturation magnetization and mesoporous structure. Toxicity test by exposing the zebrafish larvae to nanoclusters confirms that the magnetite nanoclusters are non-toxic. In experimental rats post intravenous administration, magnetite nanoclusters are shown to be present in the reticuloendothelial system organs of liver and spleen, but not in the kidneys.

3.5 References

(1) Jun, Y. W.; Seo, J. W.; Cheon, J. *Acc. Chem. Res.* **2008**, *41*,179.

(2) Lewin, M.; Carlesso, N.; Tung, C. H.; Tang, X. W.; Cory, D.; Scadden, D. T.; Weissleder, R. *Nat. Biotechnol.* **2000**, *18*, 410.

(3) Martin, A. L.; Bernas, L. M.; Rutt, B. K.; Foster, P. J.; Gillies, E. R. *Bioconjugate Chem.* **2008**, *19*, 2375.

(4) Wang, Y. X.; Hussain, S. M.; Krestin, G. P. *Eur. Radiol.* **2001**, *11*, 2319.

(5) Du, L.; Chen, J.; Qi, Y.; Li, D.; Yuan, C.; Lin, M. C.; Yew, D. T.; Kung, H. F. Yu, J. C.; Lai, L. *Int. J. Nanomedicine* **2007**, *2*, 805.

(6) Duguet, E.; Vasseur, S.; Mornet, S.; Devoisselle, J. M. *Nanomedicine* **2006**, *1*, 157.

(7) Khemtong, C.; Kessinger, C. W.; Ren, J.; Bey, E. A.; Yang, S. G.; Guthi, J. S.; Boothman, D. A.; Sherry, A. D.; Gao, J. *Cancer Res.* **2009**, *69*, 1651.

(8) Shi, Z.; Neoh, K. G.; Kang, E. T.; Shuter, B.; Wang, S. C.; Poh, C.; Wang, W. *ACS Appl. Mater. Interfaces* **2009**, *1*, 328.

(9) Caravan, P.; Ellison, J.; McMurry, T.; Lauffer, R. *Chem. Rev.* **1999**, *99*, 2293.

(10) Muller, R. N.; Gillis, P.; Moiny, M.; Roch, A. *Magn. Reson. Med.* **1991**, *222*, 178.

(11) Merbach, A. E.; Tóth, E. *The chemistry of contrast agents in medical magnetic*

resonance imaging, Wiley, Chichester, 2001.

(12) Ge, J. P.; Hu, Y. X.; Biasini, M.; Beyermann, W. P.; Yin, Y. D. *Angew. Chem. Int. Ed.* **2007**, *46*, 4342.

(13) Seo, W. S.; Lee, J. H.; Sun, X.; Suzuki, Y.; Mann, D.; Liu, Z.; Terashima, M.; Yang, P. C.; McConnell, M. V.; Nishimura, D. G.; Dai, H. *Nat. Mater.* **2006**, *5*, 971.

(14) Cheon, J.; Lee, J. H. *Acc. Chem. Res.* **2008**, *41*, 1630.

(15) Berret, J. F.; Schonbeck, N.; Gazeau, F.; El Kharrat, D.; Sandre, O.; Vacher, A.; Airiau, M. *J. Am. Chem. Soc.* **2006**, *128,* 1755.

(16) Larsen, B. A.; Haag, M. A.; Serkova, N. J.; Shroyer, K. R.; Stoldt, C. R. *Nanotechnology* **2008**, *19*, 265102.

(17) Moffat, B. A.; Reddy, G. R.; McConville, P.; Hall, D. E.; Chenevert, T. L.; Kopelman, R. R.; Philbert, M.; Weissleder, R.; Rehemtulla, A.; Ross, B. D. *Mol. Imag.* **2003**, *2*, 324.

(18) Talelli, M.; Rijcken, J. F. C.; Lammers, T.; Seevinck, P. R.; Storm, G.; Nostrum, C. F. V.; Hennink, W. E. *Langmuir* **2009**, *25*, 2060.

(19) Krishnan, K. M.; Pakhomov, A. B.; Bao, Y.; Blomqvist, P.; Chun, Y.; Gonzales, M.; Grffin, K.; Ji, X.; Roberts, B. K. *J. Mater. Sci.* **2006**, *41*, 793.

(20) Hu, F. Q.; MacRenaris, K. W.; Waters, E. A.; Schultz-Sikma, E. A.; Eckermann, A. L.; Meade, T. J. *Chem. Commun.* **2009**, *4,* 73.

(21) Liu, J.; Sun, Z. K.; Deng, Y. H.; Zou, Y.; Li, C. Y.; Guo, X. H.; Xiong, L. Q.; Gao, Y.; Li, F.Y.; Zhao, D. Y. *Angew. Chem. Int. Ed.* **2009**, *48*, 5875.

(22) Taylor, K. M. L.; Kim, J. S.; Rieter, W. J.; An, H. Y.; Lin, W. L.; Lin, W. B. *J. Am. Chem. Soc.* **2008**, *130*, 2154.

(23) Makhluf, S.; Dror, R.; Nitzan, Y.; Abramovich, Y.; Jelinek, R.; Gedanken, A. *Adv. Funct. Mater.* **2005**, *15*, 1708.

(24) Panda, A. B.; Glaspell, G.; El-Shall, M. S. *J. Am. Soc. Chem.* **2006**, *128*, 2790.

(25) Tsuji, M.; Hashimoto, M.; Nishizawa, Y.; Kubokawa, M.; Tsuji, T. *Chem. Eur. J.* **2005**, *11*, 440.

(26) Hu, X. L.; Yu, J. C.; Gong, J. M.; Li, Q.; Li, G. S. *Adv. Mater.* **2007**, *19*, 2324.

(27) Hu, X. L.; Gong, J. M.; Zhang, L. Z.; Yu, J. C. *Adv. Mater.* **2008**, *20*, 4845.

(28) Hu, X. L.; Yu, J. C. *Chem. Mater.* **2008**, *20*, 6743.

(29) Jia, J. C.; Yu, J. C.; Wang, Y. X.; Chan, K. M. *ACS Appl. Mater. Interfaces* **2010**, *2*, 2579.

(30) Westerfield, M. *The zebrafish book, 5th edn.* University of Oregon Press, Eugene, 2007, pp 2.1.

(31) OECD, ISO 7346-2 *Water quality-determination of the actual lethal toxicity of substances to a freshwater fish [Brachydanio rerio Hamilton-Buchanan (Teleostei, Cyprinidae)] Part 2: Semi-static method* **1996**

(32) Ju, S.; Teng, G. J.; Lu, H.; Zhang, Y.; Zhang, A.; Chen, F.; Ni, Y. *Radiology* **2007**,

245, 206.

(33) Grainger, D. W.; Castner, D. G. *Adv. Mater.* **2008**, *20*, 867.

(34) Oberdorster, G.; Oberdorster, E.; Oberdorster, J. *Environ. Health Perspect.* **2005**, *113*, 823.

(35) Bar-Ilan, O.; Albrecht, R. M.; Fako, V. E.; Furgeson, D. Y. *Small* **2009**, *5*, 1897.

(36) Ai, H.; Flask, C.; Weinberg, B.; Shuai, X. T.; Pagel, M. D.; Farrell, D.; Duerk, J.; Gao, J. M. *Adv. Mater.* **2005**, *17*, 1949.

(37) Corot, C.; Robert, P.; Idée J. M.; Port, M. *Adv. Drug Deliv. Rev.* **2006**, *58*, 1471.

(38) Na, H. B.; Song, I. C.; Hyeon, T. *Adv. Mater.* **2009**, *21*, 1.

(39) Wang, Y.; Ng, Y. W.; Chen, Y.; Shuter, B.; Yi, J. B.; Ding, J.; Wang, S. C.; Feng, S. S. *Adv. Funct. Mater.* **2008**, *18*, 308.

(40) Daldrup-Link, H. E.; Rudelius, M.; Oostendorp, R. A.; Jacobs, V. R.; Simon, G. H.; Gooding, C.; Rummeny, E. J. *Acad. Radiol.* **2005**, *12*, 502.

(41) Kim, E. H.; Lee, H. S.; Kwak, B. K.; Kim, B. K.; *J. Magn. Magn. Mater.* **2005**, *289*, 328.

(42) Tsourkas, A.; Hofstetter, O.; Hofstetter, H.; Weissleder, R.; Josephson, L. *Angew. Chem. Int. Ed.* **2004**, *43*, 2395.

(43) Perez, J. M.; Josephson, L.; O'Loughlin, T.; Hogemann, D.; Weissleder, R. *Nat. Biotechnol.* **2002**, *20*, 816.

(44) Josephson, L.; Perez, J. M.; Weissleder, R. *Angew. Chem. Int. Ed.* **2001**, *40*, 3204.

(45) Roch, A.; Gossuin, Y.; Muller, R. N.; Gillis, P. *J. Magn. Magn. Mater.* **2005**, *293*, 532.

Chapter Four

Bifunctional Mesoporous Core/Shell Ag@FeNi$_3$ Nanospheres for Magnetic Resonance and Fluorescent Imaging

4.1 Introduction

Core/shell nanostructures have recently been intensively studied because of their unique functionalities.[1] Various shells were reported, including carbon,[2,3] polymer,[4,5] and inorganic compounds such as SiO_2[6,7] and Fe_3O_4 [8]. In particular, transition metal alloys were extensively studied in the past several decades for their increasing utility in electronic and energy conversion devices.[9] Alloys form when two or more metals coaggregate to produce compositionally ordered structures, with properties that differ from those of bulk alloys or nanoparticles of the individual components.[10-13] This makes magnetic alloy nanoparticles particularly interesting because of their high saturation magnetization[14] and resistance against oxidation.[15] As important transition

alloys, iron-nickel alloys, such as $FeNi_3$, are of great interest due to their useful magnetic properties and can be used as a new class of magnetic resonance imaging (MRI) probes [16] as well as other applications.[17-21] MRI is currently one of the most powerful diagnosis tools in medical science. It has been the preferred tool for imaging the brain and the central nervous system, for assessing cardiac function, and for detecting tumors. MRI contrast agents, which can help to clarify images, allow better interpretation. [22]

Metal-enhanced fluorescence (MEF) is an established technology,[23-26] where the interactions of fluorophores with metallic nanoparticles results in fluorescence enhancement, increased photostability, decreased lifetime owing to increased rates of system radiative decay, reduced blinking in single molecule fluorescence spectroscopy,[24] and increased transfer distances for fluorescence resonance energy transfer.[25] Recently, several authors have reported on the magnetic iron or iron oxide nanoparticles coated with Au,[27] gadolinium,[28] and silica.[29-31] In contrast with gold nanoparticles, Ag nanoparticles have several advantages as follows: (i) Ag nanoparticles exhibit a surface plasmon band between 390 and 420 nm that is a spectral regime that is distinct from that of Au (510-560 nm)[32] and (ii) the extinction coefficient of the surface plasmon band for an Ag particle is approximately 4 times as large as that for an Au particle of the same size.[33] Meanwhile, MEF requires that the fluorescent nanoparticles are monodisperse, bright, photostable, and amenable to further surface modification for the conjugation of biomolecules and/or fluorophores. Among the many types of fluorescent nanoparticles available today, nanoparticles

with core-shell architecture fulfill all these requirements, combining diverse functionalities into a single hybrid nanocomposite.[34] Therefore, a major advance would be to propose a method for designing particles with the physical properties of an Ag nanoparticle composition but with the surface chemistry of $FeNi_3$ alloy.

In this chapter, we report a rapid and economical microwave-assisted approach to fabricate a new class of bifunctional core-shell (Ag core-$FeNi_3$ alloy shell) nanoparticles modified by a polymer polyvinylpyrrolidone (PVP) in ethylene glycol solution at one step. The core/shell Ag@$FeNi_3$ nanospheres were synthesized within one minute without using any hard templates or catalysts. It shows the versatility of the core-shell architecture, and demonstrates their applicability for two platform technologies, metal-enhanced fluorescence (MEF) and magnetic resonance imaging (MRI).

4.2 Experimental Section

4.2.1 Reagents.

Iron(III) chloride ($FeCl_3$, 95%), nickel(II) chloride ($NiCl_2$, 95%), silver nitrate ($AgNO_3$, 95%), ethylene glycol (EG, 99.8%), hexamine (98%), hydrazine monohydrate (98%) were supplied by Aldrich. Deionized water was used throughout. All chemicals were used as received without further purification.

4.2.2 Preparation of Ag@FeNi$_3$ nanospheres.

All the samples were prepared in a microwave digestion system (Ethos TC Plus 1, Milestone). The detailed conditions are listed in Table 5.1. In a typical procedure, 0.2 mmol iron(III) chloride and 0.6 mmol nickel(II) chloride were dissolved into 45mL ethylene glycol, and then 0.05g silver nitrate and 0.5g PVP were added. After stirring mildly for about 5 min, 1mL of hydrazine monohydrate was added dropwise by an auto-pipette over an one-minute period, then the solution was sealed in a high-pressure digestion vessel which was Teflon-lined and double-walled. The reaction vessel was fitted with a temperature probe that was housed in a sturdy thermowell and protected from chemical attack by a triple layer of PTFE/ceramic/PTFE. The desired exposure time and temperature were programmed by using Milestone's EasyControl software. The Automatic Temperature Control system allowed continuous monitoring and controlling (±1℃) of the internal temperature. The preset profile (desired time and temperature) was followed automatically by continuously adjusting the applied power (0-1000 W) in order to keep the reaction temperature at 220℃. After treating the mixture at 220℃ for 1 min under microwave irradiation, the vessel was cooled to room temperature. The product was collected, washed with deionized water and absolute ethanol, and dried in a vacuum at 60℃ for 4 hours.

4.2.3 Characterization of Ag@FeNi$_3$ nanospheres.

The general morphology of the products was characterized by a field-emission

scanning electron microscope (FESEM, FEI, Quanta 400 FEG). Transmission electron microscopy (TEM, FEI/PHILIPS CM120), high-resolution TEM (HRTEM), and high angle annular dark field scanning TEM (HAADF-STEM) measurements were carried out on a Tecnai F20 microscope (FEI, 200 kV) coupled with an HAADF detector and an energy-dispersive X-ray (EDX) spectrometer. Two-dimensional STEM-EDX elemental mapping was performed for the product. The electron probe size for the STEM-EDX analysis was about 1 nm. X-ray diffraction (XRD) patterns were collected using a Bruker D8 Advance diffractometer using Cu K irradiation (λ =1.5406 Å). The Fourier transform infrared (FTIR) spectra were recorded using a Nicolet Magna 560 FTIR spectrometer. The N_2-sorption isotherms were recorded at 77 K in a Micromeritics ASAP 2010 instrument. All samples were degassed at 150 ℃ and 10^{-6} Torr for 24 h prior to measurements. The Brunauer- Emmett-Teller (BET) approach was used to determine the surface area. Powdered products were weighed out for magnetic characterization by vibrating sample magnetometry (VSM-7300, Lakeshore, U.S.A.)

4.2.4 Toxicity test of Ag@FeNi$_3$ nanospheres using embryos/larvae of zebra fish.

For toxicity studies, 20 healthy zebrafish larvae (5 day post-fertilization and hatched) were transferred to a 100 ml polyethylene beaker containing 50 ml of a solution prepared by dissolving 60 mg of artificial sea salt in one liter of ultrapure (deionized and purified after reverse osmosis) water. All fish rearing conditions and larval production procedures were carried out according to Westerfield[35] and the bioassay was performed according to the OECD recommended method.[36] Graded concentrations of Ag@FeNi$_3$ nanospheres (0, 0.5, 1, 5, 10, 25, 50 mg/L) were

sonicated and incubated for 96 h at 28.5°C. Tests were performed six times (120 larvae per concentration). The survival rate is expressed as the total number of survival larvae after 24, 48 and 96 h.

The silver nanoparticles (shown in Fig. 4.8) and $FeNi_3$ nanoparticles (prepared in chapter 1) were used by comparison. The silver nanoparticles were prepared using the microwave method in aqueous solution. In a typical procedure, 0.1mmol hexamine was dissolved completely in 44mL of water, and then 0.5mL 0.1M $AgNO_3$ solution was added, the solution was stirred for 5min and was sealed in a double-walled digestion vessel which was Teflon-lined and double-walled. After treating the mixture at 220℃ for 10 min under microwave irradiation, the vessel was cooled to room temperature. The product was collected, washed with deionized water and absolute ethanol, and dried in a vacuum at 60℃ for 4 hours.

4.2.5 *In vitro* MRI of Ag@FeNi$_3$ nanospheres.

MR relaxometry of the Ag@$FeNi_3$ nanospheres was performed using a clinical 1.5 T whole-body MR system (Siemens Sonata, Erlangen, Germany) in combination with a knee radio frequency coil for excitation and signal reception. Ag@$FeNi_3$ nanospheres were dispersed in distilled water at iron concentrations ranging from 0 to 0.3 mmol/L. For MR measurements, Ag@$FeNi_3$ nanospheres dispersed solutions (1 mL) were filled in each 1.5 mL Eppendorf tubes. Sonication was applied for 10 min prior to MRI using at 40 kHz (Branson 3510E-MTH) in water at ambient temperature.

4.2.6 Metal-enhanced fluorescence (MEF) of organic dyes using Ag@FeNi$_3$ nanospheres.

Our approach is through dyeing (doping) of the Ag@FeNi$_3$ nanospheres. In this regard, 500 μL ethanol solution of 0.2 mg/ml Rhodamine B (RhB) was added into 500 μL (0.2 mg) of Ag@FeNi$_3$ nanospheres suspended solution and incubated overnight. The mixture was centrifuged and washed with 1.5 mL H_2O and 1.2 mL ethanol 4 times, respectively. The absorbance and the fluorescence spectra of the washing solution were monitored to ensure the complete removal of the unadsorbed fluorophores.

UV-vis absorption spectra of the all samples were taken on a Cary 1E UV-visible Spectrophotometer. The fluorescence intensity was measured on a Hitachi F-4500 Fluorescence Spectrophotometer. The confocal microscope images of the microgel-stabilized emulsions were taken on a Nikon Eclipse Ti inverted microscope (Nikon, Japan). Lasers with wavelengths of 408 nm were used to excite the fluorescent nanoparticles.

4.3 Results and discussion

4.3.1 Characterization of Ag@FeNi$_3$ nanospheres.

Puce powders were obtained from the microwave-assisted reaction. Fig. 4.1

shows the X-ray diffraction (XRD) pattern of a typical product. All peaks can be indexed to the awaruite $FeNi_3$ alloy and cubic (face-centered cubic, fcc) Ag, which are in good agreement with the reported data (Joint Committee on Powder Diffraction Standards, JCPDS card no.: JCPDS card no.:38-0419 and JCPDS card no.: 4-783). No iron and nickel oxides or hydroxides or other impurity phases are detected. The sharp peaks and the low background reveal that the as-synthesized iron-nickel alloy particles had a high degree of crystallinity. This indicates that well-crystallized Ag@$FeNi_3$ nanospheres can be easily obtained under the proposed preparation conditions.

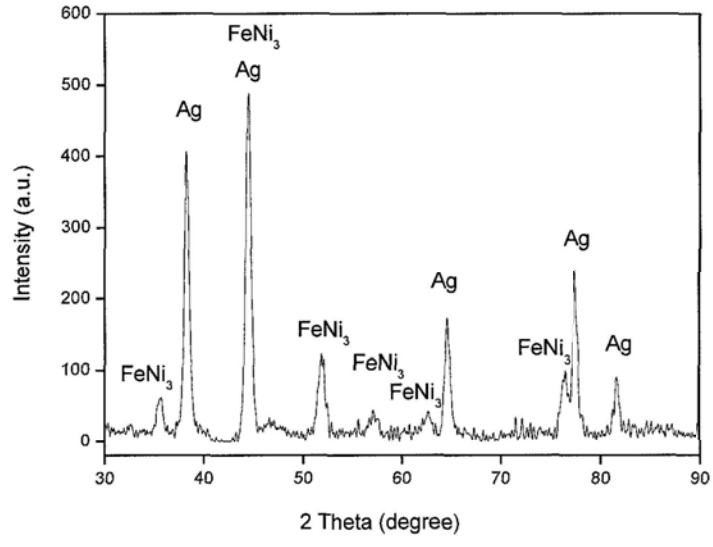

Figure 4.1 XRD pattern of the as-prepared Ag@$FeNi_3$ nanospheres.

The morphology of the as-obtained products was characterized by FESEM and TEM. A general overview FESEM image in Fig. 4.2a shows that the product is composed of nanoparticles with a diameter of 90 nm. Representative TEM image (Fig. 4.2b) also shows the core/shell structure of the nanospheres, and a high-magnification TEM image (Fig. 4.2c) shows that the thickness of outer shell is about 15nm, and the diameter of Ag in the centre is about 60 nm. Fig. 4.2d shows a HRTEM image at the edge of an individual Ag@FeNi$_3$ nanosphere. As shown in Fig. 3d, the results suggest that the products are polycrystalline. The local elemental composition of the as-formed nanospheres was studied by EDX microanalysis at the single-nanosphere level, focused on the whole nanosphere and the centre part separately, shown in Fig. 4.3. It confirms that the nanospheres are composed of Fe, Ni, Ag, C and O elements, the presence of C and O elements is due to stabilizer PVP. The molar ratios of all elements are inserted in the Fig. 4.3(a-b). The results show the amount of Ag in the core is much higher than the whole nanosphere, while Ni, Fe, C and O mainly in the shell. Fig. 4.4a-d show the typical high angle annular dark field scanning TEM (HAADF-STEM) and EDX elemental mapping images of an individual nanosphere. The results also confirm the existence and distribution of Fe, Ni, Ag, C and O elements, and Ag is in the centre, while Ni, Fe, C and O surrounding in the outer shell.

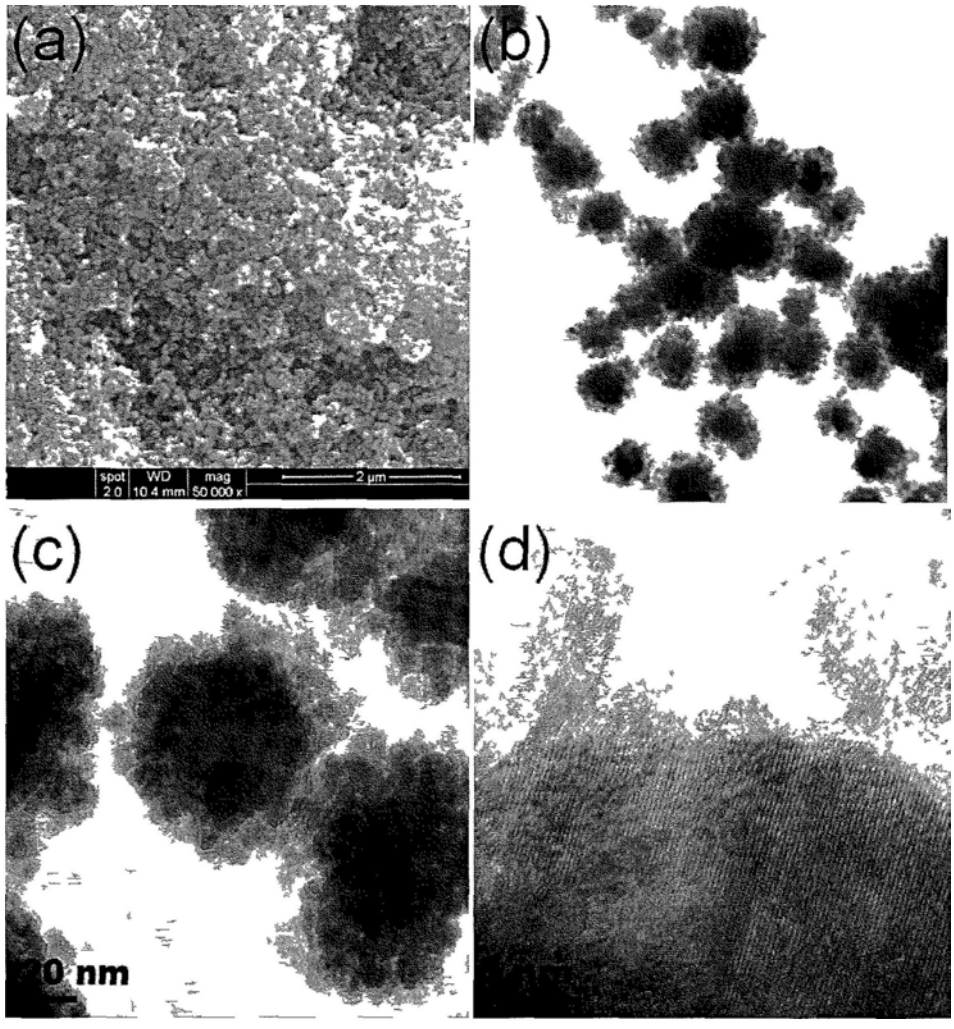

Figure 4.2 (a) FESEM image of the as-prepared Ag@FeNi$_3$ nanospheres. (b, c) Bright-field TEM and enlarged TEM image of the as-prepared nanospheres. (d) Typical HRTEM image indicating the crystalline nature of the nanospheres.

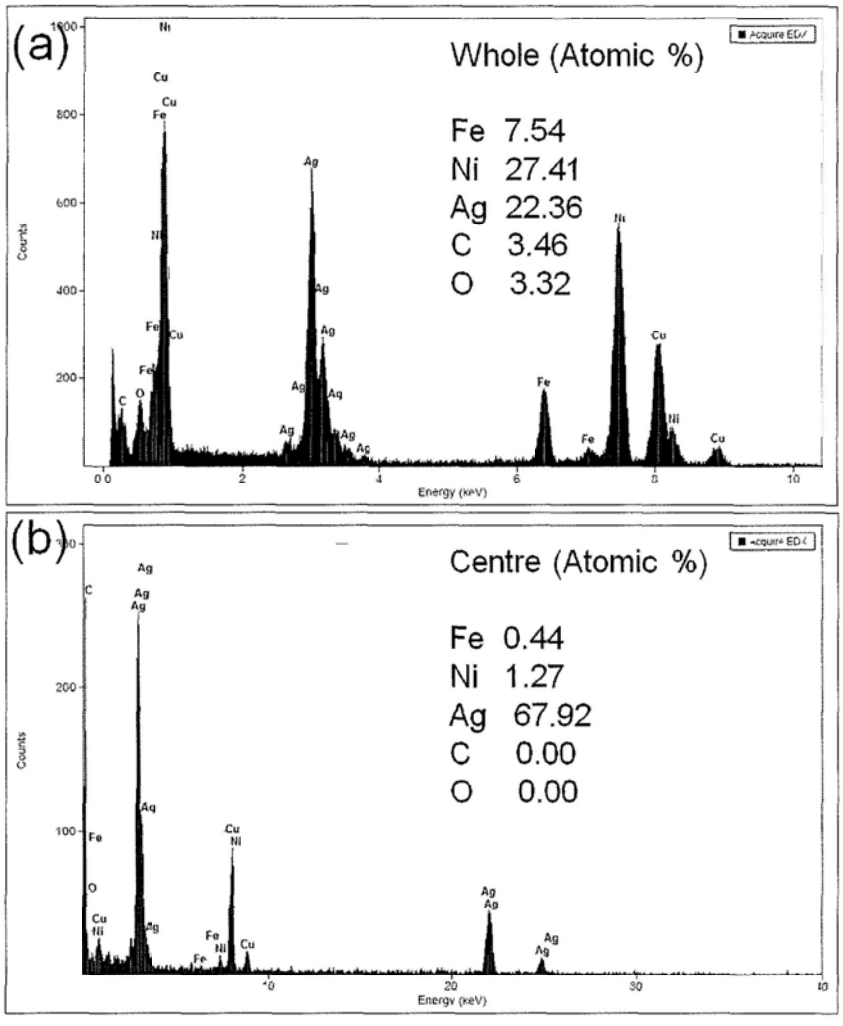

Figure 4.3 (a) EDX spectrum of a single Ag@FeNi$_3$ nanosphere, (b) EDX spectrum focused on the centre part of the nanosphere, where the signals of Cu are generated from the Cu grids.

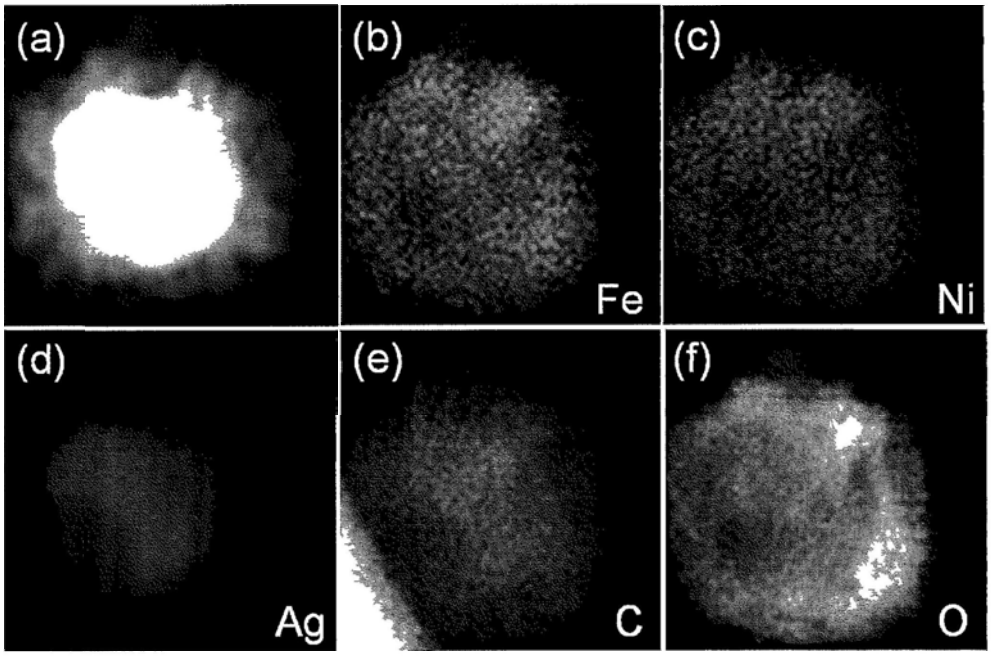

Figure 4.4 (a) HAADF-STEM and (b-f) elemental mapping images of a single Ag@FeNi$_3$ nanosphere

Moreover, the nanostructures were characterized with the FTIR spectrum, as shown in Fig. 4.5. The absorption band appearing at 467 cm^{-1} and 580 cm^{-1} are corresponding to Fe-O bond and Ni-O band separately, which totally with the published results.[37,38] The absorption band at 1630 cm^{-1} is assigned to the stretching vibration mode of the poly(vinylpyrrolidone) carbonyl, C=O (PVP), in the nanoparticle suspensions. The shift of the PVP carbonyl position, compared to the C=O (PVP) adsorption position at 1679 cm^{-1} and to the C=O (PVP-EG) position at 1630 cm^{-1}, is essentially due to the interaction between C=O (PVP) and $FeNi_3$ nanoalloy surface. This result is in good agreement with those reported in earlier studies where it has been concluded that the PVP can protect the metal nanoparticles via the carbonyl group. [39-41]

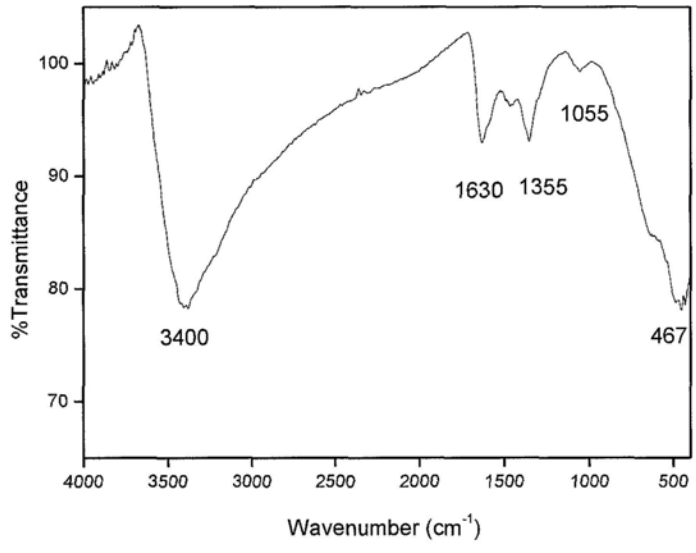

Figure 4.5 FT-IR spectrum of the Ag@$FeNi_3$ nanospheres.

Fig. 4.6 shows the nitrogen adsorption/desorption isotherms of the Ag@FeNi$_3$ nanospheres. The isotherm was of type IV classification, showing typical hysteresis loops of mesoporous materials and further confirming the nanosphere structure. The Ag@FeNi$_3$ nanospheres had a surface area of 16.05 m^2 g^{-1}. It can be clearly seen that two peaks appear on the pore size distribution curve. One peak was located at around 3.4 nm, corresponding to filling of the pores formed in the nanospheres. The other peak was centered at 16.7 nm, corresponding to filling of the pores formed among the nanospheres. The single point adsorption total volume at $P/P_0 = 0.973$ of nanospheres is 0.064 cm^3/g.

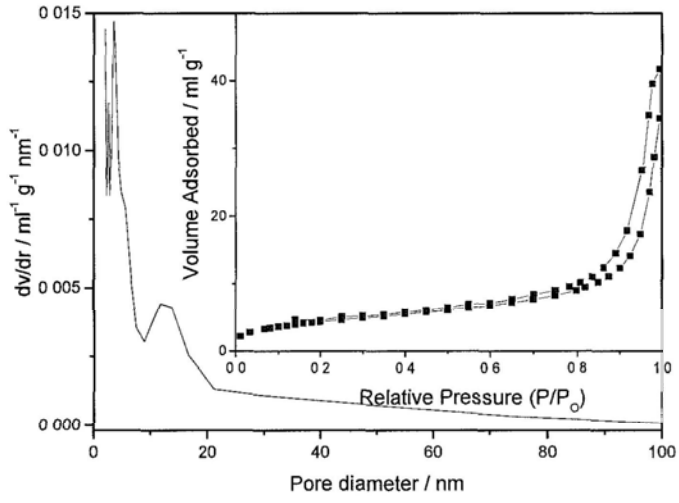

Figure 4.6 The pore size distribution curve and corresponding N_2-sorption isotherm (inset) for the Ag@FeNi$_3$ nanospheres.

The magnetic properties of the products were characterized by VSM. Fig. 4.7 shows the room-temperature magnetization hysteresis loop. Clearly, it reveals a typical ferromagnetic behavior with saturation magnetization (Ms) of 10.50 emu g^{-1} and coercivity field (Hc) of 132.0 Oe. The hysteresis curve is symmetric in shape with respect to zero magnetic field. It is worth noting that the Ni_3Fe exhibit significantly enhanced magnetic coercivity (about 244 times higher) compared with that of bulk $FeNi_3$ (0.54 Oe), and the saturation magnetization is about 70 times higher than the monodispersed Ni_3Fe nanospheres (0.15 emu g^{-1}).[21] This may be ascribed to the distinctive anisotropic structure and hierarchical surfaces of the magnetic nanospheres.

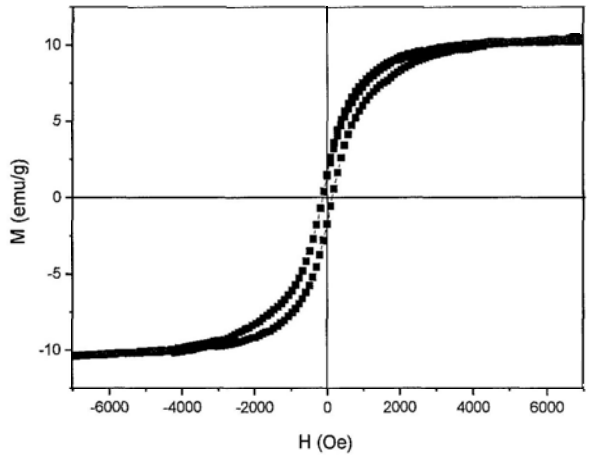

Figure 4.7 The hysteresis loop of the Ag@$FeNi_3$ nanospheres at 300 K.

4.3.2. Toxicity test of Ag@FeNi$_3$ nanospheres by using zebrafish larvae.

While rapid development of nanomaterials will certainly continue, the application of these materials will be limited by their inherent toxicity.[42,43] Thus, the need for evaluating nanotoxicity is becoming increasingly paramount. Transparent zebrafish, possessing a high degree of homology to the human genome, offers an economically feasible platform for noninvasive real-time assessments of nanotoxicity.[44] Toxicity of the as-prepared Ag@FeNi$_3$ nanospheres was evaluated using zebrafish as a model. Fig. 4.8 shows in detail the hatching rate of zebrafish larvae at different concentrations of nanospheres (0, 0.5, 1, 5, 10, 25, 50 mg/L) after 96h exposure. The silver nanoparticles (shown in Fig. 4.9) and FeNi$_3$ nanoparticles (prepared in chapter 1) were used by comparison.

The results in Fig. 4.8 show that the FeNi$_3$ is nontoxic to zebrafish, corresponding to our former report, silver nanoparticles are toxic, it is because that Ag^+ ions can get released from Ag nanopartciles under the complex physiological conditions. Ag@FeNi$_3$ nanospheres treated embryos showed much higher hatching rate when compared to Ag nanoparticles. Hence, these results confirm that Ag@FeNi$_3$ nanospheres has reduced the toxicity compared to Ag nanoparticles, this is mainly because the outer shell FeNi$_3$ and PVP are of good biocompatibility, which have prevented the release of silver.

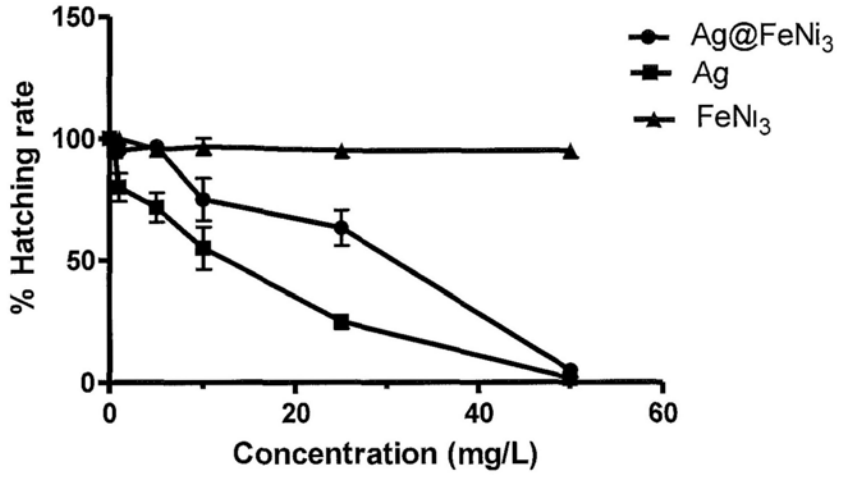

Figure 4.8 Hatching rate of zebrafish embryos treated by $FeNi_3$ nanoparticles, Ag nanoparticles and Ag@$FeNi_3$ nanospheres at different concentrations after 96h exposure.

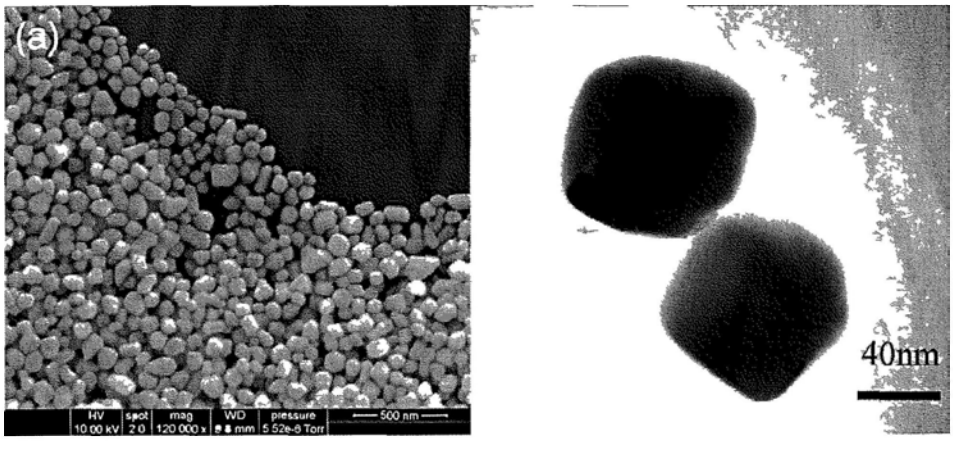

Figure 4.9 (a) FESEM image of the as-prepared Ag nanparticles, and (b) Bright-field TEM image of the as-prepared Ag nanparticles.

4.3.3 *In vitro* MRI of of Ag@FeNi$_3$ nanospheres.

Fig. 4.10 shows *in vitro* MRI of Ag@FeNi$_3$ nanospheres suspended in DI water at the different concentrations of nanochains (0, 0.006, 0.015, 0.030, 0.15, 0 30mM). The Ag@FeNi$_3$ nanospheres resulted in signal decrease in a concentration dependant manner, with higher concentration leading to darker signal. These results demonstrate that this kind of magnetic nanospheres has the potential to be used as a T_2 MRI contrast agent.

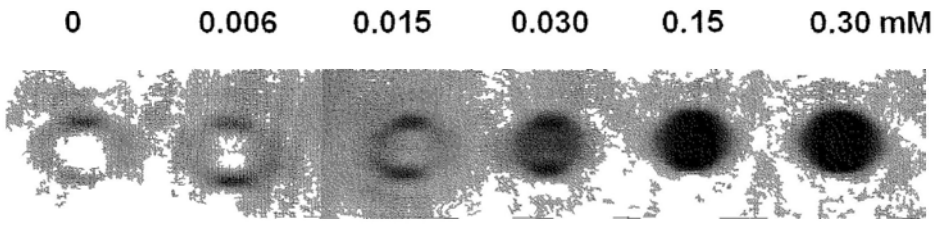

Figure 4.10 T_2-weighted magnetic resonance spin echo images of the prepared Ag@FeNi$_3$ nanospheres in DI water (1 5Tesla, TR = 2000 msec, TE=92 msec).

4.3.4 Metal-enhanced fluorescence (MEF) of organic dyes using Ag@FeNi$_3$ nanospheres.

UV-Vis spectra, shown in Fig. 4.11, displayed the optical spectra of the FeNi$_3$ nanoparticles, Ag@FeNi$_3$ nanospheres, RhB, and the RhB-doped Ag@FeNi$_3$ nanospheres before and after purification. The absorption peak of RhB appears at 546 nm, while there is no absorption of FeNi$_3$ nanoparticles, and the Ag surface plasmon was observed at 425 nm in the spectrum of Ag@FeNi$_3$ nanospheres. On the other hand, the clear absorption peaks appear at 535 nm and 544 nm of the RhB-doped Ag@FeNi$_3$ nanospheres before and after purification, implying that the Ag@FeNi$_3$ nanospheres indeed change the absorption of RhB.

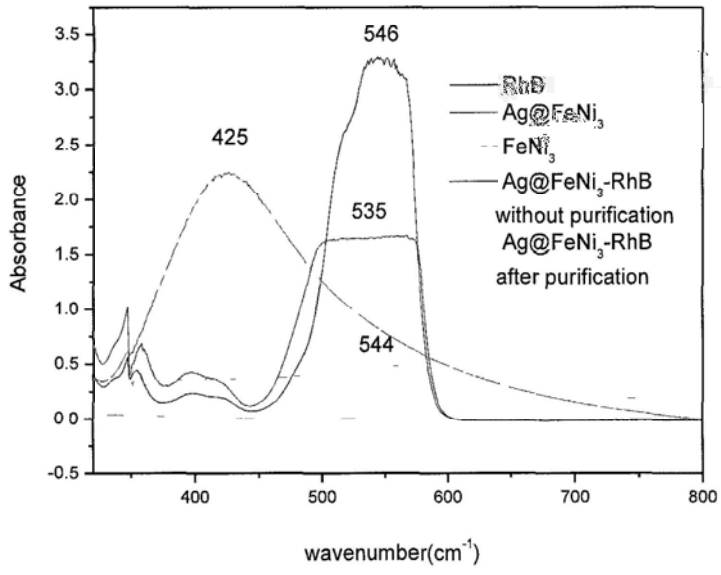

Figure 4.11 UV/Vis spectra of solutions of the FeNi$_3$ nanoparticles, Ag@FeNi$_3$ nanospheres, RhB, and RhB-doped Ag@FeNi$_3$ nanospheres before and after purification. All samples were dispersed in ethanol solution.

Fig. 4.12 shows the fluorescence emission intensity from RhB-doped Ag@FeNi$_3$ nanospheres, RhB-doped FeNi$_3$ nanoparticles and from the pure Ag@FeNi$_3$ nanospheres (control samples). The emission intensity was approximately 8-fold higher for RhB-doped Ag@FeNi$_3$ nanospheres than for RhB-doped FeNi$_3$ nanoparticles. We also note that the fluorescence emission spectra of the fluorophores were identical in both cases, indicating that the spectral properties of the fluorophores were retained. And there is no fluorescence emission for pure Ag@FeNi$_3$ nanospheres.

Finally, a bright field image and the corresponding confocal fluorescent microscopy image (Fig. 4.13) shows that the RhB-doped Ag@FeNi$_3$ nanospheres are well-dispersed and have high luminescent intensity, suggesting that the particles were successfully modified with RhB molecules.

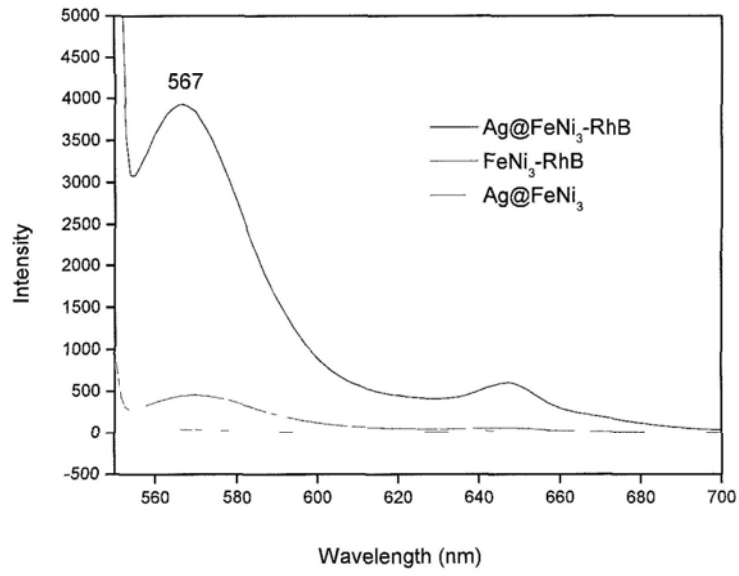

Figure 4.12 Fluorescence emission intensity of RhB-doped Ag@FeNi$_3$ nanospheres, RhB-doped FeNi$_3$ nanoparticles and the pure Ag@FeNi$_3$ nanospheres.

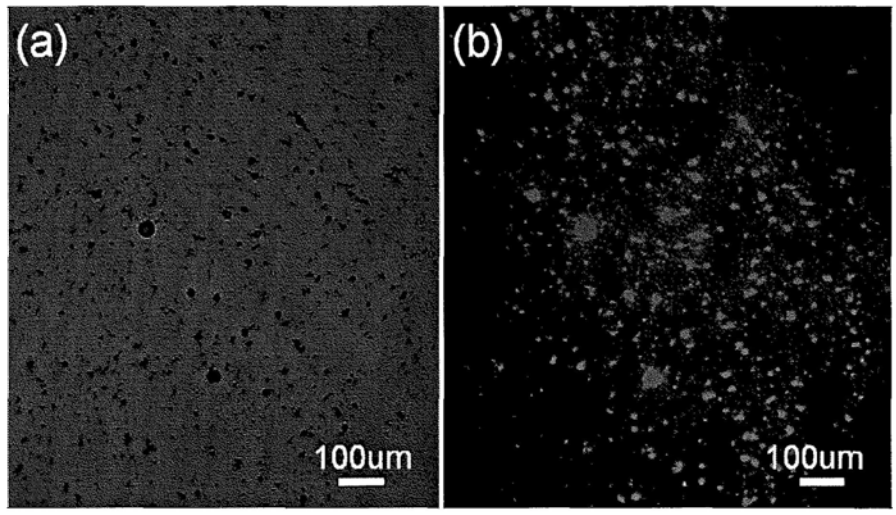

Figure 4.13 (a) Bright-field image and (b) the corresponding confocal luminescence image of RhB-doped Ag@FeNi$_3$ nanospheres. (Excited at laser of wavelength of 408 nm)

4.4 Conclusions

Bifunctional mesoporous core/shell Ag@FeNi$_3$ nanospheres were synthesized by reducing iron(III) chloride, nickel(II) chloride and silver nitrate with hydrazine in ethylene glycol under microwave irradiation. This is an efficient microwave-hydrothermal process which significantly shortens the synthesis time to one minute. The as-prepared products were characterized by field emission scanning electron microscopy (FESEM), transmission electron microscopy (TEM), X-ray diffraction (XRD), and high-resolution transmission electron microscopy (HRTEM),

energy-dispersive X-ray (EDX) spectroscopy, elemental mapping, X-ray photoelectron spectroscopy (XPS). Toxicity of Ag@$FeNi_3$ nanospheres has been reduced compared to silver nanoparticles by exposuring to zebra fish. *In vitro* MRI confirmed the effectiveness of the Ag@$FeNi_3$ nanospheres as sensitive MRI probes. The interaction of Rhodamine B and nanospheres showed greatly enhanced fluorescence over the $FeNi_3$ nanoparticles.

4.5 References

(1) Caruso, F. *Adv. Mater.* **2001**, *13*, 11.

(2) Sun, X.; Li, Y. *Angew. Chem. Int. Ed.* **2004**, *43*, 597.

(3) Tang, C.; Qi, K.; Wooley, K. L.; Matyjaszewski, K.; Kowalewski, T. *Angew. Chem. Int. Ed.* **2004**, *43*, 2783.

(4) Aizawa, M.; Buriak, J. M. *J. Am. Chem. Soc.* **2006**, *128*, 5877.

(5) Lahav, M.; Weiss, E. A.; Xu, Q. B.; Whitesides, G. M. *Nano Lett.* **2006**, *6*, 2166.

(6) Yang, Y. H.; Gao, M. Y. *Adv. Mater.* **2005**, *17*, 2354.

(7) Zhang, H. F.; Wang, C. M.; Wang, L. S. *Nano Lett.* **2002**, *2*, 941.

(8) Xu, C. J.; Xie, J.; Ho, D.; Wang, C.; Kohler, N.; Walsh, E. G.; Morgan, J. R.; Chin, Y. E.; Sun, S. H. *Angew. Chem. Int. Ed.* **2008**, *47*, 173.

(9) Tremel, W.; Kleinke, H.; Derstroff, V.; Reisner, C. *J. Alloys Compd.* **1995**, *219*, 73.

(10) Sun, S. H.; Anders, S.; Hamann, H. F.; Thiele, J. U.; Baglin, J. E. E.; Thomson, T.; Fullerton, E. E.; Murray, C. B.; Terris, B. D. *J. Am. Chem. Soc.* **2002**, *124*, 2884.

(11) Sun, S. H.; Fullerton, E. E.; Weller, D.; Murray, C. B. *IEEE Trans. Magn.* **2001**, *37*, 1239.

(12) Park, J. I.; Cheon, J. *J. Am. Chem. Soc.* **2001**, *123*, 5743.

(13) Kiely, C. J.; Fink, J.; Zheng, J. G.; Brust, M.; Bethell, D.; Schiffrin, D. J. *Adv. Mater.* **2000**, *12*, 640.

(14) Chaubey, G. S.; Barcena, C.; Poudyal, N.; Rong, C. B.; Gao, J. M.; Sun, S. H.; Liu, J. P. *J. Am. Chem. Soc.* **2007**, *129*, 7214.

(15) Robinson, I.; Zacchini, S.; Tung, L. D.; Maenosono, S.; Thanh, N. T. K. *Chem. Mater.* **2009**, *21*, 3021.

(16) Jia, J. C.; Yu, J. C.; Wang, Y. X.; Chan, K. M. *ACS Appl. Mater. Interfaces,* **2010**, *2*, 2579.

(17) Datta, A.; Pal, M.; Chakravorty, D.; Das, D.; Chintalapudi, S. N. *J. Magn. Magn. Mater.* **1999**, *205*, 301.

(18) Bac, L.H.; Kwon, Y.S.; Kim, J.S.; Lee, Y.I.; Lee, D.W.; Kim, J.C. *Mater. Res. Bull.* **2010**, *45*, 352.

(19) Wang, H. Z.; Li, J.G.; Kou, X. L.; Zhang, L. *J. Cryst. Growth* **2008**, *310*, 3072.

(20) Lu, X. G.; Liang, G. Y.; Zhang Y. M. *Mater. Sci. Eng., B* **2007**, *139*, 124.

(21) Liao, Q. L.; Tannenbaum, R.; Wang Z. L. *J. Phys. Chem. B*, **2006**, 110, 14262.

(22) Brown, M. A.; Semelka, R. C. *MRI: Basic Principles and Applications*, Wiley-Liss, New York **2003**.

(23) Aslan, K.; Gryczynski, I.; Malicka, J.; Matveeva, E.; Lakowicz, J. R.; Geddes, C. D. *Curr. Opin. Biotechnol.* **2005**, *16*, 55.

(24) Ray, K.; Badugu, R.; Lakowicz, J. R. *J. Am. Chem. Soc.* **2006**, *128*, 8998-8999.

(25) Malicka, J.; Gryczynski, I.; Kusba, J.; Lakowicz, J. R. *Biopolymers* **2003**, *70*, 595.

(26) Aslan, K.; Leonenko, Z.; Lakowicz, J. R.; Geddes, C. D. *J. Fluoresc.* **2005**, *15*, 643.

(27) Lin, J.; Zhou, W.; Kumbhar, A.; Fang, J.; Carpenter, E. E.; O'Connor, C. J. *J. Solid State Chem.* **2001**, *159*, 26.

(28) Xu, H. K.; Sorensen, C. M.; Klabunde, K. J.; Hadjipanayis, G. C. *J. Mater. Reson.* **1992**, *7*, 712.

(29) Tartaj, P.; Gonzalez-Carreno, T.; Serna, C. J. *Langmuir* **2002**, *18*, 4556.

(30) Tartaj, P.; Gonzalez-Carreno, T.; Serna, C. J. *Adv. Mater.* **2001**, *13*, 1620.

(31) Santra, S.; Tapec, R.; Theodoropoulou, N.; Dobson, J.; Hebard, A.; Tan, W. *Langmuir* **2001**, *17*, 2900.

(32) Mulvaney, P. *Langmuir* **1996**, *12*, 788.

(33) Link, S.; Wang, Z. L.; El-Sayed, M. A. *J. Phys. Chem. B* **1999**, *103*, 3529.

(34) Ow, H.; Larson, D. R.; Srivastava, M.; Baird, B. A.; Webb, W. W.; Wiesner, U. *Nano Lett.* **2005**, *5* (1), 113-117.

(35) Westerfield, M.; *The Zebrafish Book.* Edition 5, University of Oregon Press, Eugene. **2007**; pp 2.1-3.44.

(36) International Organization for Standardization; ISO 7346-2 Water quality-determination of the actual lethal toxicity of substances to a freshwater fish [*Brachydanio rerio* Hamilton-Buchanan (Teleostei, Cyprinidae)] Part 2: Semi-static method. 1996.

(37) Tang, D. P.; Yuan, R.; Chai, Y. Q. *J. Phys. Chem. B* **2006,** *110,* 11640.

(38) Cornell, R. M.; Schwertmann, U. *The Iron Oxides*: *Structure*, *Properties*, *Reactions*, *Occurrence and Uses*, VCH: New York, **1996**; Vol. 134.

(39) Szaraz, I.; Forsling, W. *Langmuir* **2001**, *17*, 3987.

(40) Koo, C.M.; Ham, H.T.; Choi, M.H.; Kim, S.O.; Chung, I. *J. Polymer* **2003**, *44*, 681.

(41) Teranishi, T.; Miyake, M. *Chem. Mater.* **1998**, *10*, 594.

(42) Oberdorster, G.; Oberdorster, E.; Oberdorster, J. *Environ. Health Perspect.* **2005**, *113,* 823-839.

(43) Grainger, D. W.; Castner, D. G. *Adv. Mater.* **2008**, *20*, 867-877.

(44) Bar-llan, O.; Albrecht, R. M.; Fako, V. E.; Furgeson, D. Y. *Small* **2009**, *5*, 1897-1910.

Chapter Five

Shape-Controlled Synthesis of Core/Shell Silver/Phenol Formaldehyde Resin Nano/Microstructures through Self-Assembly Growth

5.1 Introduction

In the past decades, systematic control over the desired morphologies and architectures of nano-/microparticles with well-defined shapes and sizes or higher order superstructures has attracted more and more interest due to their strong influence on materials properties.[1,2] since the size, shape, morphology, dimensionality, and texture of the nano-/microcrystals and their assembly architectures have significant influences on varying their optical, electronic, catalytic, and magnetic properties.[3,4] Reasonable control of different factors allows us not only to obtain the materials with unique properties but also to adjust their chemical and physical

properties as expected. Therefore, when synthetic methods were explored to generate nano-/microstructures, the simultaneous control over dimension, morphology, shape, and uniformity is one of the most important issues concerned.

Among the different morphologies of nanomaterials, hollow cage-like structures of nanometer to micrometer dimensions have received much attention because of their widespread potential applications in catalysis, drug delivery, chromatography separation, chemical reactors, controlled release of various substances, protection of environmentally sensitive biological molecules, and lightweight filler materials.[5-8]

One-dimensional (1-D) nanostructures of metals also have drawn considerable attention because of their unique physical properties and potential applications in photonics,[9] waveguides,[10] and piezoelectronics,[11] sensors.[12] 1-D silver (Ag) nanostructures seem to be particularly interesting to investigate because of their great potential for serving as important components and interconnects in nanodevices. However, the metallic materials are very sensitive to air and moisture on the nanometer scale, which degrades the performance of the nanodevices.[13,14] Functions and properties of nanocables would be further enhanced because metal nanowires would be protected from oxidation and corrosion by outer shell and core-shell heterostructures that are formed.[15-18] As a new kind of nanostructure, coaxial nanocables are a good candidate for enhanced properties and a more diverse range of applications.[19-23]

Core/shell silver/phenol formaldehyde resin (PFR) nanospheres were prepared

by hydrothermal method and were reported to be effective green luminescent green fluorescence for in vivo bioimaging on human lung cancer cells.[24] However, the preparation and shape control over the nanostructures of core/shell silver/phenol formaldehyde resin (PFR) nano/microstructures, such as the ultralong silver/PFR coaxial nanocables and hollow silver/PFR microcages, has been met with limited success.

Herein, we will report a rapid microwave-assisted approach to fabricate hollow silver/PFR microcages and ultralong and flexible silver/PFR coaxial nanocables separately for the first time via one step. Microwave irradiation is an efficient process that becomes an increasingly popular heating method for nanomaterials synthesis.[25-27] We have successfully synthesized colloidal Fe_2O_3 nanocrystals, carbon-based interconnected cable-like Ag/C and superparamagnetic porous Fe_3O_4/C nanocomposites by taking advantage of microwave irradiation effects.[28-30] In this work, the nano/microstructures were synthesized within several minutes in the presence of different kinds of surfactants. The structure, morphology and composition of the products are investigated by changing the experiment conditions, including the amounts of precursors, the reaction time and temperature, as well as the kind of surfactants. The self-assembly mechanism of the nano/microstructures growth was further elucidated based on the experimental results. This kind of novel superstructure is also expected to have potential applications in catalyst support, drug delivery, separation technology, biomedical engineering, and nanotechnology owing to its unique cage-like structure.

5.2 Experimental Section

5.2.1 Synthesis of hollow silver/PFR microcages.

All the samples were prepared in a microwave digestion system (Ethos TC Plus 1, Milestone). The detailed conditions are listed in Table 5.1. In a typical procedure, 0.5g Pluronic P123 (EO20PO70EO20) was dissolved completely in 44mL of water, and then 0.5mL 0.1M $AgNO_3$ solution was added, then 0.2mmol phenol, 0.1mmol hexamine were added to the mixture under stirring. The solution was stirred for 5min and was sealed in a double-walled digestion vessel which was Teflon-lined and double-walled. The reaction vessel was fitted with a temperature probe that was housed in a sturdy thermowell and protected from chemical attack by a triple layer of PTFE/ceramic/PTFE. The desired exposure time and temperature were programmed by using Milestone's EasyControl software. The Automatic Temperature Control system allowed continuous monitoring and controlling (±1℃) of the internal temperature. The preset profile (desired time and temperature) was followed automatically by continuously adjusting the applied power (0-1000 W) in order to keep the reaction temperature at 220℃. After treating the mixture at 220℃ for 10 min under microwave irradiation, the vessel was cooled to room temperature. The product was collected, washed with deionized water and absolute ethanol, and dried in a vacuum at 60℃ for 4 hours.

5.2.2 Synthesis of ultralong and flexible silver/PFR coaxial nanocables.

The basic process was similar to that detailed above except the amounts of precursors are different and the surfactant used is cetyltrimethylammonium bromide, CTAB.

5.2.3 Synthesis of monodispersed silver/PFR nanospheres.

The basic process was still similar to that detailed above except different ratios of the precursors are used and in the absence of any surfactant.

Table 5.1 Summaries of the experimental results indicating the influence of the composition of a mixed solution on the shape of the product.

Sample No.	phenol [mmol]	hexamine [mmol]	$AgNO_3$ [mmol]	Surfactant	Morphology	Diameter
1	0.20	0.10	0.05	0.5g P123	microcage	1-2.5μm
2	0.20	0.10	0.05	0.25g CTAB	nanocable	200-800nm
3	0.20	0.10	0.05	-	nanosphere	110nm
4	0.30	0.15	0.05	-	nanosphere	250nm
5	0.40	0.20	0.05	-	nanosphere	370nm
6	0.50	0.25	0.05	-	nanosphere	450nm

5.2.4 Characterization of silver/PFR nano/microstructures.

The samples was examined by powder XRD with a Bruker D8 Advance diffractometer using Cu Kα_1 irradiation (λ = 1.5406 Å). Diffraction patterns were collected from 30° to 80° with a step size of 0.02°. TEM images were recorded on a CM-120 microscope (Philips, 120 kV) coupled with an EDX spectrometer (Oxford Instrument). Samples were deposited on thin amorphous carbon films supported by copper grids from ultrasonically processed ethanol solutions of the samples. The general morphology of the products was characterized by field emission scanning electron microscopy (FESEM, Quanta 400 FEG). The products were conductively coated with gold by sputtering for 30 seconds to minimize charging effects under SEM imaging conditions. The Fourier transform infrared (FTIR) spectra were recorded using a Nicolet Magna 560 FTIR spectrometer. X-ray photoelectron spectroscopy (XPS) measurements were performed on a PHI 5600 multi-technique system with a monochromatic Al K X-ray source (Physical Electronics). All the binding energies were referenced to the C1s peak at 284.6 eV of the surface adventitious carbon.

5.3 Results and discussion

5.3.1 Phase Identification.

Grey powders were obtained from the microwave-assisted reaction. Fig. 5.1 shows the X-ray diffraction (XRD) pattern of typical products. All the diffraction peaks can be indexed to cubic (face-centered cubic, fcc) Ag, which is in good agreement with the reported data (Joint Committee on Powder Diffraction Standards, JCPDS card no.: 4-783). No other impurity phases are detected.

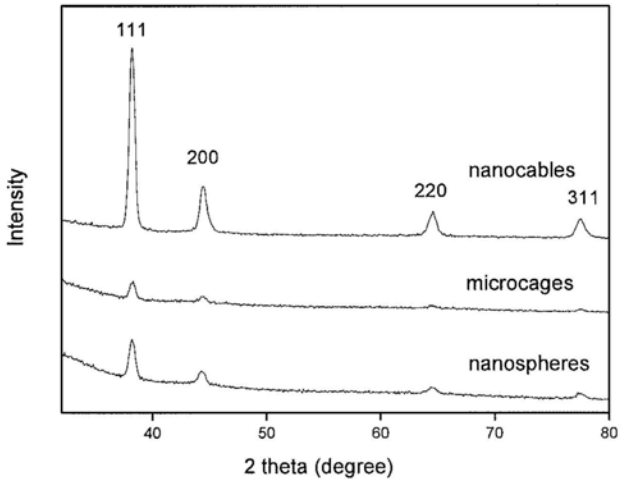

Figure 5.1 XRD patterns of the as-prepared products obtained at 220 ℃ for 10min.

Moreover, the nano/microstructures were characterized with the FTIR spectrum, as shown in Fig. 5.2. It shows that the band positions of the compound are consistent with those for PFR reported previously.[24, 32] The slight shift in wavelength may be due

to the addition of a crosslinking agent and silver nanowires or nanoparticles.[24]

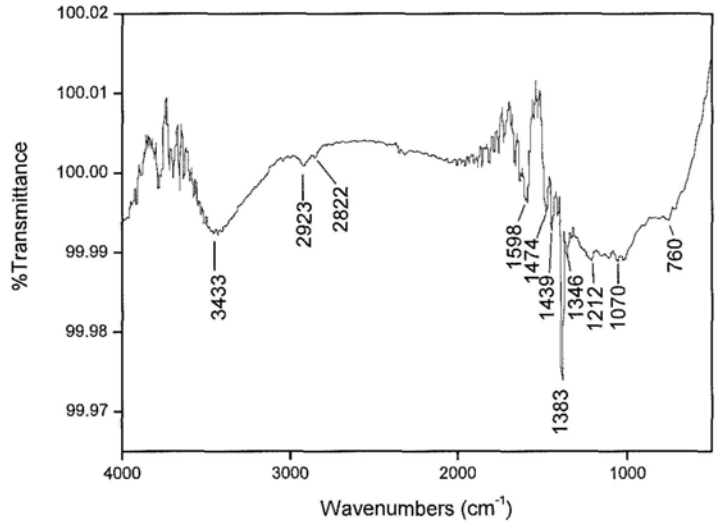

Figure 5.2 FT-IR spectrum of the Ag/PFR nano/microstructures obtained at 220 ℃ for 10min.

X-ray photoelectron spectroscopy (XPS) was used to detect the surface composition of the nano/microstructures. XPS measurements indicated that C1s and O1s binding energies of the obtained sample are 284.60 and 532.10, respectively (Fig. 5.3). However, the peaks with binding energy at 368.10 eV for Ag3d were very weak and could hardly be detected, indicating that all silver nanoparticles/nanowires in the products are confined within the shells of PFR.

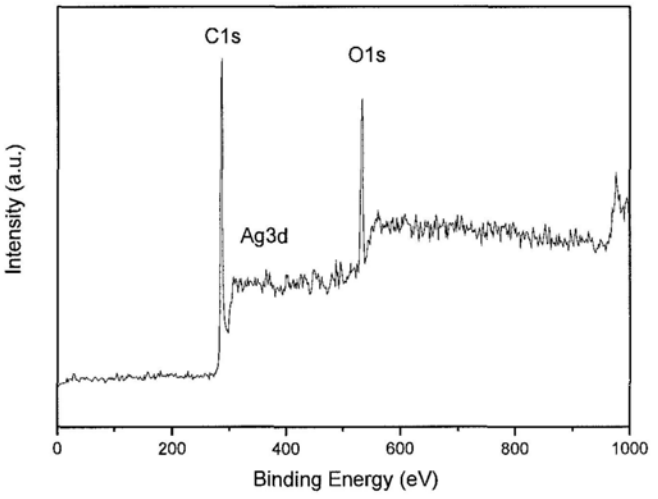

Figure 5.3 XPS spectrum of the Ag/PFR nano/microstructures obtained at 220 ℃ for 10min.

5.3.2 Surfactant Effect

Surfactants are useful in controlling morphology of nanostructures because of their soft template effect, simple manoeuvrability and reproducibility.[10] Diverse shapes of micelles can be formed from spheres to rods, ellipsoids, discs, and even more complex shapes, by adjusting experimental parameters.[17] Triblock copolymer P123 is usually used to prepare the hierarchical micron/nano-sized hollow spheres in aqueous solutions.[31-34]

The morphological varieties of the final Ag/PFR nano-/microstructures were investigated in the presence of different kinds of surfactants. The products prepared in P123 are hollow microcages, as indicated in Fig. 5.4. The morphology of the as-obtained products was characterized by FESEM and TEM. A general overview FESEM image in Fig. 5.4a shows that the product is composed of microcages with a diameter of 1-2.5 μ m. Enlarged FESEM images (Fig. 5.4b-c) show that the microcages are comprised of many core/shell nanospheres with diameters about 100nm. Representative TEM images (Fig. 5.4d-e) also clearly show the hollow and hierarchical structure of microcages. The local elemental composition of the as-formed microcages was studied by EDX microanalysis at one microcage level, shown in Fig. 5.4f. It confirms that the microcages are composed of Ag, C and O elements.

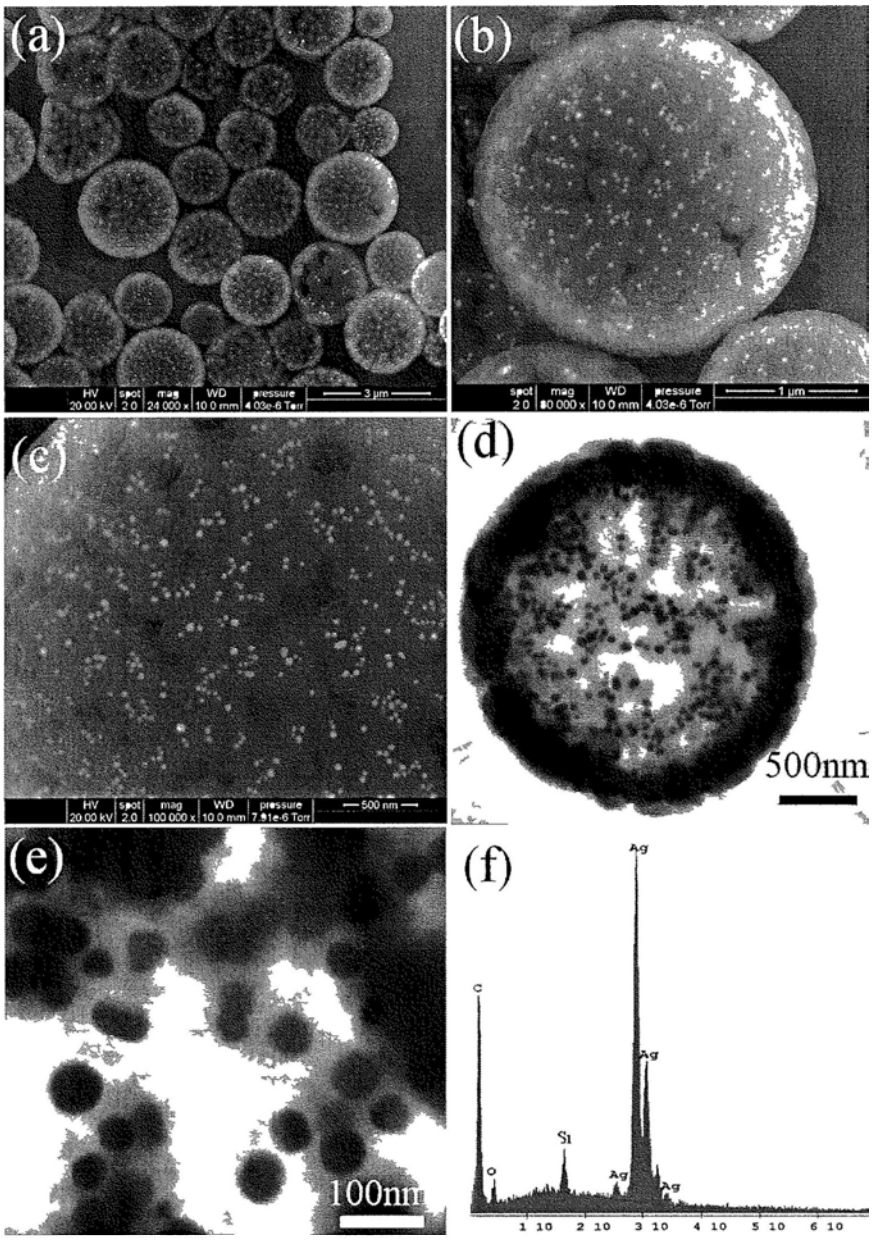

Figure 5.4 (a-c) Low- and high-magnification FESEM images of sample 1. (d, e) Bright-field TEM and enlarged TEM images of sample 1. (f) EDX spectrum of sample 1, where the signals of Si are generated from the Si wafer.

Ultralong silver/PFR coaxial nanocables were obtained when CTAB was used as surfactant instead of P123. Fig. 5.5a shows that the product is composed of flexible fibers with a diameter of 200-800nm and length more than 100 μm. TEM image (Fig. 5.5b) show that all wires are actually a composite comprised of a smooth core about 50 nm in diameter and a surrounding sheath about 150-750nm in thickness, from which the contrast between surrounding polymer and inner core can be easily observed. The insert selected-area electron diffraction (SAED) pattern (in Fig. 5.5b) by focusing an electron beam onto an individual nanocable, indicates the single-crystalline nature of the Ag core. As further support for our interpretation of the silver/PFR coaxial nanocable structure, we performed energy dispersive X-ray (EDX) analysis. Fig. 5.5d-f show the EDX line graph of a nanocable obtained in STEM mode by performing the scan shown in Fig. 5.5c. It is observed that both the carbon and oxygen peaks start at the same radial position and have the same profile across the particle. Meanwhile the small curve around 500nm clearly demonstrates the eccentric core-shell structure. Note that silver shows up sharply after carbon and oxygen and exists only in the inner part of the cable.

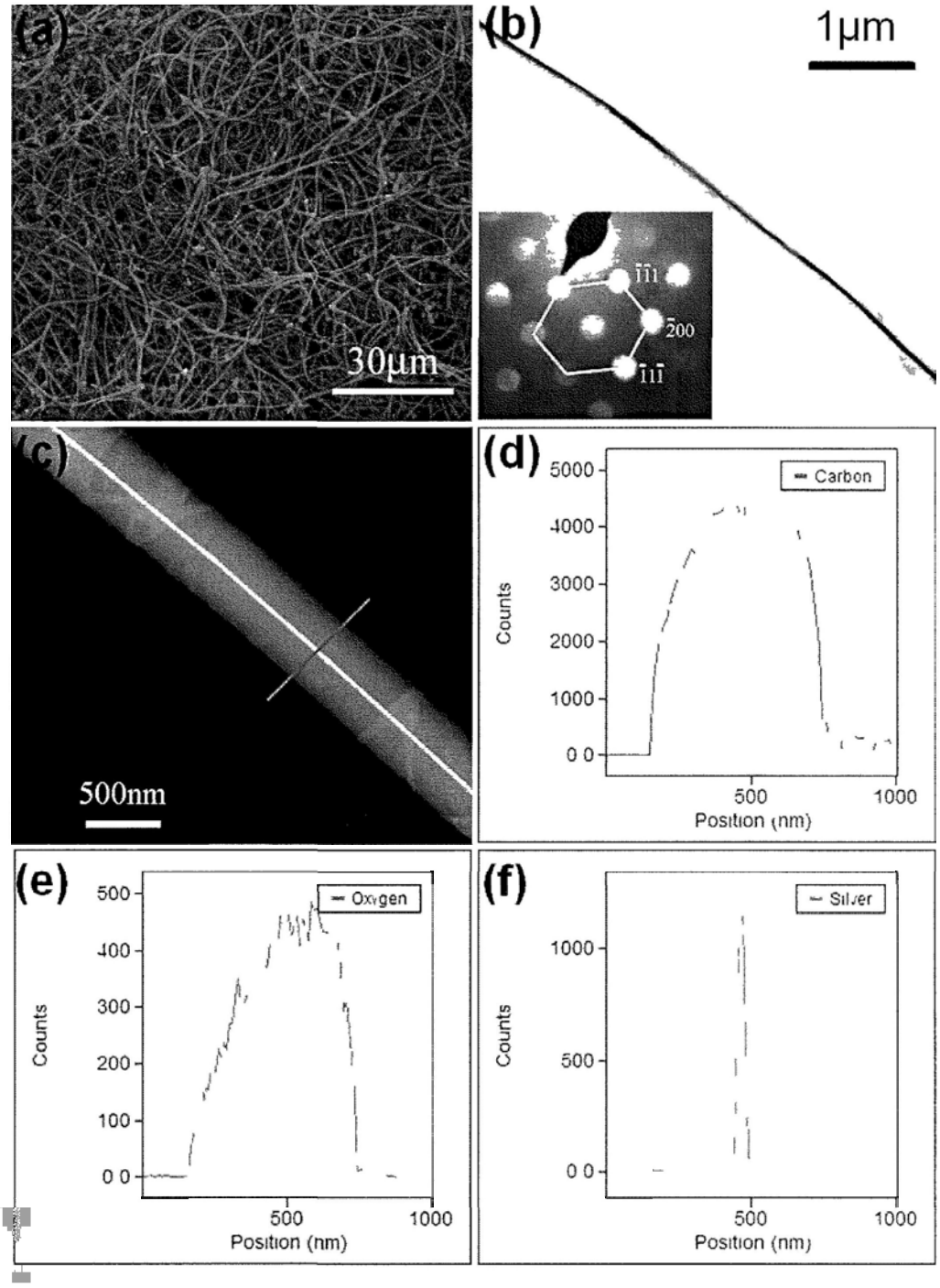

Figure 5.5 (a) FESEM and (b)TEM images of the Ag/PFR nanocables. (c) STEM dark-field image showing the EDX line-scan through the silver/PFR coaxial nanocable. (d-f) EDX line graph obtained in by performing the scan shown in (c),

scan was performed from left to right. Insert in (b): selected area electron diffraction (SAED) pattern of the nanocable.

In the absence of any surfactants, monodispersed silver/PFR nanospheres were obtained, as shown in Fig. 5.6. The effect of precursor concentrations will be discussed later.

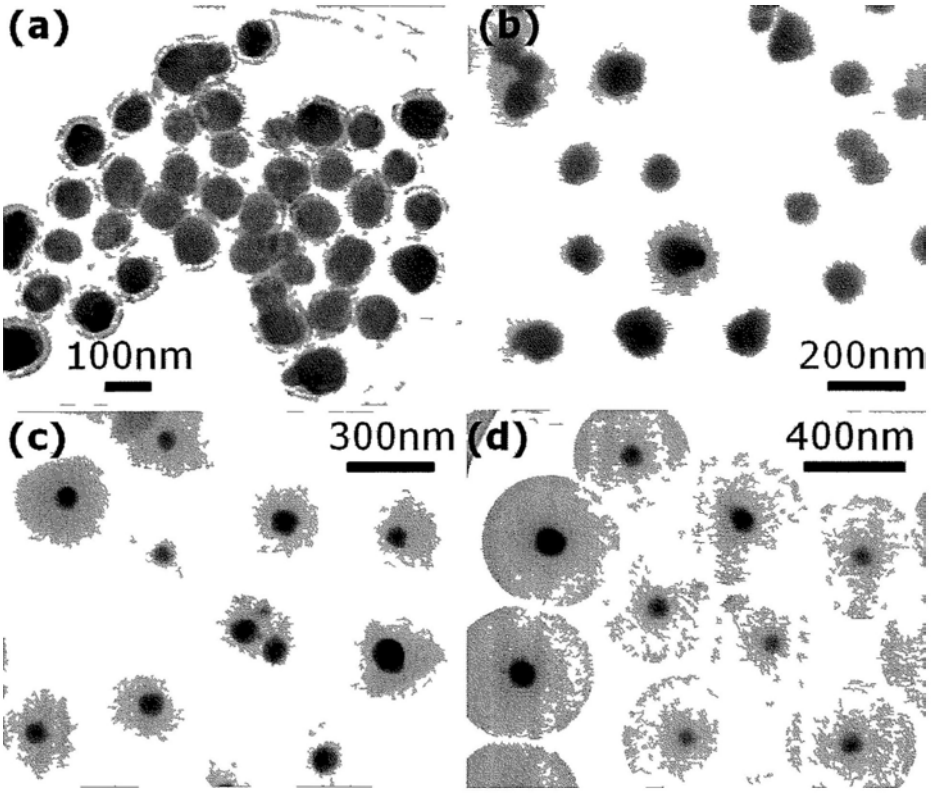

Figure 5.6 TEM images of the centered mono-core/shell spheres prepared at 220 ℃ for 10mins at various phenol/hexamine/$AgNO_3$ mole ratios (mmol/mmol/mmol) (a) 0.2:0.1:0.05, (b) 0.3:0.15:0.05, (c) 0.4:0.2:0.05, (d) 0.5:0.25:0.05.

The surfactants in the experiment seemed to play an important role in the obtained morphologies of the nano-/microstructures, the shape of micelle formed by surfactants is responsible for the morphological evolution of the final nano-/microstructures. As it is reported previously, surfactants are useful in controlling morphology of nanostructures because of their soft template effect, simple manoeuvrability and reproducibility.[10] Diverse shapes of micelles can be formed from spheres to rods, ellipsoids, discs, and even more complex shapes, by adjusting experimental parameters.[17] Triblock copolymer P123 is usually used to prepare the hierarchical micron/nano-sized hollow spheres due to the formation of spherical micelle in aqueous solutions. [31-34] Meanwhile, CTAB has been widely used as a structure-directing agent and an effective capping reagent in obtaining well controlled aspect ratio nanorods or nanowires of noble metals, because it has a tendency to form an elongated rodlike micellar structure or tubular micelle that possibly assists in nanowire formation.[18]

5.3.3 Precursor Concentrations.

We further investigated the effects of reactant concentration on the size of the silver/PFR nanospheres without surfactants, as shown in Fig. 5.6a-d. Results are summarized in Table 5.1. The amounts of (phenol:hexamine) had a significant effect on the size of the as-prepared silver/PFR nanospheres. When the amounts of phenol:hexamine were increased from 0.2 mmol:0.1 mmol to 0.5 mmol:0.25 mmol

(fixed the molar ratio of phenol:hexamine = 2:1, and the $AgNO_3$ at 0.05mol), the diameter of silver/PFR nanospheres increased from 110 nm to 450 nm gradually, while the Ag centre maintained at 90nm (Fig. 5.6a-d). This is responding to the more mass transfer for the growth of the crystal with a higher concentration of the precursor. Fig. 5.7a-d show the typical high angle annular dark field scanning TEM (HAADF-STEM) and EDX elemental mapping images of the as-prepared nanospheres. The results confirm the existence of Ag, C and O elements, and Ag is in the centre, while C and O surrounding in the outer shell.

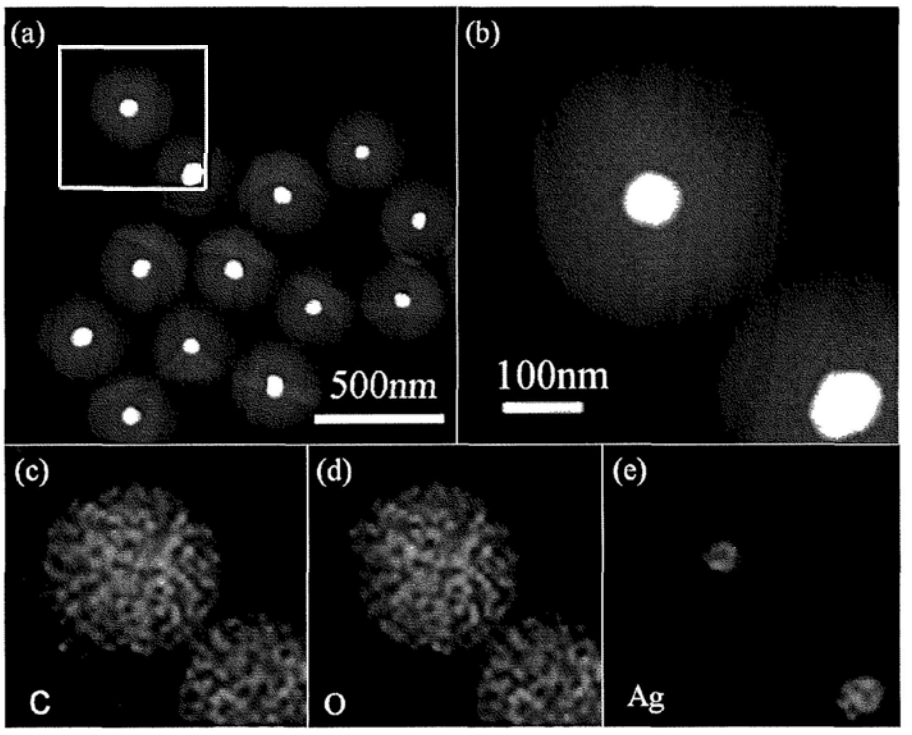

Figure 5.7 (a, b) HAADF-STEM and (c, d) elemental mapping images of core/shell Ag/PFR nanospheres.

5.3.4 Possible Growth Mechanism.

The above observation provides a clue for us to understand the detailed mechanism of Ag/PFR nano-/microstructures formation as discussed below. It can be seen that the uniform Ag/PFR microcages, nanocables, and nanospheres could be prepared by a simple microemulsion route from the same precursor. According to the results, the formation process of hollow spheres via copolymer complex micelles is schematically drawn in Scheme 5.1. It generally involves four major steps: (a) Copolymer P123 complex micelles form through complexation of silver ions with functional groups on the outer part of copolymer micelles. (b) Then phenol and hexamine are introduced into the system. During the heating process to 220 ℃, hexamine will first decompose into NH_3 and HCHO, in Equation 1. Then silver ions can be reduced to silver nanoparticles by HCHO according to Equation 2. Silver nanoparticles diffuse slowly to the circumference of the copolymer complex micelles and react with the phenol and hexamine molecules diffusing into the copolymer complex micelles. (c) Meanwhile, polymerization of PFR took place, according to Equation 3, around the silver nanoparticles and a thin polymer layer was formed. A huge core-shell structure composed of an Ag/PFR shell and a copolymer P123 core forms during the reaction of sliver nanoparticles and phenol and HCHO. (d) The copolymer is removed by washing with water, resulting in the formation of hollow core/shell spheres. Clearly, hexamine was used as both the monomer (HCHO) source for polymerization and the reducing agent for the formation of silver nanoparticles. A key advantage of the synthesis using polymeric complex micelles as soft templates is

that the size and morphology of the micelles can be easily tuned by adjusting the structure, block size, and functional groups of copolymers, as well as the solvent and the solute compositions.

$$(CH_2)_6N_4 + 6H_2O \rightarrow 4NH_3 + 6HCHO \quad (1)$$

$$Ag^+ \xrightarrow{HCHO} Ag \quad (2)$$

$$nC_6H_5OH + nHCHO \rightarrow -[C_6H_3OHCH_2]_n- \quad (3)$$

Scheme 5.1 Schematic Illustration of the Hirarchical Ag/PFR Microcages Formation Process

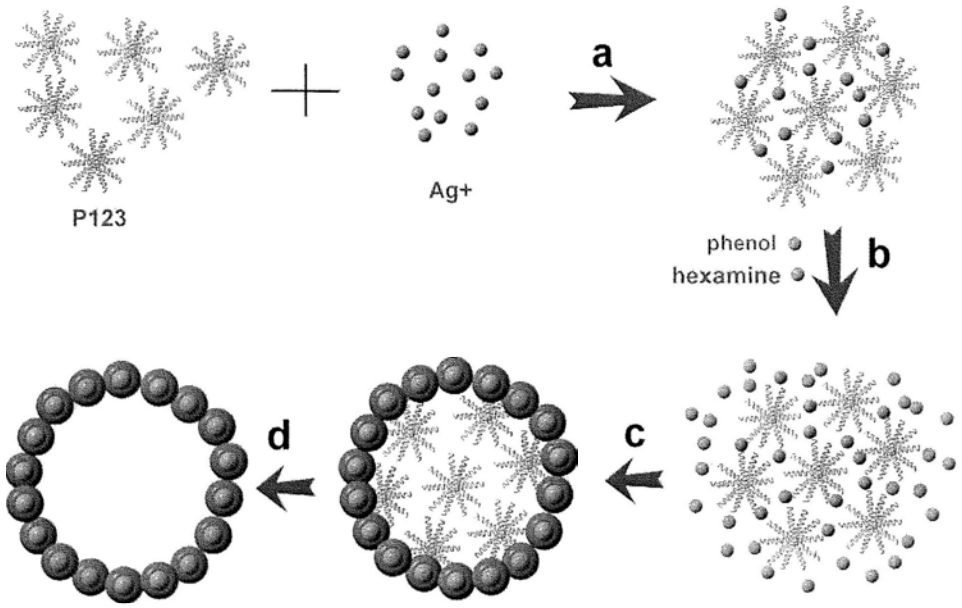

And then, the proposed formation mechanism of Ag/PFR nanocables with cross-linked structure in this work could be illustrated as Scheme 5.2. Initially, the CTAB tubular micelle structures are formed in aqueous solution containing the Ag ions inside the micelles. The Ag ions, confined within the tubular micelle, are then reduced under the reaction conditions to give Ag nanowires that replicate the structure of the tubular micellar template. So although in the nanorods synthesis the CTAB surfactant molecules act primarily as surface passivating agents, in the nanowire growth case,[20] they probably form a more rigid template that directs the growth. As the CTAB molecule is easily adsorbed onto the surfaces of particles, this can effectively prevent agglomeration of silver nanoparticles formed at the initial stage of reaction. It is helpful for Ag nanoparticles with oriented arrangement to form nanowires by the amalgamation of nanoparticles. Meanwhile, the silver wires act as a backbone on which crosslinked PFR shell will form.

Scheme 5.2 Schematic Illustration of the Ag/PFR Coaxial Nanocables Formation Process

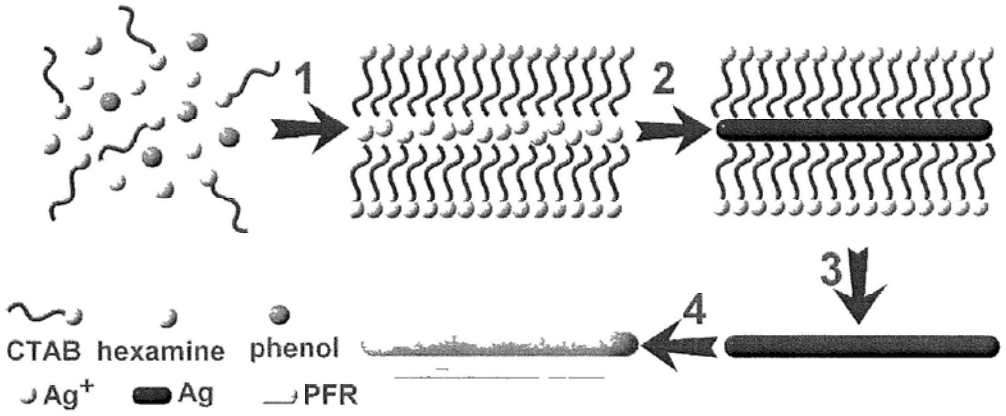

(1) Formation of CTAB tubular micelle surrounding Ag ions; (2, 3) Formation of Ag nanowires by the amalgamation of nanoparticles templated by CTAB micelle; (4) The PFR shell attached onto the surface of Ag nanowires.

5.4 Conclusions

In summary, we have reported the core/shell silver/phenol formaldehyde resin (PFR) nano/microstructures were successfully synthesized through an efficient microwave process by self-assembly growth. Various morphologies, including monodispersed nanospheres, nanocables, and microcages were achieved by tuning the

fundamental experimental parameters, such as the reaction time and the kinds of surfactants (Pluronic P123 or CTAB). The results indicate that the presence of triblock copolymer Pluronic P123 would result in hollow silver/PFR microcages, while CTAB would prefer the formation of ultralong silver/PFR coaxial nanocables. In the absence of surfactants monodispersed core/shell silver/PFR nanospheres could be obtained, and the size of the nanospheres can be controlled in the range of 110 to 450 nm by changing the ratio of reagents (phenol: hexamine). The morphology and composition of the as-prepared products were characterized by field emission scanning electron microscopy (FESEM), transmission electron microscopy (TEM), X-ray diffraction (XRD), elemental mapping and Fourier transform infrared spectra (FTIR). The formation mechanism of the products is discussed based on the obtained results. The synthesized core/shell nano/microstructures with controllable morphologies may have potential applications in biotechnology and many other fields.

5.5 References

(1) (a) Li, F.; He, J.; Zhou, W.; Wiley, J. B. *J. Am. Chem. Soc.* **2003**, *125*, 16166. (b) Li, F.; Xu, L.; Zhou, W. L.; He, J.; Baughman, R. H.; Zakhidov, A. A.; Wiley, J. B. *Adv. Mater.* **2002**, *14*, 1528. (c) Yu, J.; Liu, W.; Yu, H. *Cryst. Growth Des.* **2008**, *8*, 930. (d) Yu, J.; Su, Y.; Cheng, B. *Adv. Funct. Mater.* **2007**, *17*, 1984.

(2) (a) Colfen, H.; Mann, S. *Angew. Chem. Int. Ed.* **2003**, *42*, 2350. (b) Yu, J.; Zhang, L.; Cheng, B.; Su, Y. *J. Phys. Chem. C* **2007**, *111*, 10582.

(3) (a) Peng, X. G.; Manna, L.; Yang, W.; Wickham, J.; Scher, E.; Kadavanich,A.; Alivisatos,A. P. *Nature* **2000**, *404*, 59. (b)Alivisatos, A. P. *Science* **1996**, *271*, 933.

(4) (a) Jin, R.; Cao, Y.; Mirkin, C. A.; Kelly, K. L.; Schatz, G. C.; Zheng, J. G. *Science* **2001**, *294*, 1901. (b) Shi, H.; Qi, L.; Ma, J.; Cheng, H. *J. Am. Chem. Soc.* **2003**, *125*, 3450. (c) Xie, Y.; Huang, J. X.; Li, B.; Liu, Y.; Qian, Y. T. *Adv. Mater.* **2000**, *12*, 1523.

(5) (a) Caruso, F.; Caruso, R. A.; Mohwald, H. *Science* **1998**, *282*, 1111. (b) Caruso, F. *Adv. Mater.* **2001**, *13*, 740.

(6) Zhong, Z.; Yin, Y.; Gates, B.; Xia, Y. *Adv. Mater.* **2000**, *12*, 206.

(7) Fowler, C. E.; Khushalani, D.; Mann, S. *J. Mater. Chem.* **2001**, *11*, 1968.

(8) Yu, J.; Yu, X.; Huang, B.; Zhang, X.; Dai, Y. *Cryst. Growth Des.* **2009**, *9*, 1474.

(9) (a) Mcalpine, M. C.; Friedman, R. S.; Lieber, C. M. *Proc. IEEE* **2005**, *93*, 1357-1363. (b) Nakayama, Y.; Pauzauskie, P. J.; Radenovic, A.; Onarato, R. M.;

Saykally, R. J.; Liphardt, J.; Yang, P. *Nature* **2007**, *447*, 1098.

(10) (a) Tong, L.; Gattass, R. R.; Ashcom, J. B.; He, S.; Lou, J.; Shen, M.; Maxwell, I.; Mazur, E. *Nature* **2003**, *426*, 816. (b) Barrelet, C. J.; Greytak, A. B.; Lieber, C. M. *Nano Lett* **2004**, *4*, 1981. (c) Law, M.; Sirbuly, D. J.; Johnson, J. C.; Goldberger, J.; Saykally, R. J.; Yang, P. *Science* **2004**, *305*, 1269.

(11) (a) Wang, Z. L.; Song, J. *Science* **2006**, *312*, 242. (b) Wang, C.; Hu, Y.J.; Lieber C. M., and Sun S.H. *J. Am. Chem. Soc.* **2008**, *130*, 8902.

(12) (a) Zheng, G.; Patolsky, F.; Cui, Y.; Wang, W. U.; Lieber, C. M. *Nat. Biotechnol.* **2005**, *23*, 1294. (b) McAlpine, M. C.; Ahmad, H.; Wang, D.; Heath, J. R. *Nat. Mater.* **2007**, *6*, 379.

(13) Cao, H.; Xu, Z.; Sang, H.; Sheng, D.; Tie, C. *Adv. Mater.* **2001,** *13*, 121.

(14) Sun, Y. G.; Yin, Y. D.; Mayers, B. T.; Herricks, T.; Xia, Y N. *Chem. Mater.* **2002**, *14*, 4736.

(15) Li, Q.; Wang, C. R. *J. Am. Chem. Soc.* **2003,** *125,* 9892.

(16) Morales, A. M.; Lieber, C. M. *Science* **1998,** *279,* 208.

(17) Wu, Y. Y.; Yang, P. D. *Appl. Phys. Lett.* **2000,** *77,* 43.

(18) Song, X. C.; Zhao, Y.; Zheng, Y. F.; Yang, E.; Fu, J.; He, Y. *Cryst. Growth Des.* **2008,** *8*, 1823.

(19) Shi, W. S.; Peng, H. Y.; Xu, L.; Wang, N.; Tang, Y. H. H.; Lee, S. T. *Adv. Mater.* **2000,** *12,* 1927.

(20) Zhang, M.; Bando, Y.; Wada, K. *J. Mater. Res.* **2001,** *16,* 1408.

(21) Yu, J.C.; Hu, X.L.; Li, Q.; Zhang, L.Z. *Chem. Commun.* **2005,** 2704.

(22) Luo, L. B.; Yu, S. H.; Qian, H. S.; Zhou T. *J. Am. Chem. Soc.*, **2005,** *127 (9)*, 2822.

(23) Fang, Z.; Tang, K. B.; Lei, S. J.; Li, T. Y. *Nanotechnology* **2006,** *17,* 3008.

(24) Guo, S.R.; Gong, J.Y.; Jiang, P.; Wu, M.; Lu, Y.; Yu, S.H. *Adv. Funct. Mater.* **2008,** *18,* 872.

(25) Tsuji, M.; Hashimoto, M.; Nishizawa, Y.; Kubokawa, M.; Tsuji, T. *Chem. Eur. J.* **2005**, *11*, 440.

(26) Makhluf, S.; Dror, R.; Nitzan, Y.; Abramovich, Y.; Jelinek, R.; Gedanken, A. *Adv. Funct. Mater.* **2005**, *15*, 1708.

(27) Panda, A. B.; Glaspell, G.; El-Shall, M. S. *J. Am. Soc. Chem.* **2006**, *128*, 2790.

(28) Hu, X. L.; Yu, J. C.; Gong, J. M.; Li, Q.; Li, G. S. *Adv. Mater.* **2007**, *19*, 2324.

(29) Yu, J. C.; Hu, X. L.; Li, Q.; Zhang, L. Z. *Chem. Commun.* **2005**, 2704.

(30) Hu, X. L.; Yu, J. C. *Chem.-Asian J.* **2006**, *1*, 605.

(31)Choi, K.H.; Chae, W.S.; Jung, J. S.; Kim Y. R. *Bull. Korean Chem. Soc.* **2009**, *30,* 1118.

(32)Guan, M. Y.; Sun, J. H.; Han, M.; Xu, Z.; Tao, F. F.; Yin, G.; Wei, X. W.; Zhu J. M.; Jiang, X. Q. *Nanotechnology* **2007**, *18*, 415602.

(33) Ma, Y. R.; Qi, L. M.; Ma, J. M.; Cheng, H. M. *Langmuir* **2003**, *19*, 4040.

(34) Ma, Y. R.; Qi, L. M. *J. Colloid interface Sci.* **2009**, *335*, 1.

Chapter Six

Microwave-Assisted Synthesis and Assembly of ZnO Spindles

6.1 Introduction

Zinc oxide (ZnO), an important II–VI semiconductor with a bandgap of 3.37 eV and a large exciton binding energy of 60 MeV, has attracted much attention due to its potential applications in solar cells,[1-3] gas sensors,[4] photovoltaic devices[5, 6] and photocatalysis.[7-11] In recent years, various ZnO morphologies including nanowires,[12, 13] nanorods,[14-16] nanoribbons,[17] nanoplates,[18] nanotubes,[19] multipods,[20] nanoclusters,[21] and even hollow microhemispheres and microspheres[22] were prepared. Moreover, a number of well-known techniques such as high-temperature chemical vapor transport, physical vapor deposition, hydrothermal routes, template-directed synthesis, self-assembly of nanocrystals were developed to fabricate ZnO Micro/nanostructures, but these methods usually involved either a relatively long period of processing time, substrate-dependence or complex multi-step processes. Microwave-induced chemical

synthesis is often very efficient since it offers rapid volumetric heating, high reaction rates, high yields of products and energy saving. It is also a rapid and economic method, which easily programs the experimental conditions and significantly shortens the synthesis time to minutes.[21, 23]

However, there is no paper concerning the preparation of an integrated series of ZnO morphologies, from simple microspindles to complex flowers, paddies and clusters by the microwave-assisted method. Herein, we report the synthesis of a series of ZnO microstructures by a one-step microwave-assisted method.

6.2 Experimental

All chemicals were of analytical grade and were used as received without further purification. All the samples were prepared in a microwave digestion system (Ethos TC Plus 1, Milestone). In a typical synthesis, various amounts of hexamine and phenol were dissolved in 44 mL of water. And then various concentrations of $Zn(NO_3)_2$ solution were added. After stirring mildly for 2-10 min, the solution was sealed in a high-pressure digestion vessel which was Teflon-lined and double-walled. The reaction vessel was fit with a temperature probe that was housed in a sturdy thermowell and protected from chemical attack by a triple layer of PTFE/ceramic/PTFE. The desired exposure time and temperature were programmed by using Milestone's EasyControl software. The Automatic Temperature Control

system allowed continuous monitoring and controlling (±1℃) of the internal temperature. The preset profile (desired time and temperature) was followed automatically by continuously adjusting the applied power (0-1000 W) in order to keep the reaction temperature at a certain temperature (such as 100°C, 150°C and 220°C). After treating the mixed solution for two to ten minutes, the vessel was cooled to room temperature. The product was collected, washed with deionized water and absolute ethanol, and dried in a vacuum at 60℃ for 6 hours. Finally, as-prepared powder was obtained for further characterization.

The samples were examined by powder XRD with a Bruker D8 Advance diffractometer using Cu Kα_1 irradiation (λ = 1.5406 Å). Diffraction patterns were collected from 25° to 95° with a step size of 0.02°. TEM images were recorded on a CM-120 microscope (Philips, 120 kV) coupled with an EDX spectrometer (Oxford Instrument). High-resolution transmission electron microscopy (HRTEM, Tecnai 20, 200kV) was also used. Samples were deposited on thin amorphous carbon films supported by copper grids from ultrasonically processed ethanol solutions of the samples. The general morphology of the products was characterized by field emission scanning electron microscopy (FESEM, Quanta 400 FEG).

6.3 Results and discussion

An X-ray diffraction (XRD) pattern of the as-synthesized products is shown in Fig.

6.1a. All diffraction peaks are in good agreement with the JCPDS card (No. 36-1451), which can be indexed to a typical wurtzite-type ZnO crystal. The narrow sharp peaks suggest that the ZnO products are highly crystalline. No other impurities such as $Zn(OH)_2$ are observed.

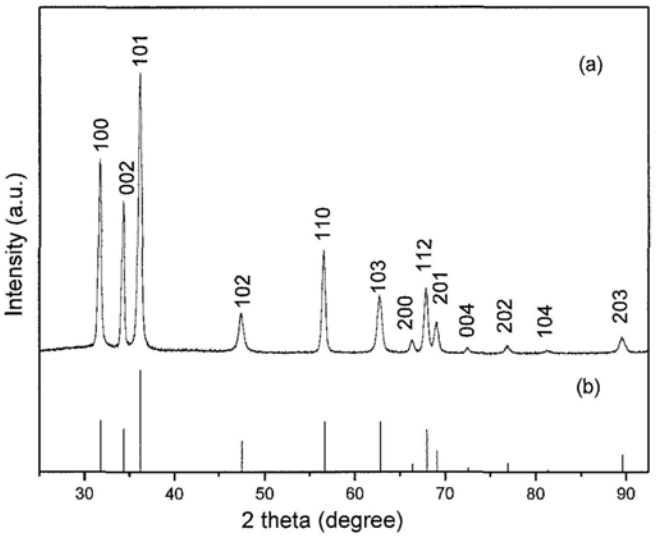

Figure 6.1 XRD patterns of as-prepared products (a) and standard ZnO (JCPDS no. 36-1451) (b).

The detailed conditions for preparing the samples are listed in Table 6.1. The size and shape of the products were examined by FESEM. Fig. 6.2a–d show representative FESEM images of the samples prepared at 150°C. It is observed that the shape of the samples depends on the amount of hexamine used, and evolves from spindles (S1 and S2, see Fig. 6.2a, b) to flowers (S3 and S4, see Fig. 6.2c, d). All of the products are composed of a large quantity of uniform spindles or flowers. These particles are characterized by a narrow size distribution (relative standard deviation ≤5%), obtained from a statistical analysis of over 100 particles. The aspect ratio (c/a) of a shape is defined as the length of the major axis (c) divided by the width of the minor axis (a). Sample 1 has the largest c and a. The amount of hexamine had a significant effect on the morphology of the as-prepared ZnO. When the amount of hexamine was increased from 0.05 to 0.1mmol (see Fig. 6.2a, b), the microspindles structures were still maintained. With the increase of the hexamine amount, the sizes of single spindle decreased from 1.19μm to 1.08μm in diameter and from 5.31μm to 4.56μm in length respectively. Both S1 and S2 consist of a large number of monodispersed microspindles, and very few multi-linked spindles such as T-shaped and X-shaped complex morphologies. However, when the amount of hexamine was increased to 0.15mmol, it is interesting that flowerlike ZnO microstructures (⩽50% of whole morphologies) were formed (S3, see Fig. 6.2c), still containing some X-shaped or starlike morphologies. By increasing the amount of hexamine to 0.2 mmol, ZnO microstructures (S4) were almost flowers. Fig. 6.3a displays a typical ZnO microflower with a diameter of about 2.61μm and the single petal diameter of about

430 nm. The morphology and microstructure of the ZnO flower were further investigated by TEM, HRTEM, SAED pattern and EDS. Fig. 6.3b depicts a typical bright field TEM image of S4, which shows a well-defined flower morphology. The insert selective area electron diffraction (SAED) pattern that corresponds to a single petal of the flower (see Fig. 6.3b) indicates the single-crystalline structure. The spacing of the fringes taken from the tip of the flower petal was determined to be 0.26 nm (shown in Fig. 6.3d), which is equal to the (0002) lattice spacing of bulk ZnO, hence indicating that the growth of these crystallites is in the [0001] direction. EDS was performed to further confirm the composition of the as-prepared products. Fig. 6.3d shows that the flower is composed of Zn and O with a ratio of ~1:1, giving a stoichiometric formula of ZnO. The Cu peak in the spectrum is attributed to the copper meshes of the TEM copper grid.

Table 6.1 Experimental conditions for the preparation of samples.

Sample No.	Hexamine	$Zn(NO_3)_2$	Phenol	Temp.	Time	Size(c/a)	Morphology
	[mmol]	[mmol]	[mmol]	[°C]	[min]	[μm/μm]	
S1	0.05	0.25	—	150	2	5.31/1.19	spindle
S2	0.10	0.25	—	150	2	4.56/ 1.08	spindle
S3	0.15	0.25	—	150	2	2.80/0.54	flower
S4	0.20	0.25	—	150	2	2.61/0.43	flower
S5	0.20	0.25	—	100	2	2.71/1.04	spindle,
S6	0.20	0.25	—	220	10	3.50/0.95	spindle
S7	0.10	0.25	—	220	10	0.78/0.23	paddy
S8	0.10	0.25	0.20	220	10	1.83/0.25	cluster

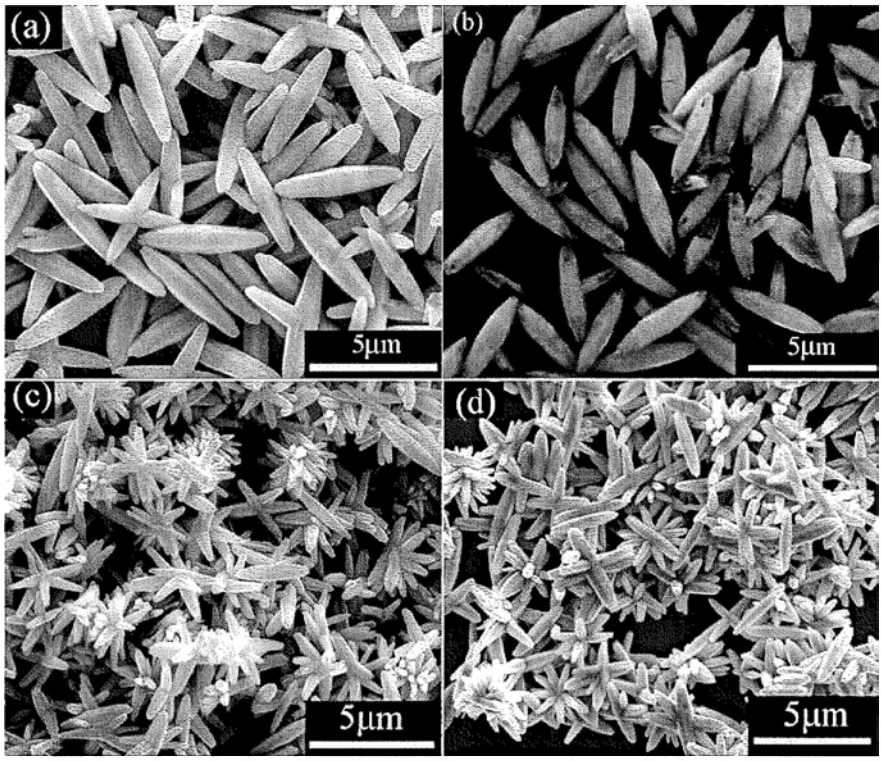

Figure 6.2 FESEM images of the products (S1-S4) prepared by the microwave irradiation 150 ℃ for 2min, with different hexamine/$Zn(NO_3)_2$ molar ratios (mmol/mmol). (a) 0.05:0.25, (b) 0.10:0.25, (c) 0.15:0.25, (d) 0.20:0.25.

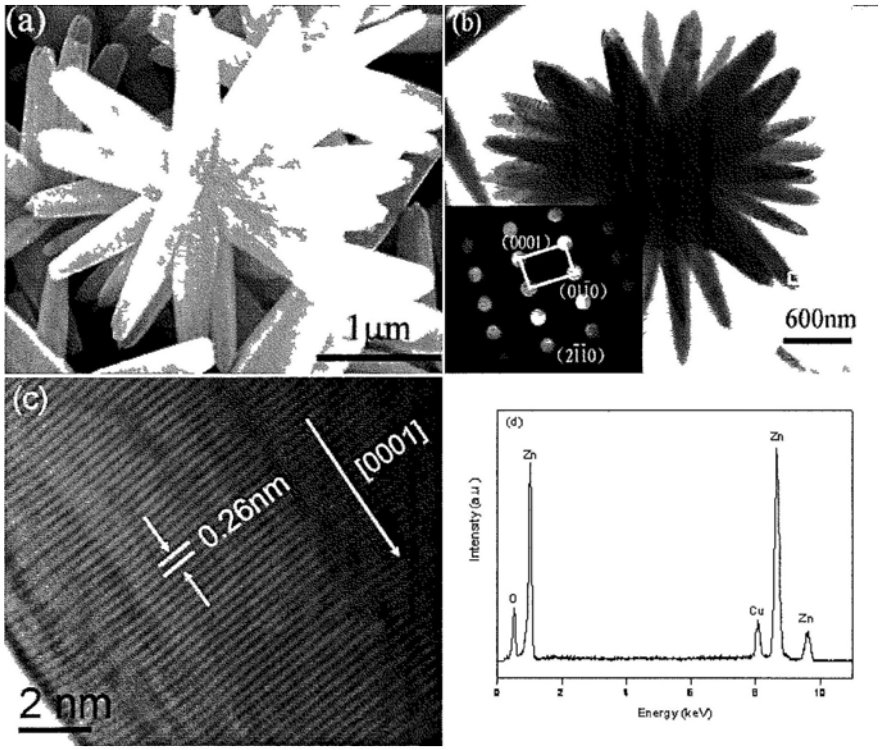

Figure 6.3 (a) Enlarged FESEM image and (b) TEM image of the as-prepared ZnO flower from the sample S4 shown in Figure 6 2d. The insert SEAD pattern corresponding to the small frame area marked in the tip of the flower, recorded along the [2$\bar{1}\bar{1}$0] zone. (c) HRTEM image taken from the tip of a ZnO flower petal. (d) EDX spectrum of sample S4.

Concerning the morphology evolution of the ZnO crystals, the hexamine must play a key role, because no other templates, surfactants, or emulsions are used in our reaction system. It is evident from Table 6.1 that varying the amount of hexamine provides systematic control of the morphology of the ZnO crystals, while a constant $Zn(NO_3)_2$ content is maintained at 0.25 mmol. Upon increasing the amount of hexamine from 0.05 to 0.20 mmol, the length of the resulting ZnO crystals decreases from 5.31 to 4.56 μm, whereas the radial diameter decreases from 1.19 to 1.08 μm. And in S3 and S4, almost all the deposited ZnO particles possess the flowerlike morphology, and very few ZnO rods were formed. So it can be concluded that hexamine will promote the growth of the flowerlike morphology and inhibit the formation of undesired nanorods, which is consistent to what was reported by others.[24] The major chemical reactions for the formation of ZnO in the aqueous solution can be summarized as Eqs. (1)–(3):

$$(CH_2)_6N_4 + 6H_2O \rightarrow 4NH_3 + 6HCHO \quad (1)$$

$$NH_3 + H_2O \rightarrow NH_4^+ + OH^- \quad (2)$$

$$Zn^{2+} + 2OH^- \rightarrow Zn(OH)_2 \rightarrow ZnO\,(s) + H_2O \quad (3)$$

During the heating process to 150 ℃, hexamine will decompose into NH_3 and HCHO, and OH^- ions formed as a result of the reaction of H_2O with NH_3, leading the ionic product of $Zn(OH)_2$. Subsequently, ZnO nuclei formed rapidly.

Moreover, it has been reported that infinite chains of $[Zn(hexamine)Cl_2]_n$ and $[Zn(hexamine)en]_n$ can be formed by bidentate coordination linking tetrahedral zinc ions.[24-26] So it is reasonable to believe that a similar complex structure may exist in

the current [zinc(hexamine)$(NO_3)_2]_n$ system as well. First, the structure can act as the nucleation center and facilitate the homogeneous precipitation of $Zn(OH)_2$ in the bulk solution. Second, it can serve as the organic template and modify the nucleation process and resultant structure of ZnO. It has been reported that, under the hydrothermal condition, hexamine can promote the formation of well-aligned and highly crystallized ZnO nanorods and nanowires when the ZnO seed layer was adopted.[24-28] In our microwave system, it can be expected that hexamine will promote the formation of nanorods constituting the petal crystal of the flower.

In addition, the influence of reaction temperature on the morphology of the products has been investigated. Fig. 6.4a and 4b illustrate FESEM micrographs of ZnO prepared at 100 ℃ for 2min, the molar ratio (mmol/mmol) of hexamine/$Zn(NO_3)_2$ is 0.20:0.25. The magnified SEM image (Fig. 6.4b) shows that a ZnO spindle is 2.71μm in length and 1.04μm in diameter, and the aspect ratio is a bit smaller than other samples (S1-S4) prepared under 150℃. Meanwhile, with the same amounts of reagents, when the reaction temperature is increased to 220℃ and maintained for 10mins, columnar spindles can be formed. The products are monodispersed spindles (S6, see Fig. 6.4c, d) which maybe fused together to form T-shaped, cross-shaped and star-shaped morphologies. When the molar ratio (mmol/mmol) of hexamine/$Zn(NO_3)_2$ is cut in half to 0.10:0.25 while maintaining the temperature at 220℃, the paddylike morphology can be produced. Each paddy is composed of many uniform spindles, 0.78μm in length and 0.23μm in diameter (S7, see Fig. 6. 4e, f).

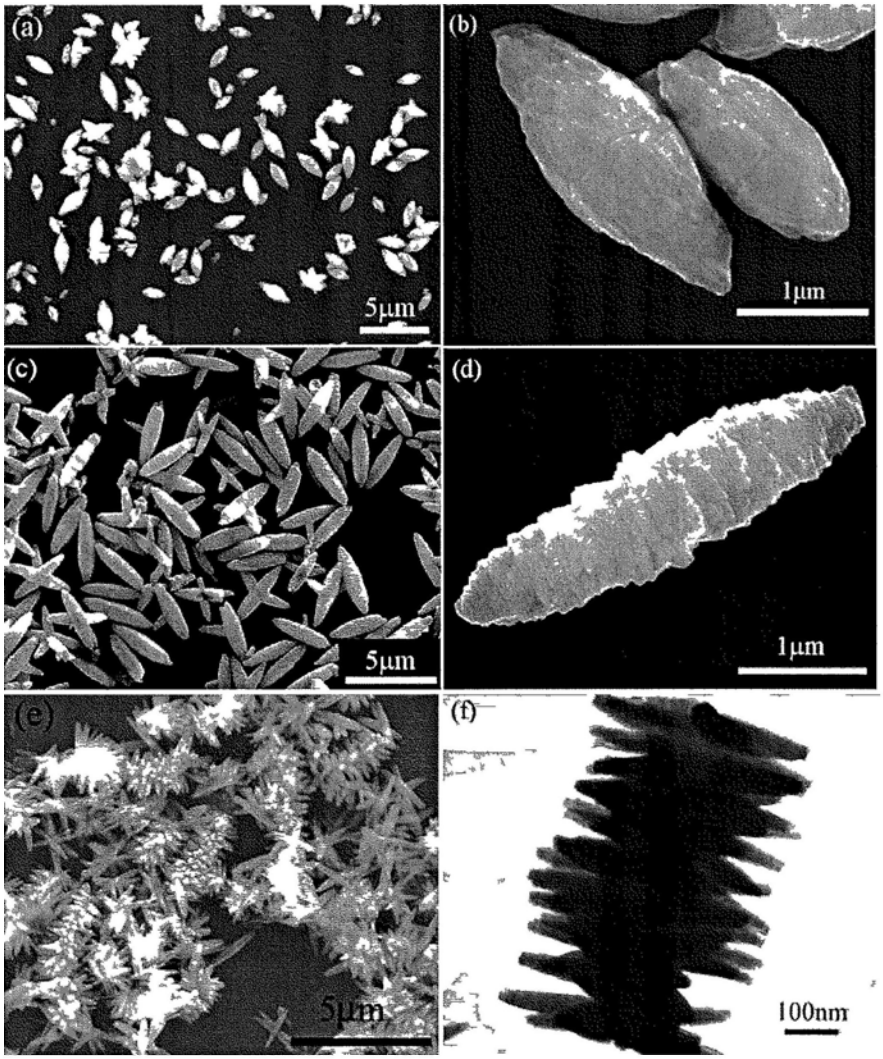

Figure 6.4 (a, b) FESEM images of sample S5 prepared by the microwave irradiation 100℃ for 2min. (c, d) FESEM images of sample S6 prepared by the microwave irradiation 220℃ for 10min, hexamine/$Zn(NO_3)_2$ = 0.20:0.25 (mmol/mmol). (e, f) FESEM image and TEM image of sample S7 prepared by the microwave irradiation 220℃ for 10min, hexamine/$Zn(NO_3)_2$ = 0.10:0.25 (mmol/mmol).

Phenol was added in the preparation of sample S8. FESEM and TEM images show ZnO clusters containing many uniform spindles (see Fig. 6.5), each spindle is about 1.83μm in length and 0.25μm in diameter. As shown in equation (1), hexamine would decompose into NH_3 and HCHO under high temperature, HCHO may react with phenol to form a phenol formaldehyde resin polymer. It has been reported that many polymers can influence the nucleation, growth and aggregation processes of ZnO.[16, 18] The polymers can change the growth rate along some crystallographic directions,[29–35] or even acts as a binder to form hierarchical structures such as mesocrystals by using preformed particles as building blocks.[29-33]

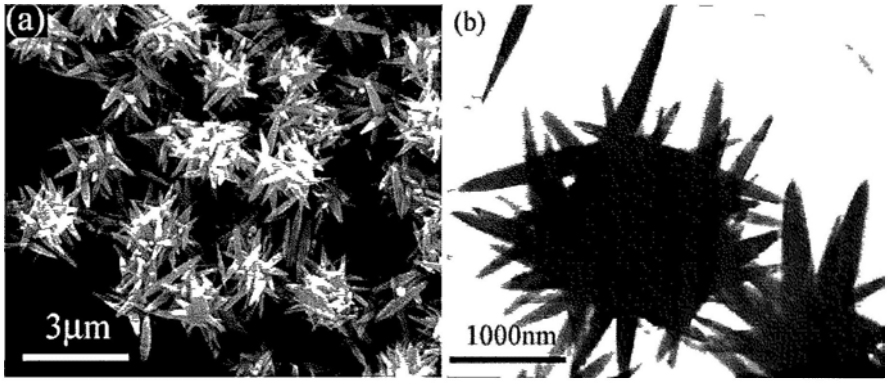

Figure 6.5 FESEM and TEM images of the products (S8) prepared by the microwave irradiation 220 ℃ for 10min, phenol/hexamine/$Zn(NO_3)_2$ = 0.2:0.05:0.25 (mmol/mmol/mmol).

On the basis of the experimental results, the formation mechanism of ZnO can be outlined as follows: under microwave irradiation, large quantities of small primary ZnO nuclei are generated by the rapid microwave-induced hydrolysis of Zn^{2+} (Scheme 6.1, step 1). The freshly formed ZnO nuclei are unstable because of their high surface energy and they tend to aggregate rapidly, probably driven by the oriented attachment process accompanied by Ostwald ripening (Scheme 6.1, step 2). Laudise and Ballman[36] suggested that the formation of the hexagonal shape and the capping faces at the top of wurtzite-type ZnO crystals were related to the relative growth rates in different crystal facets. They claimed that the (0001) face was not a stable face, thus the maximum growth rate in ZnO crystal was in the [0001] direction. Its rate was about twice as fast as that in the $[10\bar{1}0]$ direction, while the growth rate along $[10\bar{1}1]$ was in between the two. These ZnO molecules or clusters, whose principal faces are (0001), act as a site of seeds to accommodate newly formed ZnO molecules. So the primary crystals are in favor of recrystallizing in an ordered manner along the c-axis (Scheme 6.1, step 3), which produces the final spindlelike crystals (S1–2, 5 and 6). In the presence of phenol, clusters are formed. (S8, Scheme 6.1, step 4) If there are two or three active sites, they will trigger the nucleation at the interface, promoting the formation of T-shaped or X-shaped crystals extending from the interface. Meanwhile, if there are many active sites, the flowerlike or paddylike morphologies can be expected. (S3, 4, 7, Scheme 6.1, step 4')

Scheme 6.1 Schematic illustration for ZnO crystal growth.

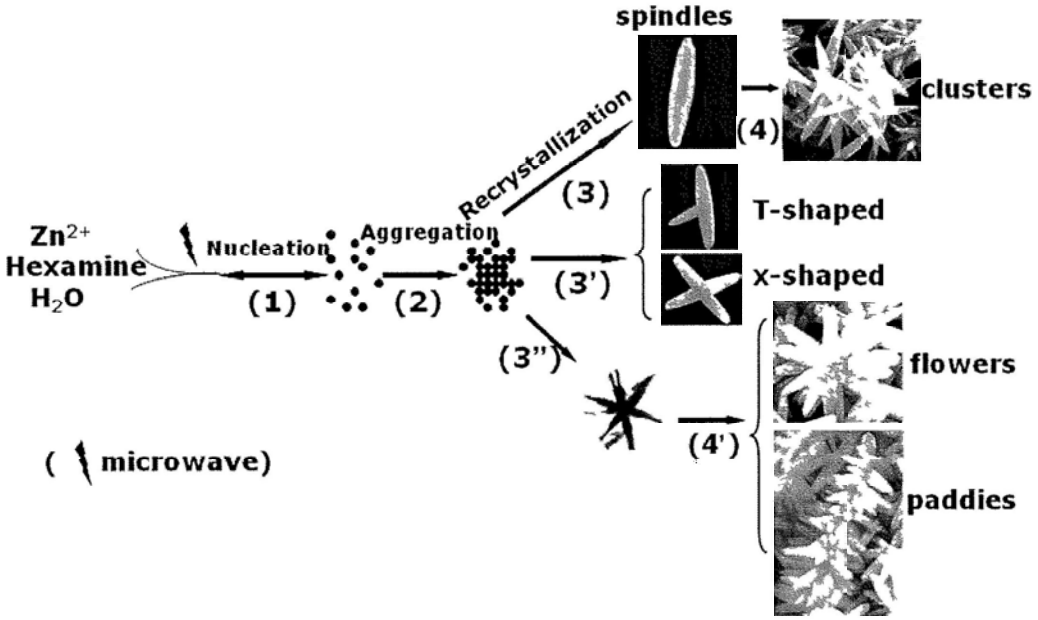

6.4 Conclusions

A series of ZnO structures (spindles, flowers, paddies, and clusters) were successfully synthesized by a programmed microwave-hydrothermal method. The effects of reaction conditions including reaction temperature and reactant concentration on the morphology of ZnO were investigated systematically. Results reveal that the initial molar ratio of hexamine to Zn^{2+} plays a crucial role in controlling the final size and shape of the ZnO products. These interesting ZnO structures may have potential applications in electronic and optoelectronic devices. This efficient microwave-hydrothermal method significantly reduces the synthesis time to minutes.

6.5 References

(1) Hara, K. *Sol. Energy Mater. Sol. Cells* **2000**, *64*, 115.

(2) Zhang, Q. F.; Chou, T. P.; Russo, B.; Jenekhe, S. A.; Cao, G. Z. *Angew. Chem. Int. Ed.* **2008**, *47*, 2402.

(3) Hamann, T. W.; Martinson, A. B. F.; Elam, J. W.; Pellin, M. J.; Hupp, J. T. *Adv. Mater.* **2008**, *20*, 1560.

(4) Lehman, H. W.; Widmer, R. *J. Appl. Phys.* **1973**, *44*, 3868.

(5) Keis, K.; Vayssieres, L.; Lindquist, S. E.; Hagfeldt, A. *Nanostruct. Mater.* **1999**, *12*, 487.

(6) Hsu, Y. F.; Xi, Y. Y.; Tam, K. H.; Djurisic, A. B.; Luo, J. M.; Ling, C. C.; Cheung, C. K.; Ng, A. M. C.; Chan, W. K.; Deng, X.; Beling, C. D.; Fung, S.; Cheah, K. W.; Fong, P. W. K.; Surya, C. C. *Adv. Funct. Mater.* **2008**, *18,* 1020.

(7) Yumoto, H.; Inoue, T.; Li, S. J.; Sako, T.; Nishiyama, K. *Thin Solid Films.* **1999**, *345*, 38.

(8) Lu, F.; Cai, W. P.; Zhang, Y. G. *Adv. Funct. Mater.* **2008**, *18*, 1047.

(9) Ivanov, V. K.; Shaporev, A. S.; Sharikov, F. Y.; Baranchikov, A. Y. *Superlattices Microstruct.* **2007**, *42*, 421.

(10) Moghaddam, F. M.; Saeidian, H.; Moghaddam, F. M.; Saeidian, H.; *Mater. Sci. Eng. B* **2007**, *139*, 265.

(11) Villasenor, J.; Reyes, P.; Pecchi, G. *J. Chem. Technol. Biotechnol.* **1998**, *72*, 105.

(12) Pan, Z. W.; Dai, S.; Rouleau, C. M.; Lowndes, D. H. *Angew. Chem. Int. Ed.* **2005**,

44, 274.

(13) Ku, C. H.; Yang, H. H.; Chen, G. R.; Wu, J. J. *Cryst. Growth Des.* **2008**, *8,* 283.

(14) Greene, L. E.; Law, M.; Goldberger, J.; Kim, F.; Johnson, J. C.; Zhang, Y.; Saykally, R. J.; Yang, P. *Angew. Chem. Int. Ed.* **2003**, *42*, 3031.

(15) Hsu, J. W. P.; Clift, W. M.; Brewer, L. N. *Langmuir* **2008**, *24*, 5375.

(16) Gao, Y. F.; Miao, H. Y.; Luo, H. J.; Nagai, M. *Cryst. Growth Des.* **2008**, *8*, 2187.

(17) Kong, X. Y.; Wang, Z. L. *Nano Lett.* **2003**, *3*, 1625.

(18) Tian, Z. R.; Voigt, J. A.; Liu, J.; Mckenzie, B.; Mcdermott, M. J.; Rodriguez, M. A.; Konishi, H.; Xu, H. *Nat. Mater.* **2003**, *2*, 821.

(19) Yu, H.; Zhang, Z.; Han, M.; Hao, X.; Zhu, F. *J. Am. Chem. Soc.* **2005**, *127,* 2378.

(20) Yan, H.; He, R.; Pham, J.; Yang, P. *Adv. Mater.* **2003**, *15,* 402.

(21) Hu, X. L.; Gong, J. M.; Zhang, L. Z.; Yu, J. C. *Adv. Mater.* **2008**, *20*, 4845.

(22) Mo, M. S.; Yu, J. C.; Zhang, L. Z.; Li, S. K. A. *Adv. Mater.* **2005,** *17*, 756.

(23) Yu, J. C.; Hu, X. L.; Li, Q.; Zhang L. Z. *Chem. Commun.* **2005**, *21*, 2704.

(24) Gao, X. D.; Li, X. M.; Yu, W. D. *J. Phys. Chem. B* **2005**, *109*, 1155.

(25) Pickardt, J.; Droas, P. *Acta Cryst.* **1989**, *C45*, 360.

(26) Zheng, S. L.; Tong, M. L.; Chen, X. M. *Coord. Chem. Rev.* **2003**, *246,* 185.

(27) Gorender, K.; Boyle, D. S.; O'Brien, P.; Binks, D.; West, D.; Coleman, D. *Adv. Mater.* **2002**, *14*, 1221.

(28) Choy, J. H.; Jang, E. S.; Won, J. H.; Chung, J. H.; Jong, D. J.; Kim, Y. W.; *Adv. Mater.* **2003**, *15*, 1911.

(29) Colfen, H.; Mann, S. *Angew. Chem. Int. Ed.* **2003**, *42*, 2350.

(30) Yu, S. H.; Colfen, H. *J. Mater. Chem.* **2004**, *14*, 2124.

(31) Xu, A. W.; Ma, Y.; Colfen, H.; Yu, S. H.; Colfen, H. *J. Mater. Chem.* **2007**, *17*, 415.

(32) Colfen, H.; Yu, S. H. *MRS Bull.* **2005**, *30*, 727.

(33) Colfen, H.; Antonietti, M. *Angew. Chem. Int. Ed.* **2005**, *44*, 5576.

(34) Mann, S. *Angew. Chem. Int. Ed.* **2000**, *112*, 3532.

(35) Tian, Z. R.; Voigt, J. A.; Liu, J.; McKenzie, B.; McDermott, M. J.; Rodriguez, M. A.; Konishi, H.; Xu, H. *Nat. Mater.* **2003**, *2*, 821.

(36) Laudise, R. A.; Ballman, A. A. *J. Phys. Chem.* **1960**, *64*, 688.

Chapter Seven

Conclusions

Various inorganic nanomaterials including magnetic materials and bifunctional core/shell nanostructured materials were fabricated. Several fast and energy efficient methods were developed for fabricating inorganic nanostructures or microstructures with controllable size distributions and morphologies. Some potential applications in biomedical field have also been discussed.

Magnetic $FeNi_3$ nanochains were synthesized by reducing iron(III) acetylacetonate and nickel(II) acetylacetonate with hydrazine in ethylene glycol solution without any template under a rapid and economical microwave irradiation. The diameter of the chains can be tuned by changing the concentration of the precursors, iron(III) acetylacetonate and nickel(II) acetylacetonate. The ratio of the precursors plays an important role in the formation of $FeNi_3$ nanostructures. Magnetic measurement reveals that the $FeNi_3$ nanochains show enhanced coercivity and saturation magnetization. The formation mechanism of the product is discussed. Toxicity tests by exposure of $FeNi_3$ nanochains to the zebrafish larvae show that the as-prepared nanochains are biocompatible. This new materials can be used as efficient and sensitive MRI probes. In addition, the present synthetic method and growth mechanism might be extended to other magnetic substances to direct large-scale

synthesis of similar nanochains.

Magnetic resonance imaging (MRI) contrast agents, mesoporous magnetite (Fe_3O_4) nanoclusters were demonstrated. The nanoclusters were synthesized by reducing iron(III) acetylacetonate with hydrazine in ethylene glycol under microwave irradiation. The diameter of the nanoclusters could be controlled effectively between 75 nm and 115 nm by increasing the amount of iron(III) acetylacetonate. Brunauer-Emmett-Teller (BET) results reveal a mesoporous structure and a large surface area of 72.3 m^2 g^{-1}. Toxicity tests by exposing zebrafish larvae to magnetite nanoclusters indicated that the as-prepared nanoclusters were non-toxic. The nanoclusters exhibited an enhanced T_2 relaxivity value of 406 s^{-1} mM^{-1}. *In vitro* and *in vivo* MRI confirmed the effectiveness of the magnetite nanoclusters as MRI probes. The biodistribution of the nanoclusters in rat liver and spleen after intravenous injection was also investigated.

Bifunctional mesoporous core/shell Ag@$FeNi_3$ nanospheres were synthesized by reducing iron(III) chloride, nickel(II) chloride and silver nitrate with hydrazine in ethylene glycol under microwave irradiation. This is a rapid and economical route based on an efficient microwave-hydrothermal process which significantly shortens the synthesis time to one minute. Toxicity of Ag@$FeNi_3$ nanospheres has been reduced compared to silver nanoparticles by exposuring to zebra fish. *In vitro* MRI confirmed the effectiveness of the Ag@$FeNi_3$ nanospheres as sensitive MRI probes. The interaction of Rhodamine B and nanospheres showed greatly enhanced fluorescence over the $FeNi_3$ nanoparticles.

Core/shell silver/phenol formaldehyde resin (PFR) nano/microstructures were synthesized through an efficient microwave process by self-assembly growth. Various morphologies, including monodispersed nanospheres, nanocables, and microcages were obtained by changing the fundamental experimental parameters, such as the reaction time and the kinds of surfactants (Pluronic P123 or CTAB). The results indicate that the presence of triblock copolymer Pluronic P123 would result in hollow silver/PFR microcages, while CTAB would prefer the formation of ultralong silver/PFR coaxial nanocables. In the absence of surfactants monodispersed core/shell silver/PFR nanospheres could be obtained, and the size of the nanospheres can be controlled in the range of 110 to 450 nm by changing the ratio of reagents (phenol: hexamine). The formation mechanism of the products is discussed based on the obtained results. The synthesized core/shell nano/microstructures with controllable morphologies may have potential applications in biotechnology and many other fields.

A series of ZnO structures (spindles, flowers, paddies, and clusters) were successfully synthesized by a programmed microwave-hydrothermal method. The effects of reaction conditions including reaction temperature and reactant concentration on the morphology of ZnO were investigated systematically. Results reveal that the initial molar ratio of hexamine to Zn^{2+} plays a crucial role in controlling the final size and shape of the ZnO products. These interesting ZnO structures may have potential applications in electronic and optoelectronic devices.

List of Publications

1. **Juncai Jia**, Jimmy C. Yu, Yi-Xiang J. Wang, King Ming Chan, Magnetic nanochains of $FeNi_3$ prepared by a template-Free microwave-hydrothermal method. *ACS Appl. Mater. Interfaces,* 2010, *2* (9), 2579-2584.
2. **Juncai Jia**, Feng Wang, Jimmy C. Yu, Toxicity study of metal and metal oxide nanoparticles by using zebrafish. *Environ. Chem.* 2011, *30*(1), 153-157.
3. **Juncai Jia**, Jimmy C. Yu, Yi-Xiang J. Wang, King Ming Chan, Magnetite nanoclusters as magnetic resonance probes. (Submitted)

Conference Presentations

1. **Juncai Jia**, Jimmy C. Yu, and Jiangtao Zhu, Microwave-assisted synthesis of monodispersed silver@phenol formaldehyde resin core/shell nanostructures, *the 2nd International Symposium of Energy and Environment*, Hong Kong, 8-10/12/2008.
2. **Juncai Jia**, Jiangtao Zhu, Jimmy C. Yu, Synthesis of hollow carbon nanospheres and carbon nanotubes through a silver@phenol formaldehyde resin core/shell template route, *the 3th International Symposium on Carbon for Catalysis*, Berlin, 8-12/11/2008.

3. Ka Lok Chiu, Fung Luen Kwong, **Juncai Jia**, Jia Li, Hang Leung Ng, Synthesis of porous biomorphic $Cu/CeO_2/Al_2O_3$ by using cotton as templates. Proceeding in the 2009 Fall Meeting of Materials Research Society (MRS), Boston, USA.